Laser-based terahertz-field-driven streak camera for the temporal characterization of ultrashort processes

Dissertation

zur Erlangung des Doktorgrades
des Fachbereichs Physik
der Universität Hamburg

vorgelegt von

Bernd Schütte
aus Telgte

Hamburg
2011

Gutachter der Dissertation	Prof. Dr. Markus Drescher Prof. Dr. Klaus Sengstock
Gutachter der Disputation	Prof. Dr. Markus Drescher Prof. Dr. Günter Huber
Datum der Disputation	12. September 2011
Vorsitzender des Prüfungsausschusses	Dr. Georg Steinbrück
Vorsitzender des Promotionsausschusses	Prof. Dr. Joachim Bartels
Leiterin des Fachbereichs Physik	Prof. Dr. Daniela Pfannkuche
Dekan der Fakultät für Mathematik, Informatik und Naturwissenschaften	Prof. Dr. Heinrich Graener

Abstract

In this work, a novel laser-based terahertz-field-driven streak camera is presented. It allows for a pulse length characterization of femtosecond (fs) extreme ultraviolet (XUV) pulses by a cross-correlation with terahertz (THz) pulses generated with a Ti:sapphire laser. The XUV pulses are emitted by a source of high-order harmonic generation (HHG) in which an intense near-infrared (NIR) fs laser pulse is focused into a gaseous medium. The design and characterization of a high-intensity THz source needed for the streak camera is also part of this thesis. The source is based on optical rectification of the same NIR laser pulse in a lithium niobate crystal. For this purpose, the pulse front of the NIR beam is tilted via a diffraction grating to achieve velocity matching between NIR and THz beams within the crystal. For the temporal characterization of the XUV pulses, both HHG and THz beams are focused onto a gas target. The harmonic radiation creates photoelectron wavepackets which are then accelerated by the THz field depending on its phase at the time of ionization. This principle is adopted from a conventional streak camera and now widely used in attosecond metrology. The streak camera presented here is an advancement of a terahertz-field-driven streak camera implemented at the Free Electron Laser in Hamburg (FLASH). The advantages of the laser-based streak camera lie in its compactness, cost efficiency and accessibility, while providing the same good quality of measurements as obtained at FLASH. In addition, its flexibility allows for a systematic investigation of streaked Auger spectra which is presented in this thesis. With its fs time resolution, the terahertz-field-driven streak camera thereby bridges the gap between attosecond and conventional streak cameras.

Zusammenfassung

In dieser Arbeit wird der Aufbau einer neuartigen Laser-basierten Terahertz-Feld-getriebenen Streak-Kamera vorgestellt. Sie ermöglicht die zeitliche Charakterisierung von Femtosekunden (fs) extrem-ultravioletten (XUV)-Pulsen durch eine Kreuzkorrelation mit Laser-basierten Terahertz-Pulsen. Die XUV-Pulse werden in einer Quelle von Höheren Harmonischen (HHG) erzeugt, die auf der Fokussierung eines intensiven nah-infraroten (NIR) Femtosekunden-Laserpulses in ein gasförmiges Medium beruht. Der Aufbau und die Charakterisierung einer Quelle für hoch-intensive Terahertz (THz)-Strahlung, die für die Streak-Kamera benötigt wird, ist ebenfalls Teil dieser Dissertation. Die Quelle beruht auf der optischen Gleichrichtung desselben nah-infraroten Laserpulses in einem Lithiumniobat-Kristall. Dabei wird die Pulsfront des Laserstrahls mit einem Brechungsgitter gekippt, um eine Geschwindigkeitsanpassung zwischen dem NIR- und dem THz-Strahl zu erreichen. Für die zeitliche Vermessung des XUV-Pulses werden sowohl HHG- als auch THz-Strahl in ein Gas fokussiert. Die harmonische Strahlung erzeugt Photoelektronen-Wellenpakete, die in der Folge durch das THz-Feld beschleunigt werden in Abhängigkeit von dessen Phase. Dieses Prinzip ist von der konventionellen Streak-Kamera übernommen und wird für die Vermessung von Attosekunden-Pulsen benutzt. Es handelt sich dabei um eine Weiterentwicklung einer Terahertz-Feld-getriebenen Streak-Kamera, die am Freien-Elektronen-Laser in Hamburg (FLASH) erstmals aufgebaut wurde. Die Vorteile der Laser-basierten Streak-Kamera liegen in ihrer Kompaktheit, der Kosteneffizienz und den verbesserten Zugangsmöglichkeiten, während die gleiche gute Qualität der Messungen wie am FLASH erhalten bleibt. Zudem ermöglicht ihre Flexibilität die systematische Untersuchung von gestreakten Auger-Spektren, die in dieser Arbeit gezeigt wird. Mit der Zeitauflösung der Terahertz-Feld-getriebenen Streak-Kamera im Femtosekunden-Bereich wird die Lücke zwischen konventionellen und Attosekunden-Streak-Kameras geschlossen.

Contents

Chapter 1

Introduction

After the invention of the laser in 1960 [1], a tremendous development in this field was triggered including the research on ultrashort pulsed lasers in the last decades. This opened up a new era of time-resolved spectroscopy in atoms and molecules, thereby investigating processes occurring on a microscopic dimension and an ultrashort time scale. The dynamic behavior in these systems is typically investigated in pump-probe experiments where one pulse creates an excited state in a system which is then probed by a second pulse with a variable time delay. Implementing this technique, a variety of processes can be studied including chemical reactions [2], molecular vibrations [3] and the ionization and tunneling delay time in an atom [4].

The energy concentration on a very short time scale also leads to high peak intensities. Thus, nonlinear optical effects occur which can be employed for various frequency conversion techniques. It is now possible to generate coherent radiation with extremely short and extremely long wavelengths covering the whole spectral region from X-ray [5] to terahertz (THz) [6] radiation. The discovery of high-order harmonic generation (HHG) in 1987 [7] has provided a source of ultrashort pulses with extreme-ultraviolet (XUV) wavelengths and pulse lengths extended down to the attosecond range in 2001 [8]. In addition to laser-based XUV radiation sources, free electron lasers (FELs) were built in recent years delivering XUV pulses with a much higher energy [9, 10]. The number of these facilities, however, is limited, since the costs are extremely high. Moreover, the emitted pulses exhibit high shot-to-shot fluctuations of the spectrum, the pulse energy and the temporal structure. Therefore, HHG is yet an outstanding source for the emission of ultrashort pulses in the XUV part and permits a time resolution in the attosecond range which is more than one order of magnitude better than what is achieved at FEL sources today.

For time-resolved experiments in the XUV range, the measurement of the pulse duration is an important task. It is a challenge, since techniques developed for the visible part of the spectrum are not easily transferred to the XUV part. Here, one cannot use crystals, because they are intransparent for

XUV radiation. For sources with a sufficient photon flux, techniques exploiting nonlinear effects of the XUV pulses in gases were developed [11, 12]. On the other hand, the method of laser-assisted photoionization with the generation of sidebands also works at low photon fluxes [13], but does not give access to XUV pulse durations much shorter than the fundamental laser pulse duration. This became first possible with the implementation of the light-field-driven streak camera which is used for the pulse duration measurement of attosecond radiation [14, 15]. It relies on the creation of photoelectron wavepackets which have the same temporal structure as the ionizing XUV beam. A superimposed light field accelerates the electrons according to its phase at the ionization time. In this way, the temporal structure is mapped into a distribution of electron energies. For the metrology of attosecond pulses, the frequency of the superimposed light field lies in the near-infrared (NIR) region of the spectrum. Transferring the principle to the femtosecond range, however, requires a light field in the THz region, because the oscillation period has to be much larger than the XUV pulse duration. A terahertz-field-driven streak camera was first developed by Ulrike Frühling at the Free Electron Laser in Hamburg (FLASH) and used for the temporal characterization of the XUV pulses [16]. While at FLASH a special THz undulator was utilized, it is desirable to make the terahertz-field-driven streak camera available to be used at other XUV and X-ray FELs as well as laser-based XUV and X-ray sources without the need of such a THz undulator. Another motivation is the development of a flexible device for electron wavepacket sampling in the femtosecond range. This technique is widely used in the attosecond range [4, 17] and principally allows for recording temporal information in a single sweep. For measuring electron dynamics occurring on a longer time scale such as certain Auger decays, an increased oscillation period of the streaking field is required.

For the development of the THz streaking technique on a laboratory scale, a high-intensity THz source is necessary. Remarkably, the same laser pulse which generates radiation at one extreme part of the spectrum via HHG, is also capable of generating radiation at a different extreme part of the spectrum referred to as THz radiation. For the generation of short THz pulses, various methods were investigated such as photoconductive switches [6] and the nonlinear interaction of the fundamental and its second harmonic in a plasma generated by the same laser pulse [18]. One of the most efficient sources today is optical rectification in a lithium niobate crystal while introducing a tilt to the pulse front of the driving laser [19, 20]. Utilizing this technique, THz pulse energies of up to $50\,\mu$J were achieved [21], thus being able to compete with accelerator-based sources of THz radiation [22].

In this work, the implementation of a compact, fully laser-based terahertz-field-driven XUV streak camera is presented for the first time. While exploiting the same principle as at FLASH, a major challenge here is to generate THz fields with sufficient electric field strengths in the laboratory. By developing a single-cycle THz source which is more efficient than comparable sources, the

HHG pulse duration and its linear chirp rate are determined with a temporal resolution of 10 fs. Here, one benefits from the inherent synchronization between both pulses and from the fact that the XUV pulse energy can be scaled down by averaging over a large number of pulses. The increased flexibility of the laser-based terahertz-field-driven streak camera now allows for a systematic investigation of electron wavepacket sampling in the femtosecond range. As a precedent experiment, the streaking of Auger electrons is studied which exhibits an unpredicted behavior.

The thesis is separated into four main parts. The theoretical concepts of the generation of high-order harmonics and THz radiation as well as the principles of the light-field-driven streak camera are discussed in Chapter 2. Chapter 3 gives an overview about the experimental setup including the femtosecond laser system and its conversion into extremely short (HHG) and extremely long wavelengths (THz), followed by a description of the streak camera. A characterization of the THz pulses is presented in Chapter 4 with general properties (Sec. 4.1) and measurements on the time-dependent electric field as well as the spectrum of the radiation utilizing electro-optic sampling (Sec. 4.2). These results are then compared with a scan of the electric field implemented by the streak camera technique (Sec. 4.3). In Chapter 5, it follows the temporal characterization of ultrashort processes with the focus on the determination of the HHG pulse duration and its linear chirp rate (Sec. 5.2) as well as on the investigation of streaked Auger spectra (Sec. 5.3). Finally, the results are summarized in Chapter 6.

Chapter 2

Theoretical background

In this Chapter, the theoretical background of this work is presented. Starting by a discussion of photoionization and the Auger process in Sec. 2.1, Sec. 2.2 and 2.3 deal with the generation of high-order harmonic and terahertz radiation, respectively. Sec. 2.4 then gives insight into the principles of the light-field-driven streak camera.

2.1 Photoemission processes

When photons interact with matter, this may lead to the emission of electrons depending on the light properties such as photon energy and intensity as well as the used medium. While for the nonlinear frequency conversion processes that will be covered in Sec. 2.2 and Sec. 2.3, multiphoton processes play a distinctive role, the consideration here is limited to the interaction of one photon with one atom. Concerning the generation of free electrons, one can distinguish between the direct photoionization and the emission of Auger electrons which will be discussed in the following.

2.1.1 Direct photoionization

The photoelectric effect describes the interaction of a photon with matter in which the photon energy is transferred to electrons in the matter. For a sufficient photon energy, E_{Ph}, an electron is released into the vacuum:

$$E_{Ph} = h\nu \geq I_P, \tag{2.1}$$

where h is the Planck constant, ν is the frequency of the light and I_P is the ionization potential of the electron. If the photon energy is larger than the ionization potential, the electron has a kinetic energy of $W_{kin} = h\nu - I_P$. Thus, by measuring the photon energy and the electron kinetic energy, one can determine the magnitude of the ionization potential. Numerical values for the different elements and different electronic states are in the range from a few eV to more than 1 MeV. Therefore, visible light cannot be used for ionization processes with one photon. Instead, XUV radiation is suitable for outer-shell and in some cases also inner-shell photoelectron spectroscopy. The probability of the photoionization process is expressed as the cross section which depends on the photon energy and the specific electron state of the element under consideration.

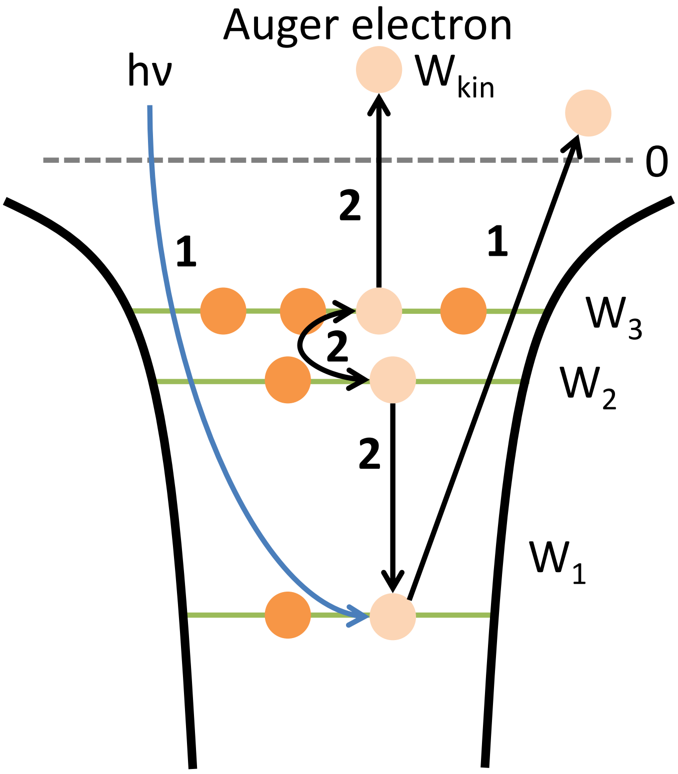

Figure 2.1: Schematic of the Auger process. In step 1, a photon transfers its energy to an inner-shell electron which is then excited or released into the vacuum. In the second step, the inner-shell hole is filled by an electron from an outer shell which transfers its energy to a third electron emitted as the Auger electron.

2.1.2 Auger electron emission

A different process that leads to the emission of an electron is the Auger effect. This is a secondary process, since it occurs after the photoionization or excitation of an inner-shell electron. According to Fig. 2.1, a photon with sufficient energy creates an inner-shell vacancy by exciting the corresponding electron or releasing it into the vacuum. The generated hole decays with a certain lifetime and is then filled by an electron from an outer shell. The energy difference $W_2 - W_1$ may now be emitted as a photon. Another possibility is the transfer of energy to a third electron which is freed into the vacuum and known as Auger electron. The kinetic energy of the Auger electron is independent from the photon energy and only determined by the involved orbitals: $W_{kin} = W_1 + W_2 - W_3$. The energy distribution of Auger electrons, however, is not sharp, but has a natural linewidth which is connected to the exponential decay behavior of the inner-shell vacancy. This is a significant difference compared to the case of photoionization. The time-dependent emission of Auger electrons was directly measured for the first time in [23].

2.2 High-order harmonic generation

High-order harmonic generation (HHG) is an extremely nonlinear optical process by which frequencies from the near-infrared (NIR) part of the electromagnetic spectrum are converted to radiation in the ultraviolet (UV), the extreme ultraviolet (XUV) or even the soft X-ray region of the spectrum. In fact, the highest generated photon energy is 3.5 keV [24] which corresponds to a frequency upconversion of a factor of more than 2000. The HHG process becomes possible when an intense laser pulse interacts with a gaseous medium. For typical peak intensities between 10^{13} to $10^{15}\,\mathrm{W/cm^2}$ the atomic potential barrier gets distorted, thus allowing electrons to tunnel through it. During the accelerated movement caused by the sinusoidal laser field, the electrons gain energy and may after a certain time recombine with the ionic cores, thereby emitting radiation with high photon energies. This radiation is strictly related to the initial laser field in the sense that the spectrum consists of odd multiples of the laser frequency which will be referred to as the fundamental frequency. A schematic of the HHG spectrum is shown in Fig. 2.2. It is characterized by an exponential decay of the intensity for lower harmonic orders referred to as the perturbative regime. This is followed by a region of about equal harmonic intensities, the so called plateau. It ends at the cut-off energy $E_{\text{cut-off}}$ where a fast intensity decrease is observed.

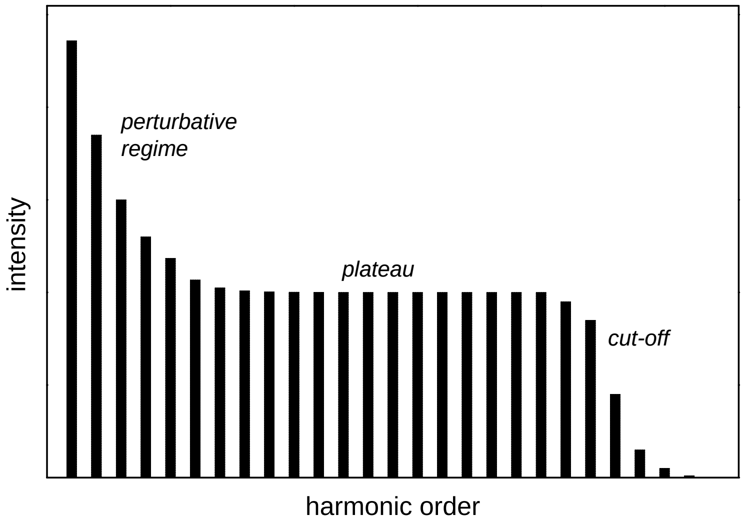

Figure 2.2: Schematic of a HHG spectrum

The conversion efficiency of the harmonic generation process depends on various parameters such as the kind of medium used, the harmonic order, the intensity of the driving laser and the geometry used for the generation. The highest efficiencies of 10^{-4} are obtained in two-color configurations of the driving laser at the 38^{th} harmonic [25, 26], while for cut-off harmonics beyond the 300^{th} order it drops to 10^{-11} [27].

The properties of HHG depend on microscopic as well as macroscopic effects. Most of the microscopic effects are covered by the semi-classical three-step-model [28] which will be discussed in the following. For a more accurate description of the response of a single atom, a quantum-mechanical model is needed [29]. On the other hand, phase-matching and absorption are important effects on the macroscopic level and will be covered in Sec. 2.2.2. Finally, the temporal characteristics of the HHG pulses will be considered.

2.2.1 The three-step model of HHG

The three-step-model provides a semiclassical view on the process of HHG and can explain major aspects of experimental results as well as give an intuitive understanding. It is restricted to the so called *tunneling regime*,

$$\hbar\omega_0 \ll I_p \ll U_p, \tag{2.2}$$

where ω_0 is the frequency of the fundamental laser, and U_p is the *ponderomotive potential* of the laser field which is given by

$$U_p = \left\langle \frac{1}{2} m_e v^2(t) \right\rangle = \frac{e^2 E_0^2}{4 m_e \omega_0^2} \propto \lambda_0^2 I_0. \tag{2.3}$$

Here m_e and v are the electron mass and velocity, e is the electron charge, E_0 is the electric field of the laser, I_0 its intensity and λ_0 its wavelength. The three steps are illustrated in Fig. 2.3 and described in the following.

1. Due to a strong laser field, the Coulomb potential of an atom is distorted. The resulting field is a superposition of the atomic potential without field and the induced laser field. A finite potential wall is created through which an electron can tunnel.

2. The electron is now regarded as a classical particle and moves freely in the laser field. It is accelerated until the laser field changes its sign. Afterwards it may be accelerated back to the vicinity of the ion, depending on its time of tunneling.

3. A recombination of the electron with its core ion leads to a simultaneous emission of radiation. The photon energy equals the ionization potential plus the kinetic energy the electron has acquired in the laser field.

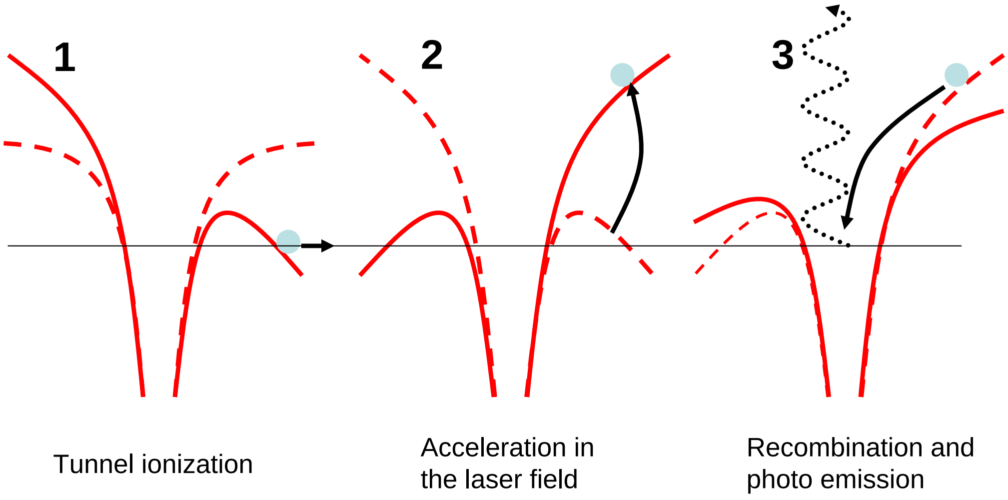

Figure 2.3: Illustration of the three-step model of HHG: (1) tunneling process due to a strong laser field, (2) acceleration in the laser field, and (3) recombination with the ion under emission of radiation.

The initial ionization rate can be calculated according to a formula derived by Ammosov, Delone and Kraïnov [30], which has been found to agree well with experimental results. The so called *ADK rate* is calculated by

$$w(t) = \omega_p \left|C_{n^*}\right|^2 \left(\frac{4\omega_p}{\omega_t}\right)^{2n^*-1} \exp\left(-\frac{4\omega_p}{3\omega_t}\right), \tag{2.4}$$

$$\left|C_{n^*}\right|^2 = \frac{2^{2n^*}}{n^*\Gamma(n^*+1)\Gamma(n^*)}, \tag{2.5}$$

$$\omega_p = \frac{I_p}{\hbar}, \qquad \omega_t = \frac{eE_0(t)}{\sqrt{2m_e I_p}}, \qquad n^* = Z\left(\frac{I_{ph}}{I_p}\right)^{1/2}. \tag{2.6}$$

$E_0(t)$ is the time-dependent amplitude of the electric field of the laser pulse, Z the net charge of the atom after the ionization process, I_{ph} the ionization potential of hydrogen, and $\Gamma(x)$ denotes the mathematical Gamma function. When the ADK rate is averaged over one cycle of the laser field, it can be written as [31]

$$w_{ave}(t) = \left(\frac{3\omega_p}{2\pi\omega_t}\right)^{1/2} w(t). \tag{2.7}$$

With the knowledge of the ionization rate, it is also possible to calculate the probability of an atom to have remained in its ground state:

$$R(t) = \exp\left[-\int_{-\infty}^{t} w(t')dt'\right]. \tag{2.8}$$

Considering only one-electron ionization, the density of free electrons inside the gas, $n_e(t)$, has to be equal to the density of ions and can thus be written as

$$n_e(t) = n_0(1 - R(t)), \tag{2.9}$$

where n_0 is the density of neutral atoms.

After the ionization process, the movement of the electron in the electric field is described classically. When neglecting the Coulomb attraction by the core, the electron motion is described by

$$\begin{aligned} a(t) &= \frac{eE_0}{m_e}\cos(\omega_0 t + \phi), \\ v(t) &= \frac{eE_0}{m_e\omega_0}(\sin(\omega_0 t + \phi) - \sin\phi), \\ x(t) &= \frac{eE_0}{m_e\omega_0^2}(\cos\phi - \cos(\omega_0 t + \phi)) - \sin\phi\frac{eE_0}{m_e\omega_0}t, \end{aligned} \tag{2.10}$$

with the initial conditions $x(0) = 0$ and $y(0) = 0$. For the electron being able to recombine with its parent ion, the NIR laser has to be linearly polarized. The ponderomotive potential is then given by the mean kinetic energy that the electron gains over one period (cf. Eq. 2.3). The actual energy of one electron, however, depends on the time of ionization. The maximum energy of 3.17 U_p is achieved for electrons which tunnel after 0.31 optical cycles of the electric field [28]. This leads to a condition for the maximum photon energy achievable in HHG which is given by

$$E_{\text{cut-off}} = \hbar\omega_{\text{cut-off}} = I_p + 3.17U_p. \tag{2.11}$$

According to this relation, in order to generate harmonic radiation with high frequencies, several parameters are important. First, an element with a high ionization potential I_p is advantageous. Secondly, the laser electric field must be high to achieve a large energy transfer to the electrons. And thirdly, a small laser frequency may be used.

Apart from the highest harmonic orders, certain photon energies can be achieved by electrons which tunnel at two different times. Electrons that tunnel at a time τ_l before the time of maximum return energy τ_c, are regarded to have a long trajectory, while electrons with return times $\tau_s > \tau_c$ have a short trajectory. In experiments, different properties for both contributions of a single harmonic order were observed [32].

According to the three-step-model, the process of HHG is periodic in time, as it occurs twice per laser cycle. It follows from Fourier analysis that in such a case the spectrum consists of peaks at odd multiples of the fundamental laser frequency.

Besides the three-step-model, several other theories of HHG were developed. Among them, a quantum mechanical model based on the strong field approximation was introduced by Lewenstein *et al.* [29]. Another approach was made by Becker *et al.* who solved the time-dependent Schrödinger equation for a zero-range potential [33].

2.2.2 Propagation and phase-matching effects

So far the response of a single atom irradiated by an intense laser pulse was considered. However, it turns out in the experiment that the characteristics of HHG radiation cannot be explained by these microscopic effects alone. In addition, macroscopic effects such as phase-matching have to be taken into account. Therefore, the Maxwell equations for the fundamental and harmonic fields must be solved. A simplified version of these propagation equations was discussed in [34], assuming a slowly varying envelope of the intensity as well as radial symmetry. The wave equation describing the propagation of a linearly polarized electromagnetic field in an isotropic, globally neutral, non-magnetic, dielectric medium can be written as [34]

$$\begin{aligned} \Delta_\perp E_0(\boldsymbol{r},t) + 2ik_0(\boldsymbol{r},t)\frac{\partial E_0(\boldsymbol{r},t)}{\partial z} &= 0, \\ \Delta_\perp E_q(\boldsymbol{r},t) + 2ik_q(\boldsymbol{r},t)\frac{\partial E_0(\boldsymbol{r},t)}{\partial z} &= -\frac{q^2\omega_0^2}{\epsilon_0 c^2}P_q^{NL}(\boldsymbol{r},t)\exp[i(qk_0-k_q)z]. \end{aligned} \tag{2.12}$$

E_0 and $\boldsymbol{k_0}$ are the amplitude and wavevector of the laser field, while E_q and $\boldsymbol{k_q}$ denote the corresponding quantities of the q^{th} harmonic order. The depletion of the fundamental field can be neglected due to the low conversion efficiency of HHG. For high intensities, the polarization in a medium corresponds nonlinearly to the electric field which gives rise to a nonlinear term of the polarization $P_q^{NL}(\boldsymbol{r},t)$. This serves as a source term for the harmonic field. It is given by [34]

$$P_q^{NL}(\boldsymbol{r},t) = n_a(z,t)d_q(\boldsymbol{r},t), \tag{2.13}$$

where $n_a(z,t)$ is the atomic density and $d_q(\boldsymbol{r},t)$ is the total harmonic dipole moment of the corresponding harmonic order which includes the contributions of all active electrons. Since the atomic densities used for the HHG process are usually low, a constant group velocity is assumed for both the fundamental and the harmonic pulses.

One important propagation effect is *reabsorption* of the harmonic radiation in the gaseous medium. The photons at higher orders typically have energies which allow them to directly ionize an atom. When only a small fraction of atoms is ionized, the imaginary part of the wavevector reads [34]

$$\mathrm{Im}(k_q) = \frac{r_0 \lambda_0 f_2 n_a}{q} = \frac{n_a \sigma_q}{2}, \tag{2.14}$$

where r_0 is the classical electron radius, λ_0 the wavelength of the fundamental radiation, f_2 the imaginary part of the atomic scattering factor and σ_q the photoionization cross section. The absorption length $L_{abs} = 1/n_a\sigma_q$ determines the distance after which the field is attenuated by a factor of exp(0.5).

Phase-matching plays a crucial role in the HHG process. For an efficient conversion to higher frequencies, the phase velocities of the fundamental and the harmonic beam must be the same. If this is not the case, the electric fields of harmonic radiation generated at different longitudinal positions will be different. Hence, destructive interference will occur if the medium exceeds a certain length. A general phase-matching condition can be deduced from Eq. 2.12 [35]:

$$k_q = qk_0 + \nabla\Phi_q. \tag{2.15}$$

Φ_q is the intrinsic phase of the harmonic dipole moment d_q. Various effects that can contribute to a phase mismatch are discussed in the following.

During the acceleration in the laser field, the electron acquires a *dipole phase*, Φ_q, which depends on the time τ between ionization and recombination. For the plateau region, it can be approximated by $\Phi_q \approx -U_p\tau \approx -\theta I_0$, where I_0 is the laser intensity. The slope θ depends on the return time and weakly varies for different intensities and atomic orders. As a consequence, different amounts of the dipole phase are acquired across the transverse beam profile of the fundamental beam for which the intensity decreases from the center to the edges. In addition, dipole phases for the long and short trajectories are different. Hence, when phase-matching is achieved for one of the trajectories, it may not be achieved for the other one.

A purely geometric dispersion effect is introduced by the *Gouy phase* due to the focusing of the fundamental laser. On the optical axis it is given by $\Phi_{geo} = \arctan(z/z_R)$ (cf. Appendix A), where z is the longitudinal coordinate and z_R is the Rayleigh length. The geometric dispersion is approximated by

$$\Delta\boldsymbol{k}_{geo} = q\delta\boldsymbol{k}_{0,geo} - \delta\boldsymbol{k}_{q,geo} \approx -\frac{q}{z_R}\boldsymbol{z}, \tag{2.16}$$

where $\delta\boldsymbol{k}_{0,geo}$ and $\delta\boldsymbol{k}_{q,geo}$ denote the corrections to the fundamental and harmonic wavevector, respectively, while $\boldsymbol{z}$ is the unity vector in longitudinal direction. For a fixed length of the gaseous medium, the geometric dispersion can be decreased by using focusing optics with a larger focal length, thereby increasing the value of the Rayleigh length.

The *atomic dispersion* is caused by the linear polarizability of the atoms. The resulting phase-mismatch can be written as [34]

$$\Delta \boldsymbol{k}_{atom} = q\delta \boldsymbol{k}_{0,atom} - \delta \boldsymbol{k}_{q,atom} \approx n_a \left(\pi \alpha_1 \frac{q}{\lambda_0} + r_0 f_1 \frac{\lambda_0}{q} \right) \boldsymbol{z}, \tag{2.17}$$

where α_1 refers to the static polarizability and f_1 is the real part of the atomic scattering factor. The influence of the atomic dispersion, however, is small for low gas densities.

Finally, the *electronic dispersion* mainly affects the fundamental beam. It becomes significant when a larger fraction of the atoms gets ionized and contributes to a phase-mismatch as follows [35]:

$$\Delta \boldsymbol{k}_{elec} = q\delta \boldsymbol{k}_{0,elec} - \delta \boldsymbol{k}_{q,elec} = r_0 \lambda_1 n_e (-q + \frac{1}{q}) \boldsymbol{z} \approx -r_0 q \lambda_0 n_e \boldsymbol{z}, \tag{2.18}$$

where n_e is the free-electron density.

A detailed phase-matching condition thus reads

$$\boldsymbol{k}_q = q\boldsymbol{k}_0 - \theta \nabla I_0 + \Delta \boldsymbol{k}_{geo} + \Delta \boldsymbol{k}_{atom} + \boldsymbol{k}_{elec}. \tag{2.19}$$

Efficient phase-matching is achieved when different components compensate for each other. In the HHG process, a number of parameters can be varied such as the gas density and volume, the laser intensity and the focusing characteristics as well as the relative position of the gas target with respect to the focal plane. These parameters are adjusted experimentally in order to optimize phase-matching and maximize the output energy of a certain harmonic order.

2.2.3 Temporal properties

As mentioned above, the harmonic spectrum consisting of peaks at odd multiples of the fundamental frequency implies a periodic process of HHG in the temporal domain where light bursts are emitted once per half laser cycle. Depending on the relative phases of the single harmonics, a train of attosecond pulses is emitted [36]. In this work, however, only one harmonic order is selected for the experiments which has a spectral bandwidth of less than 1 eV. In this case, a structure of the fs HHG pulses on an attosecond time scale is not observed. Instead, the pulse shape and duration are determined by different processes which are discussed in the following.

In the previous considerations concerning phase-matching effects it was pointed out that the dipole phase depends on the intensity of the laser. Hence, the dipole phase varies during the interaction time of the fundamental laser beam with the gaseous medium due to the time-varying envelope of the intensity. In order to determine the temporal profile of HHG pulses, the time-dependent generation efficiency has to be taken into account. This was done by solving the single-atom response and the propagation equations in [37] and [38] for different parameters of the HHG process. Strictly speaking, the obtained results are only valid for the specific parameters used in the calculations, because phase-matching conditions depend on a number of factors including the harmonic order. Still, several processes determining the temporal profile of harmonic generation can be understood from the calculations.

For pump intensities which are low enough to prevent a depletion of neutral atoms due to the HHG process, the pulse lengths of the harmonic radiation is found to be shorter compared to the fundamental laser beam by a factor of about 2. When the pump intensity gets higher, different effects may occur. For the 13^{th} harmonic investigated in [37], the harmonic pulse starts at an earlier time with respect to the temporal profile of the fundamental laser and has an asymmetric shape. The first result can be explained by the fact that the intensity is high enough already at the leading edge of the fundamental pulse in order to generate harmonic radiation efficiently. The asymmetric pulse shape is due to a strong degree of ionization which leads to a depletion of neutral atoms as well as photoelectron dispersion and thus hinders the HHG process [39]. On the other hand, for the 45^{th} harmonic investigated in [38], the pump intensity was varied by regarding different distances between the laser focus and the gaseous medium. When the distance is 0 and thus the pump intensity is increased to the maximum value, the temporal profile of the harmonic broadens and consists of a local minimum at the time of the highest pump intensity, while having 2 maxima at the leading and the trailing edge of the fundamental pulse. This is explained by a more efficient phase-matching for lower intensities. In addition, temporal profiles displaying structures are predicted [37, 38] which are partly explained by resonance effects in the single-atom response.

When comparing the results of pulse duration measurements at different harmonic orders, it has to be taken into account that the nonlinear response of the dipole moment to the laser field varies for the different harmonics. In general, one can say that the order of nonlinearity for the 59^{th} harmonic is smaller than for harmonics in the range from 9 to 27 (cf. [40]) which will be discussed in the following.

Pulse measurement methods

The pulse duration measurement in the XUV spectral range is challenging, since techniques developed for the visible part of the spectrum cannot easily be transferred to the XUV part. This is because it is not possible to use crystals in the latter case where the radiation is absorbed within a very short distance. For the measurement of HHG pulse durations, various alternative methods were developed which are divided into auto- and cross-correlation techniques. In the first case, two replicas of the same pulse are generated and superimposed in a medium. Instead, for a cross-correlation measurement, the XUV pulse is superimposed with a different light pulse. The occurrence of a nonlinear effect in the presence of both beams can be utilized to measure the pulse duration. Hereby, the temporal delay between the pulses is varied, and the change of the nonlinear effect is detected. In the following, different measurement techniques for the temporal characterization of fs XUV pulses are described.

Schins *et al.* performed a cross-correlation measurement where the 21^{st} harmonic is used to ionize helium [41]. The emitted photoelectrons have an energy which is determined by the photon energy minus the binding energy in helium. When in addition to the XUV pulse the fundamental laser field is applied, new lines in the spectrum appear which are shifted by multiples of the fundamental photon energy. These lines are referred to as sidebands of the n^{th} order. By varying the time delay between both beams, the harmonic beam was found to have a shorter length (38 fs) in comparison to the fundamental beam (150 fs). In addition, this technique also allows for measuring the chirp of the XUV pulse which was demonstrated by Mauritsson *et al.* [42]. Here, the change of the instantaneous frequency for a chirped pulse is exploited. This leads to a tilt of the sidebands with respect to the time delay axis between the two pulses.

Another method relies on cross-correlation frequency-resolved optical gating (XFROG) which was exploited in the XUV range by Sekikawa *et al.* [11]. With this technique it is possible to retrieve the intensity and the phase of the pulse. In addition to measuring a nonlinear optical effect in dependence on the time delay between two pulses, this signal is also spectrally dispersed and allows for a complete reconstruction of the XUV pulse. The technique was demonstrated by utilizing laser-assisted two-photon ionization as a nonlinear process, where an NIR beam was used as a reference. The pulse lengths for the fundamental and 9^{th} harmonic beams were 44 fs and 10 fs, respectively.

An autocorrelation technique for the measurement of HHG pulse lengths was developed by Nabekawa *et al.* [12]. It produces two replicas of the harmonic beam which can be delayed against each other. The technique is based on the two-photon double ionization of helium induced by the XUV beams. The ionization is enhanced when both beams overlap spatially and temporally which allows for measuring an autocorrelation trace. Again, the harmonic beam (27^{th} order) had a much shorter pulse duration (8 fs) compared to the fundamental pulse (23 fs).

The spectral interferometry for direct electric-field reconstruction (SPIDER) for XUV pulses was first proposed by Mauritsson *et al.* [43] and experimentally demonstrated by Mairesse *et al.* [13]. Two fundamental pulses with a variable time delay are generated to produce two HHG pulses. The energy of one fundamental pulse is shifted in order to introduce a shift to the HHG spectrum. In this way, a spectral shear is introduced. The XUV pulses are analyzed via an XUV spectrometer from which the electric field is reconstructed. The measured pulse lengths for the 11^{th} harmonic and the fundamental beams were 22 fs and 50 fs, respectively.

All these measurements were performed at low harmonic orders. For the techniques exploiting nonlinear effects this is necessary, because photon fluxes decrease rapidly for increasing harmonic orders. In contrast, the terahertz-field-driven streak camera still works for harmonics beyond the 50^{th} order, as it relies on ponderomotive streaking of single electrons. In fact, the measuring principle can also be utilized for characterizing pulses in the X-ray part of the spectrum. In comparison to the generation of sidebands it has the advantage that the time resolution is not limited by the pulse duration of the fundamental laser. Furthermore, the THz-field-driven streak camera has a single-shot capability which is important for a possible application at free electron lasers. While the SPIDER technique also works in a single-shot mode, it is limited to a low intensity range of the fundamental laser during the HHG process to ensure that both HHG pulses have the same properties. Moreover, the THz-field-driven streak camera may not only be implemented for XUV pulse characterization, but also for the investigation of electron wavepacket dynamics (cf. Sec. 5.3).

2.3 Generation and detection of single-cycle terahertz radiation

For the laser-based terahertz-field-driven streak camera a high intensity THz source with a field strength in the order of 10^7 V/m is needed and was developed during this work. The term THz refers to a frequency range from about 0.1 to 10 THz of the electromagnetic spectrum which corresponds to its far-infrared region. This range can more specifically be motivated by the used detection techniques which are in the THz range to a large extent based on thermal detectors.

This section starts with a comparison of different THz generation techniques. It follows a discussion of optical rectification and considerations concerning the tilted-pulse-front technique. The detection of the THz radiation is covered by a treatment of electro-optic sampling for the temporal characterization of the THz field.

2.3.1 THz generation techniques

In recent years, a variety of intense ultrashort THz sources has been developed which are all driven by mode-locked Ti:sapphire lasers and will shortly be presented in the following.

Photoconductive antennas [6, 44] consist of an undoped semiconductor where an electric field is applied. The absorption of laser radiation leads to the generation of electron-hole pairs and a reduced electrical resistance. If an ultrashort light pulse is applied, a rapid current change occurs which is accompanied by the emission of electromagnetic radiation in the THz range. The highest reported pulse energy for a photoconductive antenna is $0.8\,\mu$J [45]. In order to circumvent the high electric fields of up to 45 kV applied to the photoconductive antenna, built-in fields can be used. With the development of photoconductive metal-semiconductor-metal (MSM) structures, high accelerating fields were achieved by applying a bias of 50 V only [46].

The method of *four-wave mixing in a plasma* relies on the nonlinear interaction of the fundamental laser in combination with its second harmonic in a plasma [18]. The plasma can be produced in air or better in dry nitrogen. For this method electric field strengths of 40 MV/m were reported [47]. The pulse energy, however, was only 30 nJ and the high field strengths could only be achieved due to tight focusing (f=50 mm). In addition, the reported results could not be reproduced so far [48].

Optical rectification is based on difference frequency mixing in a nonlinear crystal which leads to the emission of THz radiation. In sources with a collinear geometry, zinc telluride (ZnTe) is often used as a nonlinear crystal [49], whereas the highest pulse energies of up to 50 μJ were achieved with a tilted-pulse-front technique using lithium niobate ($LiNbO_3$) as the nonlinear medium [21].

When choosing the most suitable source of THz radiation for the streak camera, various aspects have to be taken into account. As will be shown later, the focusing must not be too tight in order to minimize the influence of the Gouy phase shift. Therefore, the achievable field strengths from a plasma source are much lower than what was reported. In addition, the frequency of the generated THz radiation plays a role. Due to the influence of the ponderomotive potential, the streaking effect is more enhanced for lower frequencies. On the other hand, focusing pulses with lower frequencies typically leads to a larger focus size, thereby reducing intensities.

In this work, the method of optical rectification in a crystal of lithium niobate ($LiNbO_3$) was chosen for a variety of reasons. First, the scalability of this technique allows for high pulse energies by increasing the energy of the pump pulse. Secondly, albeit the peak frequency of 0.35 THz reported in [50] is rather low, it has been shown that the frequency in principle can be tuned upwards to more than 4 THz by cooling the crystal and preventing absorption of the higher frequency components [51]. For pump pulse energies which are comparable to those of the laser system used in the current work, a spectral moment of 1.2 THz [52] was reported. Finally, the method of optical rectification is comparably easy to realize.

2.3.2 Optical rectification

The process of optical rectification was first observed in 1962 [53]. For crystals with a low inversion symmetry, which is accompanied with a preferred internal direction, the polarization induced by an applied laser field does not necessarily change when the field changes its sign. In this way, an average direct current (dc) polarization is generated. When this effect is induced by an ultrashort laser pulse having a large bandwidth, this results in a beating polarization. Hereby, difference frequency mixing between the frequency components within the laser spectrum takes place which leads to the emission of electromagnetic radiation in the THz part of the spectrum. The following considerations are based on [54, 55, 56].

For high intensities, the polarization in a material contains a nonlinear term $\boldsymbol{P}^{NL}$ which can be expanded into a power series of the electric field $\boldsymbol{E}$ [54]:

$$\boldsymbol{P}^{NL} = \epsilon_0[\chi^{(2)}\boldsymbol{E}\boldsymbol{E} + \chi^{(3)}\boldsymbol{E}\boldsymbol{E}\boldsymbol{E} + \chi^{(4)}\boldsymbol{E}\boldsymbol{E}\boldsymbol{E}\boldsymbol{E} + \ldots], \tag{2.20}$$

where ϵ_0 is the vacuum permittivity. $\chi^{(n)}$ are nonlinear susceptibility tensors of the rank $n+1$. Optical rectification or difference frequency mixing is described by the second-order term $\chi^{(2)}$ which is given by [54]

$$\boldsymbol{P}_i^{(2)}(\Omega) = \sum_{j,k} \epsilon_0 \chi_{ijk}^{(2)}(\Omega = \omega_1 - \omega_2; \omega_1 - \omega_2) \boldsymbol{E}_j(\omega_1) \boldsymbol{E}_k^*(\omega_2). \tag{2.21}$$

The indices i, j, and k are the Cartesian components of the fields. The nonlinear susceptibility $\chi^{(2)}$ is a third-rank tensor, and symmetry determines which of the 27 tensor components are zero and which components are equal. In a centrosymmetric medium, $\chi^{(2)}$ is identically zero and no difference frequency generation will occur. In certain crystalline dielectrics, however, it is nonzero making them possible candidates as THz generation media.

Various aspects are important when choosing a suitable crystal. A single crystal has to be used which has a high transparency at pump and THz frequencies. As for a nonlinear process high pump intensities are needed, a high damage threshold is crucial. In addition, the crystal must have a high nonlinear optical coefficient for optical rectification, and competing nonlinear processes should be much weaker than difference frequency generation. Optical rectification has been demonstrated in many crystals, including the zinc blende crystals ZnTe and gallium phosphide (GaP) as well as $\mathrm{LiNbO_3}$. The latter is ferroelectric which is caused by a spontaneous polarization where the Li and Nb ions are displaced with respect to their symmetrical positions along the c axis (optical axis) of the crystal. The main process of optical rectification in $\mathrm{LiNbO_3}$ is impulsive stimulated Raman scattering [57]. Hereby, the fs laser pulse induces lattice vibrations which on their part lead to the generation of THz phonon-polariton waves [56].

The largest tensor component of $\mathrm{LiNbO_3}$ is $\chi_{333}^{(2)}(\Omega)$ which couples the polarizations of the fundamental and THz fields. The corresponding nonlinear coefficient is $d_{33} = \frac{1}{2}\chi_{333}^{(2)}(\Omega)$ and can be expressed as [58]

$$d_{33}(\Omega) = \frac{1}{2}\delta_{eee}\chi_e^2(\Omega)\chi_e^*(\Omega) + \frac{1}{2}\delta_{iee}\chi_i(\Omega)\chi_e(\Omega)\chi_e^*(\Omega), \tag{2.22}$$

where χ_e and χ_i are the electronic and ionic susceptibilities. The coefficients δ_{eee} and δ_{iee} indicate the electronic or mixed ionic nature of the terms. While $\chi_e = 3.674$ [55] is a constant in the THz region, there exist ionic resonances which lead to the following frequency dependence [59]:

$$\chi_i(\Omega) = \chi_{i0}(1 - \frac{\Omega^2}{\omega_i^2} + \frac{i\gamma\Omega}{\omega_i^2})^{-1}, \tag{2.23}$$

where χ_i =23.36, $\gamma = 0.34\,\mathrm{THz}$ is the ionic damping constant, and $\omega_i/2\pi = 7.6\,\mathrm{THz}$.

The refractive index $n(\Omega)$ and the amplitude absorption $\alpha(\Omega)$ can be calculated from the dielectric function $\epsilon(\Omega)$ according to

$$n(\Omega) = \mathrm{Re}\sqrt{\epsilon(\Omega)}, \tag{2.24}$$

$$\alpha(\Omega) = (\Omega/c)\mathrm{Im}\sqrt{\epsilon(\Omega)}. \tag{2.25}$$

The expression for the dielectric function is calculated from a coupled electron-ion multiple oscillator model [55]:

$$\epsilon(\Omega) = \epsilon_\infty + \sum_k A_k \frac{\omega_k^2}{\omega_k^2 - \Omega^2 - 2i\gamma_k\Omega}. \tag{2.26}$$

Both refractive index and absorption play an important role in the efficiency of the THz generation process. The refractive indices of the fundamental laser pulse and the THz waves have to be matched in order to maximize the interaction length between them. This important issue of velocity matching will be discussed below.

First, let us consider absorption in the crystal. The efficiency of optical rectification by long plane wave pulses neglecting pump absorption, but including THz absorption is given by [55]

$$\eta_{THz} = \frac{2\omega^2 d_{eff}^2 L^2 I_0}{\epsilon_0 n_{pump}^2 n_{THz} c^3} \exp\left(-\alpha_{THz} L/2\right) \cdot \frac{\sinh^2\left(\alpha_{THz}(L/4)\right)}{\left(\alpha_{THz} L/4\right)^2}. \tag{2.27}$$

Here ω refers to the angular difference frequency, d_{eff} is the effective nonlinear coefficient, I_0 the intensity of the pump light, ϵ_0 the permittivity in vacuum, c the velocity of light in vacuum, L the length of the nonlinear crystal, α_{THz} the intensity absorption coefficient for the THz radiation, and n_{pump} and n_{THz} are the refractive indices for the pump and THz pulses, respectively. Two cases for negligible absorption ($\alpha_{THz} L \ll 1$) and large absorption ($\alpha_{THz} L \gg 1$) are considered which result in

$$\eta_{THz} = \frac{2\omega^2 d_{eff}^2 L^2 I}{\epsilon_0 n_{pump}^2 n_{THz} c^3} \qquad (\alpha_{THz} L \ll 1), \tag{2.28}$$

and

$$\eta_{THz} = \frac{8\omega^2 d_{eff}^2 I}{\epsilon_0 n_{pump}^2 n_{THz} c^3 \alpha_{THz}^2} \qquad (\alpha_{THz} L \gg 1). \tag{2.29}$$

In case of a large absorption, the generation efficiency is independent from the crystal length. Therefore, the maximum useful crystal length can be regarded as the penetration depth of the THz radiation α_{THz}^{-1}. For larger distances to the exit surface of the crystal, most of the generated THz radiation will be absorbed before leaving the crystal.

Table 2.1 shows properties of the frequently used crystals for optical rectification GaP, ZnTe and $\mathrm{LiNbO_3}$. It reveals an advantage of ZnTe, as it can be used in a collinear geometry owing to the fact that the refractive indices at a

Material	d_{eff} (pm/V)	n^{gr}_{800nm}	n_{1THz}	α_{1THz} (cm^{-1})
GaP	24.8	3.67	3.34	0.2
ZnTe	68.5	3.13	3.27	0.5
$LiNbO_3$	168	2.25	4.96	17

Table 2.1: Properties of crystals used for optical rectification (from [55]).

pump wavelength of 800 nm and at 1 THz are almost identical. On the other hand, $LiNbO_3$ has the highest nonlinear coefficient of the three considered crystals which results in an enhanced THz generation efficiency. In fact, it was demonstrated that the output energy using $LiNbO_3$ was orders of magnitudes higher compared to ZnTe [60] which cannot be explained by the difference of d_{eff} only. In addition, $LiNbO_3$ has a large bandgap of 3.8 eV [61] making two-photon absorption impossible. In contrast, GaP and ZnTe have smaller bandgaps so that parasitic nonlinear effects such as multiphoton absorption lead to a reduction of the generation efficiency for optical rectification. This is because the carriers created by two-photon absorption significantly increase absorption of the THz radiation. As a consequence, saturation of the THz output energy occurs at much higher pump intensities for $LiNbO_3$ when compared to ZnTe [62]. One drawback of $LiNbO_3$, which can be seen from Table 2.1, is its large absorption coefficient in comparison to other crystals. Therefore, interaction lengths are typically low. In principle, a cooling of the crystal can drastically reduce absorption. However, the reported THz pulse energies from different crystals have shown that the high efficiency of THz generation in $LiNbO_3$ compensates for its large absorption coefficient even for an uncooled crystal.

A further aspect concerning $LiNbO_3$ is its strong photorefraction. In order to prevent the crystal from damage at high pump irradiation, it is usually doped with MgO. For stoichiometric $LiNbO_3$ the necessary doping level is 0.7 % [63]. The absorption coefficient α_{THz} depends on the stoichiometry of the crystal as well as on the doping level. It is smallest for an Mg doping concentration just above the threshold for suppression of photorefraction [64].

2.3.3 THz generation via tilted-pulse-front excitation

In the previous section, the advantageous properties of $LiNbO_3$ as a THz generation crystal due to its high nonlinear coefficient and the large bandgap were discussed. Table 2.1, however, also shows a large difference of the refractive indices in the THz and NIR regions which means that both are propagating with different velocities inside the crystal. When such a crystal is pumped by

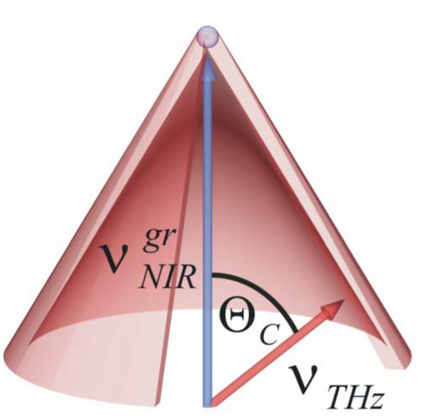

Figure 2.4: Cherenkov radiation which is emitted as a cone having an angle Θ_c with respect to the pump beam. Taken from [55].

a fs laser, THz radiation is still observed referred to as Cherenkov radiation [65]. The emitted radiation propagates away from the pump pulse under an angle Θ_c which is given by

$$\cos\Theta_c = \frac{n_{NIR}}{n_{THz}}. \tag{2.30}$$

For $LiNbO_3$ the values of n_{NIR} and n_{THz} are taken from Table 2.1 for 800 nm and 1 THz, respectively. This results in a Cherenkov angle of $\Theta_c \approx 63°$. While this is a working scheme for THz generation, it has several disadvantages. As can be seen from Fig. 2.4, the radiation is emitted as a cone which makes it hard to collect. In addition, THz radiation can only be generated if the beam waist w of the pump light is significantly smaller than its wavelength λ_{THz} [66]:

$$w \ll \lambda_{THz}. \tag{2.31}$$

Otherwise, THz radiation generated at different lateral positions along the pump pulse would destructively interfere. Therefore, the size of the pump beam cannot be increased in order increase the energy of the pump beam and the resulting THz pulse.

Tilted-pulse-front excitation serves as an alternative scheme to generate THz radiation in materials which have a mismatch of their refractive indices. Fig 2.5 shows that the THz pulses are emitted as a plane wave which is perpendicular to the pulse front of the pump laser. The angle Θ of the pulse front tilt is determined in an equivalent way to that of Cherenkov radiation:

$$\cos\Theta = \frac{v_{THz}^{p}}{v_{NIR}^{gr}}, \tag{2.32}$$

where v_{THz}^{p} refers to the phase velocity of the THz radiation and v_{NIR}^{gr} is the group velocity of the NIR radiation. One important advantage of this scheme is that the spot size can be scaled up in order to increase the THz output energy. The tilt of the pulse front can be achieved by two different methods. A discrete tilt is introduced by a glass echelon which delays different parts of the pump pulse in transverse dimension by different amounts. However, this method suffers from diffractive losses and incomplete pumping of the THz wave path in the crystal [56]. An alternative way is the introduction of a continuous pulse front tilt by a diffractive element such as a grating which is discussed in the following.

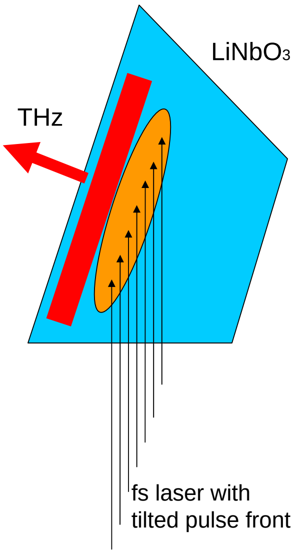

Figure 2.5: Tilted-pulse-front excitation where the projection of the pump pulse velocity is matched to the THz velocity.

According to [56], the angle of the pulse front in the nonlinear crystal is mainly determined by three factors. First, a tilt is introduced by the orientation of the grating and the angle of diffraction off it. This can be seen from Fig. 2.6 where the corresponding parts are marked as a and b. The resulting tilt angle γ can be calculated as

$$\tan\gamma = \frac{\lambda}{d\cos\beta} = \lambda\frac{d\beta}{d\lambda}, \tag{2.33}$$

where λ is the wavelength for a monochromatic beam, d is the distance between two grooves on the grating, and β is the angle of diffraction. A derivation of this equation is found in Appendix A.

Another factor that influences the tilt angle is demagnification by a lens which is used to image the pump beam from the grating to the crystal. Imaging is necessary due to the angular dispersion after diffraction off the grating. Since the spectrum of the laser is spatially dispersed, the pulse durations are much longer compared to the case before diffraction. Thus, the lens serves as a compressor by overlapping the different frequency components spatially in the

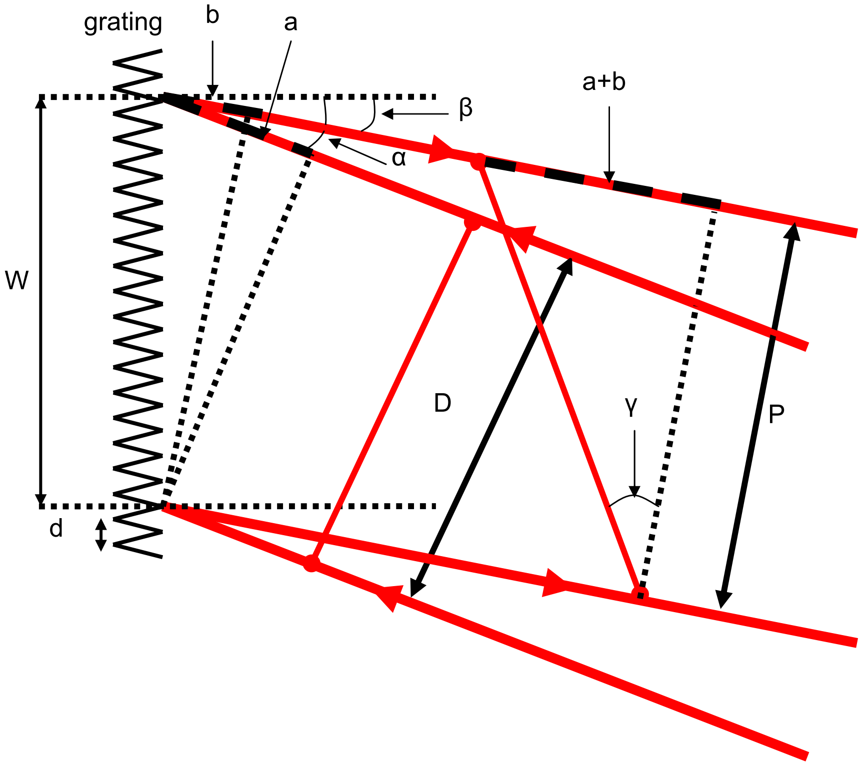

Figure 2.6: A pulse front tilt of a monochromatic beam is introduced by a grating. the upper side of the beam propagates an additional optical path $a + b$ which results in an angle γ between the pulse front and the phase front of the NIR beam.

image plane. For an effective THz generation, the image plane is close to the entrance surface of the crystal. Demagnification due to the imaging process also results in an increased tilt angle which can be seen from Fig. 2.6. While the pump diameter P decreases, the delay $a + b$ remains unchanged. After demagnification by a factor M, Eq. 2.33 reads

$$\tan \gamma\prime = M \cdot \frac{\lambda}{d \cos \beta} = M \cdot \lambda \frac{d\beta}{d\lambda}. \tag{2.34}$$

Finally, the tilt angle $\gamma\prime$ is decreased again when entering the crystal due to the differences in refractive indices in air and in the material. The delay $a+b$ is decreased by a factor n_g. Thus, the tilt angle within the crystal Θ can be calculated from the angle of diffraction β [56]:

$$\tan \Theta = \frac{M}{n_g} \cdot \frac{\lambda}{d \cos \beta} \tag{2.35}$$

Typical parameters for an efficient THz generation in $\mathrm{LiNbO_3}$ are $\Theta = 63^\circ$, $M = 2$, $n_g = 2.25$, $\lambda = 800\,\mathrm{nm}$ and $d = 500\,\mathrm{nm}$ (correlating to 2000 lines/mm). The corresponding angles for the grating orientation and the diffraction are $\alpha = 66^\circ$ and $\beta = 44^\circ$, respectively. This is close to a Littrow configuration where both angles have the same values which yields $\alpha = \beta = 53^\circ$ for the upper parameters. This configuration is most advantageous, because the diffraction efficiency is large.

2.3.4 Electro-optic sampling

The most common technique utilized for the temporal characterization of THz transients is similar to the THz generation by optical rectification. Electro-optic sampling is an optoelectronic technique which exploits the *Pockels effect* (also known as electro-optic effect). It is based on the change of refractive indices of a material which is linear in the electric field. The discussion will start by wave propagation in anisotropic crystals. The following considerations are based on [67, 68, 69, 56].

Wave propagation in anisotropic media

In contrast to an isotropic medium where the polarization $\boldsymbol{P}$ induced by an electric field $\boldsymbol{E}$ is always parallel to the electric field, this is not necessarily the case for an anisotropic medium. While for isotropic media $\boldsymbol{P}$ and $\boldsymbol{E}$ are linked by a scalar susceptibility, the susceptibility becomes a tensor for an anisotropic medium [70]:

$$P_i = \epsilon_0 \chi_{ij} E_j. \tag{2.36}$$

The coefficients of the susceptibility tensor χ_{ij} depend on the choice of the coordinate system relative to the crystal lattice. It is possible to introduce a system where χ_{ij} becomes a diagonal matrix with only three independent entries:

$$\chi_{ij} = \begin{pmatrix} \chi_{11} & 0 & 0 \\ 0 & \chi_{22} & 0 \\ 0 & 0 & \chi_{33} \end{pmatrix}. \tag{2.37}$$

The axes whose choice makes the susceptibility tensor a diagonal matrix are referred to as *principal axes* of the crystal. When not all χ_{ii} components are equal, the material exhibits birefringence accompanied by different refractive indices n_e and n_o for polarizations parallel (extraordinary) and perpendicular (ordinary) to the axis of anisotropy, respectively. Introducing the dielectric permittivity tensor,

$$\epsilon_{ij} = 1 + \chi_{ij}, \tag{2.38}$$

Eq. 2.36 can be rewritten as

$$D_i = \sum_j \epsilon_{ij} E_j. \tag{2.39}$$

The argumentation made for the susceptibility tensor also holds for the permittivity tensor. As a consequence of birefringence, the polarization state of a linearly polarized wave propagating through an anisotropic crystal will not remain invariant. This is only the case if the polarization is parallel to one of the optical axes of the crystal. For any other direction of polarization, the field vector can be split into an extraordinary and an ordinary component which propagate with different velocities through the crystal. In this way, a phase shift between the two components is introduced which leads to a change of polarization after propagation through the crystal.

The Pockels effect

The polarization for high electric fields is written in the form (cf. Eq. 2.20):

$$\begin{aligned} \boldsymbol{P} &= \epsilon_0 \left(\chi^{(1)} \boldsymbol{E} + \chi^{(2)} \boldsymbol{E}^2 + \chi^{(3)} \boldsymbol{E}^3 + \cdots \right) \\ &= \epsilon_0 \left(\chi^{(1)} + \chi^{(2)} \boldsymbol{E} + \chi^{(3)} \boldsymbol{E}^2 + \cdots \right) \boldsymbol{E} \\ &= \epsilon_0 \chi \boldsymbol{E}. \end{aligned} \tag{2.40}$$

One can now relate the refractive index n with applied field to the refractive index n_0 without external field [56]:

$$\begin{aligned} n^2 &= \epsilon = 1 + \chi \\ &= 1 + \chi^{(1)} + \chi^{(2)} \boldsymbol{E} + \chi^{(3)} \boldsymbol{E}^2 + \cdots \\ &= n_0^2 + \chi^{(2)} \boldsymbol{E} + \cdots \\ &= (n_0 + \Delta n)^2 \\ &\approx n_0^2 + 2 n_0 \Delta n. \end{aligned} \tag{2.41}$$

Here the assumption was made that contributions due to higher orders of the field are small. The final expression describes the Pockels effect which is a change in the refractive index of the crystal. Here, the THz field $E_k(0)$ is approximated as being constant in time. The polarization component P_i is in analogy to Eq. 2.21 expressed as

$$P_i^{(2)}(\omega) = 2\sum_{j,k} \epsilon_0 \chi_{ijk}^{(2)}(\omega = \omega + 0) E_j(\omega) E_k(0), \tag{2.42}$$

where $E_j(\omega)$ is the electric field of the optical probe and $E_k(0)$ is the field of the THz wave. Eq. 2.39 can be conversed:

$$E_i = \sum_j \eta_{ij} D_j. \tag{2.43}$$

$\eta_{ij} = \epsilon_{ij}^{-1}$ is the impermeability being related to the electro-optic tensor r_{ijk} by

$$\eta_{ij} = \sum_k r_{ijk} E_k. \tag{2.44}$$

As the tensor η_{ij} is real and symmetric ($\eta_{ij} = \eta_{ji}$), it only contains six distinct terms. It is common to simplify the tensor and to introduce the following nomenclature [71]:

$$\boxed{\begin{array}{c} r_{11k} \longrightarrow r_{1k} \\ r_{22k} \longrightarrow r_{1k} \\ r_{33k} \longrightarrow r_{1k} \\ r_{23k} = r_{32k} \longrightarrow r_{4k} \\ r_{13k} = r_{13k} \longrightarrow r_{5k} \\ r_{12k} = r_{12k} \longrightarrow r_{6k} \end{array}}$$

In order to determine the refractive indices of a crystal, one can introduce the so called *index ellipsoid*. In its most general form it is expressed as [72]

$$\begin{aligned} &\left(\frac{1}{n_x^2} + r_{1k}E_k\right) x^2 + \left(\frac{1}{n_y^2} + r_{2k}E_k\right) y^2 + \left(\frac{1}{n_z^2} + r_{3k}E_k\right) z^2 \\ &\qquad + \left(2r_{4k}E_k\right) yz + \left(2r_{5k}E_k\right) zx + \left(2r_{6k}E_k\right) xy = 1. \end{aligned} \tag{2.45}$$

The change of the coefficients resulting from the application of an electric field E_k then reads

$$\left(\Delta \frac{1}{n^2}\right)_h = \sum_{k=1}^{3} r_{hk} E_k, \tag{2.46}$$

where $k = 1, 2, 3$ represents the direction of the THz field and h runs from 1 to 6 according to the contracted notation of the electro-optic tensor. Eq. 2.46

is rewritten as

$$\begin{pmatrix} (\Delta\frac{1}{n^2})_1 \\ (\Delta\frac{1}{n^2})_2 \\ (\Delta\frac{1}{n^2})_3 \\ (\Delta\frac{1}{n^2})_4 \\ (\Delta\frac{1}{n^2})_5 \\ (\Delta\frac{1}{n^2})_6 \end{pmatrix} = \begin{pmatrix} r_{11} & r_{12} & r_{13} \\ r_{21} & r_{22} & r_{23} \\ r_{31} & r_{32} & r_{33} \\ r_{41} & r_{42} & r_{43} \\ r_{51} & r_{52} & r_{53} \\ r_{61} & r_{62} & r_{63} \end{pmatrix} \begin{pmatrix} E_x \\ E_y \\ E_z \end{pmatrix}. \tag{2.47}$$

The symmetry of a crystal influences the number of independent components of the electro-optic tensor. A widely used crystal for electro-optic sampling is ZnTe which has a zinc blende structure. It is composed of two face-centered cubic lattices shifted by one quarter of the spatial diagonal accompanied by a high degree of symmetry. In fact, the electro-optic tensor of ZnTe has only one independent entry [68]:

$$r_{hk} = \begin{pmatrix} 0 & 0 & 0 \\ 0 & 0 & 0 \\ 0 & 0 & 0 \\ r_{41} & 0 & 0 \\ 0 & r_{41} & 0 \\ 0 & 0 & r_{41} \end{pmatrix}. \tag{2.48}$$

At vanishing electric fields, ZnTe becomes isotropic so that $n_x = n_y = n_z = n_0$. Eq. 2.45 then reads [69]

$$\frac{1}{n_0^2}(x^2+y^2+z^2) + 2r_{41}(E_{THz,1}yz + E_{THz,2}zx + E_{THz,3}xy) = 1. \tag{2.49}$$

When a THz field is applied, it changes the index ellipsoid in size and orientation from its unperturbed state. According to Planken *et al.* [73], two coordinate transformations are necessary to align the index ellipsoid with three new orthogonal axes x'', y'' and z'' (cf. Fig. 2.7). The first transformation is a rotation of 45° around the z axis (001):

$$\begin{aligned} x &= \frac{1}{2}\sqrt{2}(x'-y'), \\ y &= \frac{1}{2}\sqrt{2}(x'+y'), \\ z &= z'. \end{aligned} \tag{2.50}$$

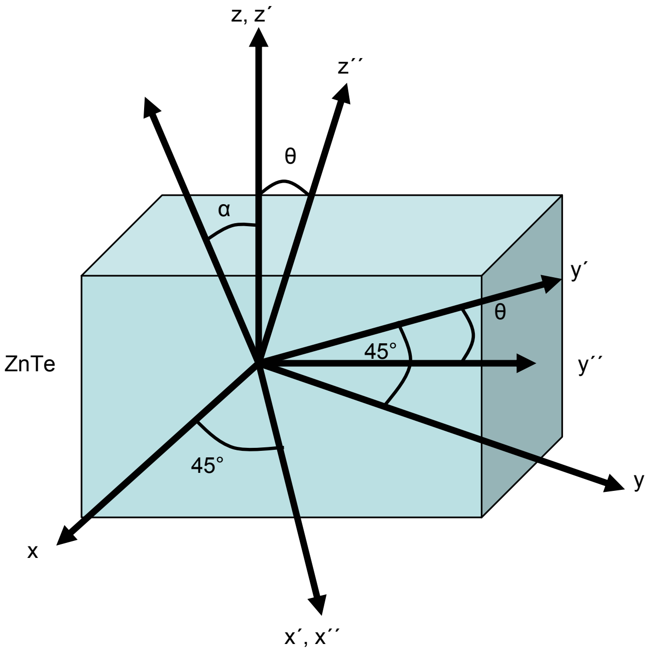

Figure 2.7: Illustration of the two coordinate transformations in ZnTe. α is the angle between the (001) axis and the THz polarization. In the first transformation the system is rotated by 45° around the z axis. In a second step, it is rotated by an angle θ around the x' axis.

The crystal is cut at $\langle 110 \rangle$ which means $E_2 = -E_1$, since the THz pulse propagates along the (110) axis. Using this simplification, the ellipsoid is transformed into

$$x'^2 \left(\frac{1}{n_0^2} + E_{THz,3} r_{41} \right) + y'^2 \left(\frac{1}{n_0^2} + E_{THz,3} r_{41} \right) + \frac{z'^2}{n_0^2} + 2\sqrt{2} E_{THz,1} r_{41} y' z' = 1. \tag{2.51}$$

In a second transformation the system is rotated by an angle θ around the x' axis:

$$\begin{aligned} x' &= x'', \\ x' &= y'' \cos\theta - z'' \sin\theta, \\ z' &= y'' \sin\theta + z'' \cos\theta. \end{aligned} \tag{2.52}$$

The components of the electric field can now be expressed in terms of the angle α: $E_{THz,3} = E_{THz} \cos\alpha$ and $E_{THz,1} = E_{THz}/\sqrt{2} \sin\alpha$, with $E_{THz} = |\boldsymbol{E}_{THz}|$.

The index ellipsoid thus becomes [56]

$$\begin{aligned}
&x''^2\left(\frac{1}{n_0^2}+E_{THz}r_{41}\cos\alpha\right)\\
&+y''^2\left(\frac{1}{n_0^2}-E_{THz}r_{41}(\cos\alpha\sin^2\theta+\cos(\alpha+2\theta))\right)\\
&+z''^2\left(\frac{1}{n_0^2}-E_{THz}r_{41}(\cos\alpha\cos^2\theta+\cos(\alpha+2\theta))\right)=1.
\end{aligned} \tag{2.53}$$

In this equation the mixed terms $y'z'$ vanish under the following condition:

$$\tan 2\theta=-\tan\alpha. \tag{2.54}$$

The coordinate system is rotated around the x' axis by an angle θ which is a function of the angle α between the THz polarization and the (001) axis. For small electric fields ($n_0^2E_{THz}r_{41}\ll 1$), the refractive indices for NIR light propagating along the x'' direction can be approximated as [56]

$$\begin{aligned}
n_{y''}(\alpha)&\approx n+\frac{n^3}{2}E_{THz}r_{41}(\cos\alpha\sin^2\theta+\cos(\alpha+2\theta)),\\
n_{z''}(\alpha)&\approx n+\frac{n^3}{2}E_{THz}r_{41}(\cos\alpha\cos^2\theta+\cos(\alpha+2\theta)).
\end{aligned} \tag{2.55}$$

Since the refractive indices $n_{y''}$ and $n_{y''}$ are different, the electric field polarization components of the probe beam accumulate different optical phases. A probe beam which is circularly polarized before entering the crystal will be elliptically polarized after leaving the medium. The intensity difference ΔI of the corresponding polarization components is calculated by [20]

$$\Delta I(\alpha,\phi)=I_p\sin(2(\phi-\theta))\sin\left(\frac{\omega_0}{c}(n_{y''}(\alpha)-n_{z''}(\alpha))L\right), \tag{2.56}$$

where ϕ is the angle between the polarization of the optical probe beam and the (001) axis of ZnTe, ω_0 is the angular frequency of the probe pulse, and L is the crystal length. Again, for small fields the relation can be simplified using Eq. 2.54 and 2.55:

$$\Delta I(\alpha,\phi)=I_p\frac{\omega n^3E_{THz}r_{41}L}{2c}(\cos\alpha\sin 2\phi+2\sin\alpha\cos 2\phi). \tag{2.57}$$

The term in brackets has a maximum value of 2, when the probe beam and the THz beam have parallel polarizations which are both perpendicular to the (001) axis of the crystal ($\alpha=\phi=-90°$). The maximum signal is denoted as $\Delta I_{max}=\Delta I(\alpha=90°,\phi=90°)$. Numerical values for the electro-optic coefficient and the refractive index of ZnTe are $r_{41}=4.04\,\mathrm{pm/V}$ and $n_0=2.854$

[74], respectively. Assuming a wavelength of $\lambda_0 = 800\,\mathrm{nm}$ ($\omega = 2.36 \cdot 10^{15}\,\mathrm{Hz}$) for the probe beam, the electric field of the THz radiation is calculated by

$$E_{THz}[\mathrm{MV/m}] = \frac{1.36}{L[\mathrm{mm}]} \cdot \frac{\Delta I_{max}}{I_p}, \tag{2.58}$$

which is valid for small intensity changes ($\Delta I_{max} \ll I_p$). Electro-optic sampling can thus be used for mapping the THz electric field transient and to estimate its maximum electric field strength.

2.4 Light-field-driven streak camera

Streak cameras for the temporal characterization of ultrashort light pulses have been employed for several decades already [75, 76]. The measurement principle of a conventional streak camera is illustrated in Fig. 2.8. An XUV pulse hits a photocathode and thereby creates electrons with the same temporal distribution. The electrons propagate perpendicular to a fast varying high voltage such that electrons generated at different times are deflected by different amounts. In this way the temporal distribution of the XUV pulse is transformed into a spatial distribution of electrons which is detected on a fluorescence screen. With the knowledge of this so called streak image as well as the slope of the high voltage it is possible to reconstruct the temporal profile of the XUV pulse. The time resolution of such a streak camera depends on the speed of the field variation, but it is ultimately limited by the spread of the electron transit times due to a spread in their initial momenta [77]. The best resolutions reported for a conventional streak camera are between 200 and 300 fs [78, 79]. This is, however, insufficient for many sources of ultrashort XUV pulses such as free electron lasers or high-order-harmonic radiation where pulse durations in the range from attoseconds to a few tens of femtoseconds are achieved.

The concept of a conventional streak camera can be transferred to a light-field-driven streak camera. Here, instead of a fast varying voltage source, the electric field of an infrared light pulse is exploited for the acceleration of electrons. The basic principle of a light-field-driven streak camera is shown in Fig. 2.9. Free electrons are generated by the XUV pulse typically in a gaseous medium. The electron momenta are decreased or increased by the superimposed infrared light field depending on its phase at the ionization time. Electrons which are generated at different times during the XUV pulse duration are accelerated or decelerated by different amounts. The resulting energy distribution is measured by an electron spectrometer. Thus, the initial temporal distribution is converted into a distribution of kinetic energies. Compared to a conventional streak camera, this arrangement has several advantages. First, the variation of the accelerating field is much faster. When XUV pulses and IR pulses are generated by the same laser, no jitter occurs between them. In addition, electron dispersion effects are prevented, since the final electron kinetic energy is defined already at the time of ionization. As a consequence, the time resolution can dramatically be enhanced.

Light-field-driven streak cameras were first established for measuring the temporal duration of attosecond pulses generated by high-order harmonic processes. The temporal resolution compared to conventional streak cameras was improved by more than three orders of magnitude to below 100 as [15]. A general aspect is that the period of the infrared light field has to be much larger than the XUV pulse duration. Therefore, when measuring pulse durations in the fs range, the typically used NIR streaking fields are no longer

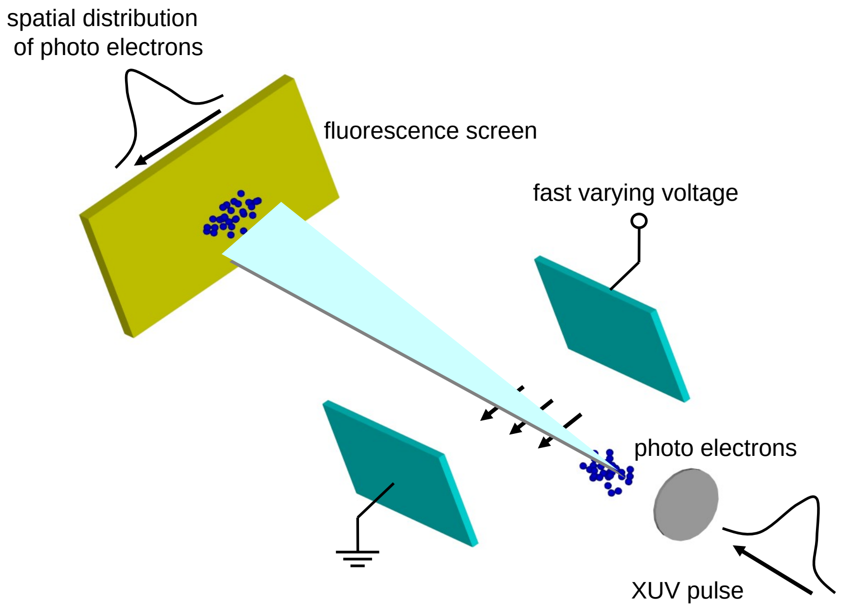

Figure 2.8: Schematic of a conventional streak camera. An XUV pulse generates photoelectrons with the same temporal distribution which are then deflected in horizontal direction by a fast varying high voltage. The temporal structure of the XUV pulse is thus transferred into a spatial distribution of electrons which is made visible on a fluorescence screen.

suitable. Instead, THz fields with larger oscillation periods can be used. The first terahertz-field-driven streak camera was established at FLASH where a temporal resolution of better than 10 fs was achieved [80].

The basic concepts of a light-field-driven streak camera are independent from the streak wavelength. Therefore, a theory of laser-assisted photoionization is discussed in the following which is adopted from attosecond metrology. First, a semiclassical model is presented which also gives intuitive understanding of the involved processes.

2.4.1 Semiclassical model

The following discussion of the light-field-driven streak camera treated in a semiclassical model is based on [81, 82]. Similar to the semiclassical model of HHG, laser-assisted photoionization can be divided into distinct steps. The first step describes the absorption of an XUV photon and the emission of an

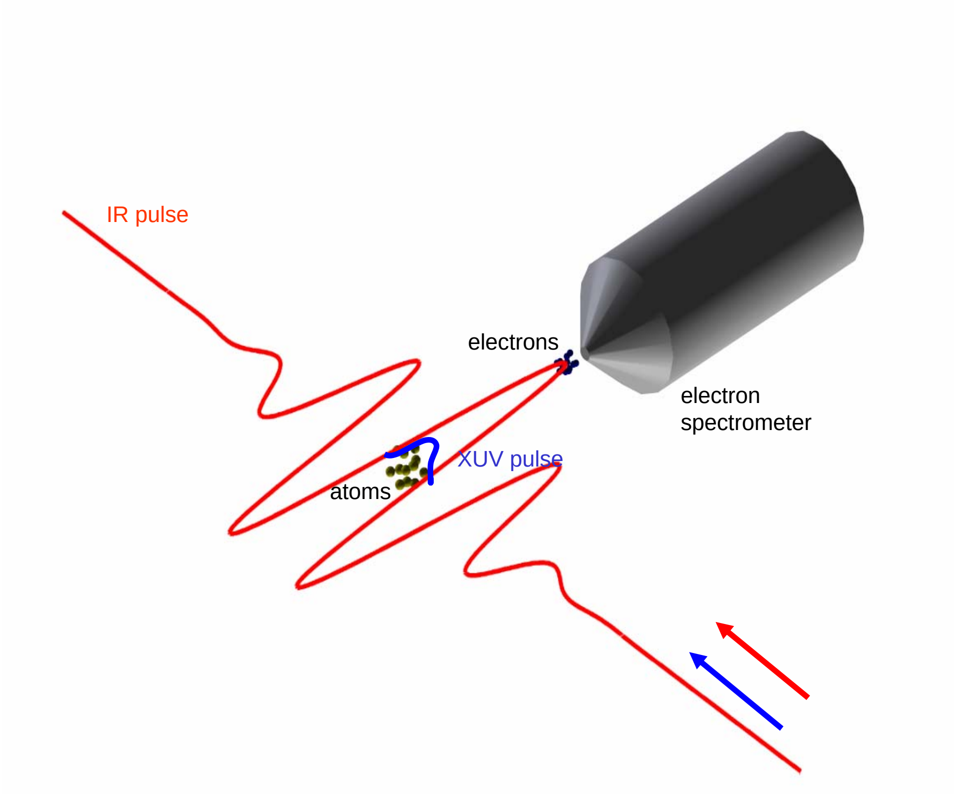

Figure 2.9: Principle of a light-field-driven streak camera where an XUV pulse ionizes rare gas atoms. The generated electrons are accelerated or decelerated by a superimposed infrared light field, depending on the time of ionization. The temporal distribution of the XUV pulse is thus transferred into a kinetic energy distribution which is analyzed by an electron spectrometer.

electron. The initial kinetic energy of the electron is

$$W_0 = \frac{m_e v_0^2}{2} = \hbar\omega_X - I_p, \tag{2.59}$$

where v_0 is the initial velocity of the electron and ω_X is the frequency of the XUV radiation. In a second step, classical mechanics is used to calculate the velocity $\boldsymbol{v}(t)$ in the field, providing that the conditions $U_p \ll \hbar\omega_L$ and $\hbar\omega_X \gg I_p$ hold. For a linearly polarized laser electric field described by $\boldsymbol{E}_L(t) = \boldsymbol{E}_0(t)\cos(\omega_L + \phi)$, the velocity is calculated as [81]

$$\boldsymbol{v}(t) = -\frac{e}{m_e}\boldsymbol{A}(t) + \left(\boldsymbol{v}_0 + \frac{e}{m_e}\boldsymbol{A}_i\right), \tag{2.60}$$

where $\boldsymbol{A}(t)$ is the vector potential for which $\boldsymbol{E}_L = -\partial\boldsymbol{A}/\partial t$. $\boldsymbol{A}_i$ is the vector potential at the time of ionization. The electron undergoes a quiver oscillation

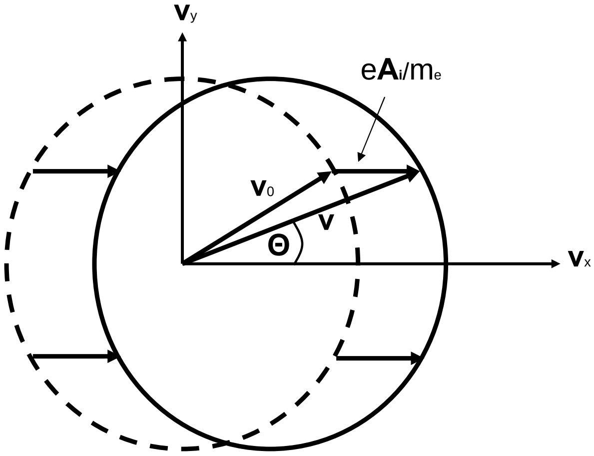

Figure 2.10: Velocity drift for laser-assisted photoionization. The dashed circle represents the velocity distribution without laser field. It is shifted by $e\boldsymbol{A}_i/m$ when a laser field is present. The solid circle shows the final velocity distribution.

which is described by the first term in Eq. 2.60. The second term is the drift velocity which remains after the laser pulse has passed. The effect of the laser field is illustrated in Fig. 2.10. Its influence is not only to change the kinetic energy of the electron, but also to deflect it from its initial propagation direction.

The drift energy is obtained by solving the polynomial equation $\boldsymbol{v}_0^2 = (\boldsymbol{v} + \boldsymbol{A}_i)^2$. When making the approximation of a slowly varying envelope, this leads to [82]

$$W_{kin} = W_0 + 2U_p \cos 2\theta \sin^2 \phi_i \pm \sqrt{1 - \frac{2U_p}{W_0} \sin^2 \theta \sin^2 \phi_i} \sqrt{8W_0U_p} \cos\theta \sin\phi_i, \tag{2.61}$$

where θ is the observation angle with respect to the laser polarization and ϕ_i is the phase of the laser field at the ionization time. For an observation angle parallel to the polarization of the laser ($\theta = 0$), this equation can be simplified:

$$W_{kin,0} = W_0 + 2U_p \sin^2 \phi_i \pm \sqrt{8W_0U_p} \sin\phi_i. \tag{2.62}$$

One can make the additional assumption $U_p \ll W_0$ which is true for most streaking experiments and obtains for the energy shift induced by streaking [16]

$$W_{streak} = W_{kin} - W_0 \approx \sqrt{8W_0U_p} \sin\phi_i = e\sqrt{\frac{2W_0}{m_e}} \frac{E_0(t_i)}{\omega_{IR}} \sin\phi_i = e\sqrt{\frac{2W_0}{m_e}} A_i. \tag{2.63}$$

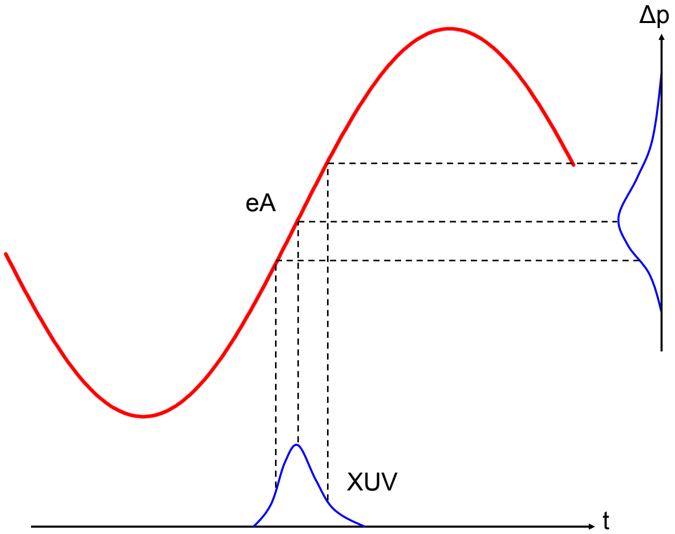

Figure 2.11: The temporal distribution of an XUV pulse is mapped into a momentum distribution of generated photoelectrons. The width of the momentum distribution depends on the XUV pulse duration and the slope of the vector potential.

Here t_i is the time of ionization and ω_{IR} is the frequency of the infrared pulse. At the zero-crossing of the vector potential, an electron experiences no energy shift. For an XUV pulse, however, whose center is overlapped with a zero-crossing of the vector potential, a part of the electrons is slightly accelerated, while another part is slightly decelerated (cf. Fig. 2.11). The width of the resulting momentum distribution depends on the temporal width of the XUV pulse and on the slope of the IR vector potential also referred to as streaking speed s:

$$s = \frac{\partial W_{streak}}{\partial t}. \tag{2.64}$$

In addition, a momentum distribution of the electrons has to be taken into account which results from the bandwidth of the XUV pulse. This can be obtained by switching off the IR field and measuring the momentum or energy distribution. In this way, a time resolution of the light-field-driven streak camera can be calculated in analogy to a conventional streak camera. It is defined by

$$\tau_{res} = \frac{\sigma_{unstreaked}}{s}. \tag{2.65}$$

For this definition the assumption is made that the streak-induced broadening σ_{streak} should equal or exceed the energy spread $\sigma_{unstreaked}$ which is measured when the streaking field is switched off.

2.4.2 Quantum-mechanical model

A quantum-mechanical description of the light-field-driven streak camera is presented according to Quéré *et al.* [82]. First, the ionization of an atom by one photon of the XUV light pulse is regarded which leads to the generation of an electron wavepacket with the same temporal structure as the XUV pulse. Here, the approximation of a single active electron is used which means that any interaction with other electrons is neglected. The transition amplitude $a_{\boldsymbol{p}}$ from the ground state to the final continuum state $|\boldsymbol{p}\rangle$ in atomic units is calculated by

$$a_{\boldsymbol{p}} = -i \int_{-\infty}^{\infty} \mathrm{d}t \boldsymbol{d}_{\boldsymbol{p}} \boldsymbol{E}_X(t) \exp(i(W + I_p)t), \tag{2.66}$$

where $\boldsymbol{d}_{\boldsymbol{p}}$ is the dipole transition matrix element from the ground state to the continuum state, $\boldsymbol{E}_X(t)$ is the XUV electric field, and W is the final energy of the continuum state. The equation shows that the photoelectron spectrum $a_{\boldsymbol{p}}$ is directly linked to the phase and the amplitude of the XUV field spectrum. In fact, when a phase and an amplitude dependency on $d_{\boldsymbol{p}}$ can be neglected, which is reasonable for the cases considered here, the electron wavepacket can be viewed as a replica of the XUV field that ionizes the atom. Thus, the electron wavepacket carries all information about the temporal structure of the XUV pulse.

For the case of the photoemitter being embedded in an infrared laser field, the strong field approximation (SFA) is applied [29]. It neglects effects caused by the ionic potential on the electron after ionization and is therefore in good approximation true for $\hbar\omega_X \gg I_p$. After the XUV and infrared pulses have passed, the transition amplitude $a_{\boldsymbol{p_f}}(\tau)$ for a delay τ between the two pulses is derived from the Schrödinger equation and given by

$$a_{\boldsymbol{p_f}}(\tau) = -i \int_{-\infty}^{+\infty} \mathrm{d}t \boldsymbol{d}_{\boldsymbol{p(t)}} \boldsymbol{E}_X(t-\tau) \exp\left[i \left(I_p t - \int_t^{+\infty} dt' \boldsymbol{p}^2(t')/2 \right) \right]. \tag{2.67}$$

The instantaneous momentum of the electron written in the Coulomb gauge is $\boldsymbol{p}(t) = \boldsymbol{v} + \boldsymbol{A}(t)$. After the infrared field has vanished, the last term of the momentum is equal to zero and the remaining momentum is $\boldsymbol{p_f} = \boldsymbol{p_0}(t) + \boldsymbol{A_i}$. $a_{\boldsymbol{p_f}}(\tau)$ can be understood as the sum of the probability amplitudes of all electron trajectories leading to the same final momentum $\boldsymbol{p_f}(\tau)$. Thus, the photoelectron spectrum is calculated as $S = \left| a_{\boldsymbol{p_f}} \right|^2$. The integral over t in Eq. 2.67 means that the XUV field can ionize the atom at any time t, with the probability amplitude equal to the actual XUV field amplitude, multiplied by the transition matrix element at that time. The last factor in Eq. 2.67 corresponds to the phase which consists of the sum of the phase $I_p t$ accumulated in the fundamental state until time t and the phase accumulated in the vacuum. This last term referred to as *Volkov phase*, is the integral of the instantaneous energy of the electron in the infrared field.

Eq. 2.67 can be rewritten as

$$a_{\boldsymbol{p_f}}(\tau) = -i \int_{-\infty}^{+\infty} \mathrm{d}t \exp[-i\Phi(t)] \boldsymbol{d}_{\boldsymbol{p(t)}} \boldsymbol{E}_x(t-\tau) \exp\left[i(W+I_p)t\right], \tag{2.68}$$

with the phase

$$\Phi(t) = -\int_{t}^{+\infty} dt'(\boldsymbol{p_f}\boldsymbol{A}(t') + \boldsymbol{A}^2(t')/2). \tag{2.69}$$

From a comparison to Eq. 2.66 follows that the infrared field induces a temporal phase modulation $\Phi(t)$ on the electron wavepacket which is generated by the XUV field. By making use of the slowly-varying envelope approximation, the phase can be written as the sum of three terms:

$$\begin{aligned}
\Phi(t) &= \Phi_1(t) + \Phi_2(t) + \Phi_3(t), \\
\Phi_1(t) &= -\int_t^{+\infty} dt U_p(t), \\
\Phi_2(t) &= \frac{\sqrt{8WU_p(t)}}{\omega_{IR}} \cos\Theta \cos(\omega_{IR}t), \\
\Phi_3(t) &= -\frac{U_p(t)}{2\omega_{IR}} \sin(2\omega_{IR}t).
\end{aligned} \tag{2.70}$$

$\Phi_1(t)$ varies on the time scale of the infrared pulse envelope, while $\Phi_2(t)$ and $\Phi_3(t)$ oscillate at the infrared field frequency and its second harmonic, respectively. For $U_p \ll W$ and small observation angles Θ, Φ_2 is the dominant term.

A comparison between the semiclassical and the quantum-mechanical model reveals a close relation between them. According to [82], the classically obtained energy modulation, ΔW, is the derivative of the quantum-mechanical phase modulation $\Phi(t)$: $\Delta W = -\partial\Phi/\partial t$. When the XUV pulses are much shorter than the IR oscillation period, both models are equivavelent and can alternatively be used for the description of the THz-field-driven streak camera.

2.4.3 Reconstruction of the chirp

So far, a chirp of the XUV pulses has not explicitly been considered. It will be shown in the following that the light-field-driven streak camera allows not only

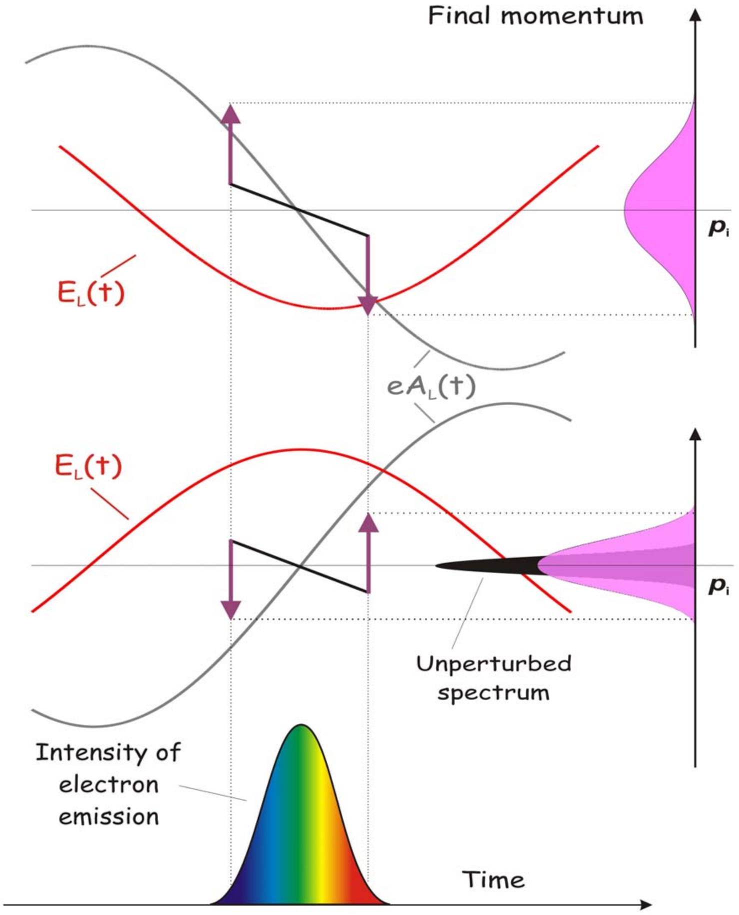

Figure 2.12: Representation of the streak camera principle for a chirped XUV pulse. Depending on the sign of the electric field and the chirp, the streaked photoelectron spectra are broader or narrower with respect to an unchirped XUV pulse (reprinted from [83]).

for a measurement of the XUV pulse duration, but also its linear chirp rate. Hereby, we assume that the XUV pulse has a linear chirp only and neglect a higher-order chirp. The considerations are adapted from [16].

In accordance to Fig. 2.12, an XUV pulse with a negative chirp is considered. The time delay is adjusted such that it is overlapped with a positive slope of the infrared vector potential. In this case, electrons generated at the beginning of the pulse have a slightly higher energy than electrons generated at the end of the pulse. The electrons generated at the beginning of the pulse are, however, decelerated, while the electrons generated at the end of the pulse are accelerated by the electric field. In this way, the resulting photoelectron spectrum is narrower than for an unchirped XUV pulse with the same pulse duration. On the other hand, if the slope of the vector potential is reversed, the corresponding photoelectron spectrum will be broader than for an unchirped pulse. The different signs of the vector potential can experimentally be realized by utilizing two detectors which are located in opposite directions. According to [16], the resulting spectrum is calculated by

$$\sigma_s = \sqrt{\sigma_X^2 + \tau_X^2(s^2 \pm 4cs)}, \tag{2.71}$$

where σ_X is the width of the field-free photoelectron spectrum, and τ_X is the XUV pulse duration. The chirp is accounted for by an effective streaking speed $s_{eff} = \sqrt{s^2 - 4cs}$ which can be regarded as follows: For an unchirped XUV pulse, a chirp is introduced to the electron wavepacket which is given by the streaking speed s. An additional chirp of the XUV pulse c increases or decreases the chirp of the electron wavepacket, depending on the signs of s and c.

In order to determine the pulse duration of a chirped XUV pulse, the measured streaked photoelectron spectral widths for both detectors are deconvoluted:

$$\sigma_{l,r} = \sqrt{\sigma_{s_{l,r}}^2 - \sigma_X^2}, \tag{2.72}$$

where the subscripts l and r refer to the left and right detector, respectively. For the XUV pulse duration follows

$$\tau_X = \sqrt{\frac{\sigma_l^2 + \sigma_r^2}{2s^2}}. \tag{2.73}$$

From this a comparison with Eq. 2.71 allows for a determination of the linear chirp rate:

$$c = \frac{\sigma_l^2 - \sigma_r^2}{8s\tau_X^2}. \tag{2.74}$$

When neglecting higher-order chirp terms, the pulse duration and the chirp of the harmonics can be determined by utilizing the laser-based terahertz-field-driven streak camera.

Chapter 3

Experimental setup

In this Chapter, the experimental setup used in this work is presented. The fs laser system is described in Sec. 3.1, while Sec. 3.2 and 3.3 deal with the generation of high-order harmonic and terahertz radiation. Finally, the experimental setup of the laser-based terahertz-field-driven streak camera is given in Sec. 3.4.

3.1 The fs laser system

The femtosecond laser used in this work for the generation of high-order harmonic and terahertz radiation is a commercial system (Amplitude Technologies). A schematic setup of the different components is shown in Fig. 3.1. In the *oscillator* (Synergy, Femtolasers), a titanium sapphire crystal serves as the active medium. With its large gain width it is capable of generating ultrashort pulses which is achieved by the *Kerr lens passive mode-locking* technique [84]. The laser crystal is pumped by a frequency-doubled diode laser at a wavelength of 532 nm (Verdi V-5, Coherent). Pulses with a bandwidth of 100 nm and a pulse energy of 5 nJ at a repetition rate of 75 MHz are generated. In order to enhance the pulse energy, the method of *chirped pulse amplification* (CPA) is applied [85]. First, the pulses from the oscillator are stretched in time by introducing a chirp. In this way, the intensity is reduced, thus preventing damage of optical components during the amplification process. In the next step, the pulses enter the *regenerative amplifier* where they propagate for several round-trips in a z-shaped cavity. 1000 pulses per second are amplified in a titanium sapphire crystal such that the repetition rate is reduced to 1 kHz. Each pulse is coupled out by a Pockels cell after it has reached its maximum energy. Every 40^{th} pulse is then sent to a different amplification system and can thereafter be used for other experiments. The remaining 975 pulses tra-

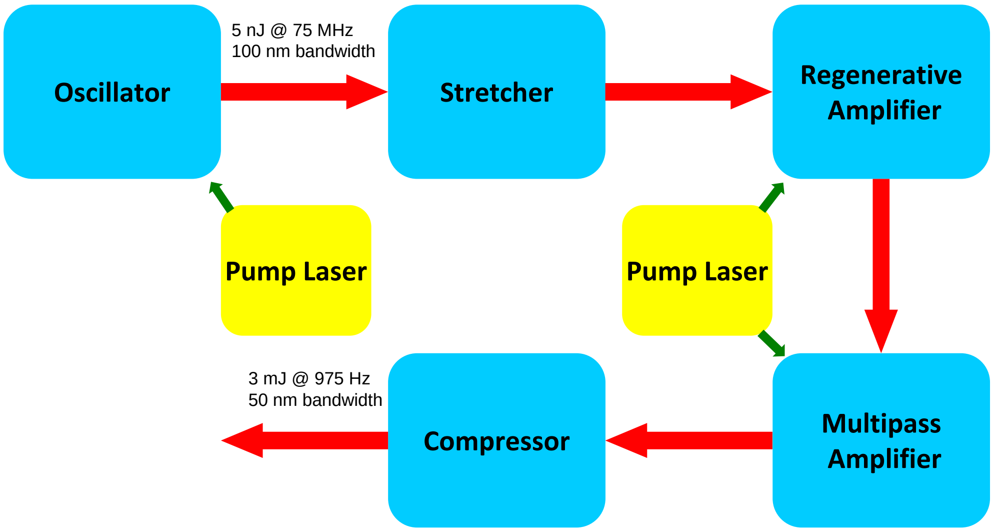

Figure 3.1: Schematic of the fs laser system

verse a *multipass amplifier* where the energy is further enhanced by passing five times through a titanium sapphire crystal. Both amplification crystals are pumped by a diode laser in the green spectral range (DM30-527, Photonics Industries). After amplification, the pulses are recompressed by a pair of gratings to obtain a minimum pulse duration of 25 fs. Each pulse has an energy of about 2.5 to 3 mJ.

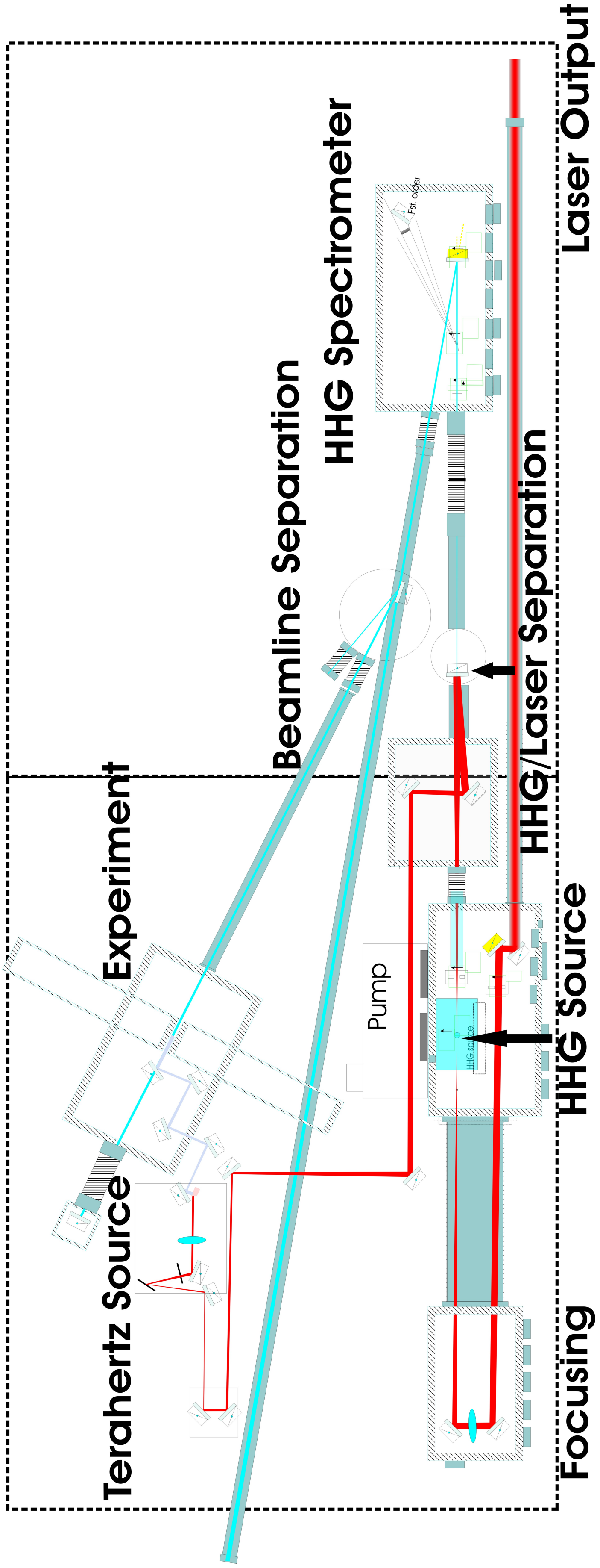

Figure 3.2: Complete setup of the experiment

3.2 HHG setup

For the generation of high-order harmonic radiation, an existing setup could be used. It will be described in the following with its most important features. A more detailed view regarding the source is found in [86], while the detection system is explained in [87]. Further information is also given in [88], where the harmonic radiation was first used for an experiment.

A schematic of the HHG setup is depicted in Fig. 3.3. The whole process occurs in vacuum, since XUV radiation has a very short absorption length in air and other media. The laser beam is coupled into a vacuum tube by a 3 mm thick glass window. It passes an iris which can be used to reduce the beam diameter and thus decrease the pulse energy and increase the focus diameter. Focusing into the gas target is achieved by a lens with a focal length of $f = 1\,\mathrm{m}$ or alternatively by a focusing mirror with $f = 1.5\,\mathrm{m}$. The gas target itself consists of a tube which has a diameter of 3 mm and is filled with neon. Two small holes on the front and back side are adequately burnt into the tube by the laser due to its high intensity close to the focal point. A back pressure of up to 200 mbar compensates for the gas losses through the holes and can also be varied in order to achieve optimum phase-matching conditions. The generated harmonic beam co-propagates with the fundamental beam, but has a distinctly narrower divergence. This circumstance is exploited in order to separate most part of the fundamental beam from the harmonic beam. Therefore, as a part of this work, a spherical concave mirror with a central hole of 3 mm in diameter and a focal length of $f = 1\,\mathrm{m}$ was placed at a distance of 1 m behind the gas tube. The diameter of the fundamental beam at this position is $\approx 10\,\mathrm{mm}$ so that the major part of it is recollimated. On the other hand, the harmonic beam is about 1 mm×3 mm in size and propagates through the hole without distortion. Since the most intense part of the fundamental beam also travels through the hole, it has to be blocked in order to prevent subsequent optical components from damage. This is achieved by a 150 nm thin zirconium filter which transmits a large portion of the XUV beam [89], but blocks most of the

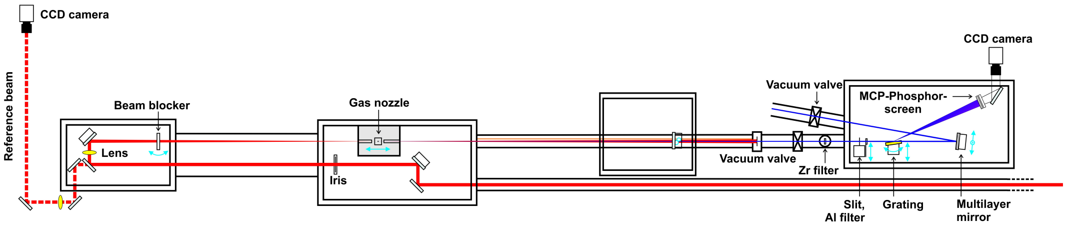

Figure 3.3: Schematic of the generation and detection setup for high-order harmonic radiation

NIR beam.

For the detection of the XUV beam profile, a grating with 600 lines/mm is moved into the beam path. It reflects the zeroth diffraction order onto the detection unit consisting of two microchannel plates (MCPs) and a phosphor screen (APD 2 PS 25/12/10/12 D40:1 P43, Photonis). The XUV radiation causes ionization on the MCPs, and the generated electrons are accelerated by a voltage of up to 2000 V which is applied to the MCPs. The channels are thin and have a direction which is tilted with respect to the acceleration direction. In this way, the interaction of the electrons with the boundaries of the channels lead to the creation of electrons. These are accelerated towards the phosphor screen where a voltage of 3000 V is applied. In this way, fluorescence radiation is emitted and recorded by a charge-coupled device (CCD) camera. Besides the beam profile, also the spectrum can be recorded. For this purpose, a 100 μm wide slit is additionally moved into the beam path in front of the grating. The result is a series of vertical lines on the phosphor screen with the horizontal direction corresponding to the spectral coordinate and the vertical direction to the divergence of the harmonic beam. The spectrometer was designed in such a way that the zeroth and first order diffraction of the grating are visible on the phosphor screen at the same time.

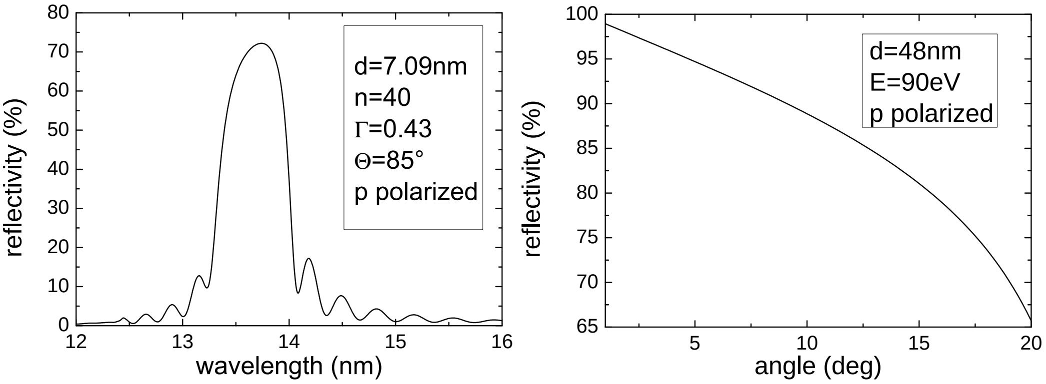

(a) (b)

Figure 3.4: Calculated reflectivities of (a) the multilayer mirror consisting of molybdenum and silicon and (b) the steering mirror made of molybdenum. d corresponds to the layer thickness, N is the number of layers, Γ is the ratio of molybdenum layer thickness/period, Θ is the angle of incidence of the XUV beam with respect to the mirror surface, and E is the photon energy (using [90]).

When moving the slit and the grating out of the beam path, the beam hits a multilayer mirror consisting of 40 alternating layers of molybdenum and silicon. Partial waves that are reflected at different layers can interfere constructively and thus allow for relatively high reflectivities of more than 70 % (cf. Fig. 3.4(a)). Due to its limited bandwidth, the mirror is used to select a certain harmonic order.

Within this work, an additional vacuum chamber was setup which now gives the ability to use the harmonic beam for three different experiments. In the chamber, two different mirrors can be moved into the beam path. When no mirror is moved in, the beam propagates along the original path towards the dichroism experiment [88]. Mirror 1 can be moved in to steer the beam towards the streaking experiment. The mirror consists of a 48 nm thick layer of molybdenum on a fused silica substrate. It is hit by the beam under a small angle of $\approx 8.5^\circ$ for which its calculated reflectivity is about 90 % according to Fig. 3.4(b). When mirror 2 is moved in, the angle of reflection is $\approx 15^\circ$, where the reflectivity is still $\approx 80\,\%$. This beamline can be used for new experiments in the future.

In total, five new vacuum chambers were constructed and included into the beamline system and for the experimental setup. Two of them have a rectangular profile and were fabricated by an alternative method compared to the usual welding technique. The baseplate and the walls made of aluminum were connected with screws and an additional adhesive. During this work, different adhesives were tested in terms of adherence and the achievable vacuum pressure. Among them, an adhesive was tested which is cured by the illumination of ultraviolet light (9001-E-V-3.5, Dymax). However, it was found to be uneligible, since leakages appeared during the pump process. Instead, liquid silicon (TSE399, Momentive) was found to prevent leakages. The achieved vacuum pressures of $1.5 \cdot 10^{-6}$ mbar are sufficient for many applications. In this way, the newly designed vacuum chambers exhibit a cost efficient alternative compared to the standard vacuum chambers.

3.3 THz source

3.3.1 Tilted-pulse-front setup

The THz source which was developed in this work is shown in Fig. 3.5. In a first step, the size of the incoming laser beam is decreased in horizontal direction by means of two cylindrical lenses which are arranged in a Galilean telescope configuration. The first convex and the second concave lens have focal lengths of $f_1 = 200\,\mathrm{mm}$ and $f_2 = -72\,\mathrm{mm}$ which corresponds to a demagnification factor of approximately 2.8. The corresponding size of the beam after the telescope is about $11\,\mathrm{mm}\times 4\,\mathrm{mm}$. A diffraction grating is used to tilt the pulse front of the laser beam. The diffraction efficiency is highest for a p-polarization which conforms to the original polarization direction of the NIR beam. According to Sec. 2.3.3, the angle between grating and the outgoing beam was adjusted to about $53\,^\circ$. The diffracted beam is imaged into a $\mathrm{LiNbO_3}$ crystal making use of an achromatic lens with a focal length of $f = 75\,\mathrm{mm}$. In order to maximize the THz generation efficiency, an achromatic $\lambda/2$ plate rotates the polarization of the laser beam by 90° to be parallel to the optical axis of the crystal. The beam size in the image plane is approximately 6 mm

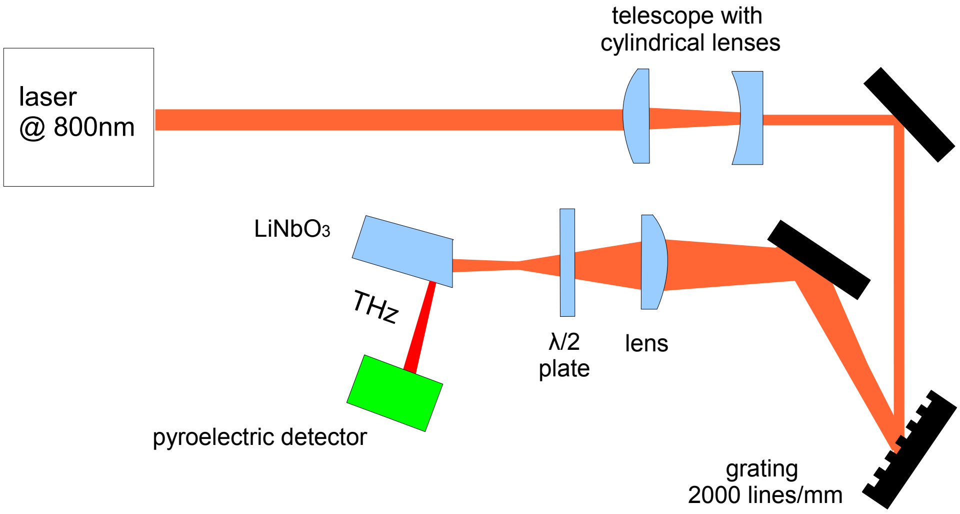

Figure 3.5: Tilted-pulse-front setup for THz generation. The pulse front is tilted by a diffraction grating and imaged onto a $\mathrm{LiNbO_3}$ crystal. The THz radiation is emitted in a direction perpendicular to the pulse front of the NIR beam.

in vertical direction and 2.5 mm in horizontal direction which corresponds to an intensity of 0.7 TW/cm^2. In comparison to a circular beam profile this has two advantages. The effective distance that the THz beam propagates within the crystal is reduced (cf. Fig. 3.6), thereby decreasing THz absorption. According to [64], this is of special importance for higher frequencies for which the absorption coefficient increases. In addition, calculations have shown that the terahertz generation efficiency drastically varies along the transverse beam profile [91]. It has a maximum at the center of the beam and decreases outwards. This effect is explained by the setup where a lens is used to image the diffracted beam from the grating onto the crystal. In this way, the different wavelengths experience a different group delay which leads to an elongation of the pulse duration varying across the beam profile. It is therefore advantageous to keep the pump spot small in horizontal direction. On the other hand, the variation of the pump pulse duration in vertical direction was calculated to be much smaller so that no additional demagnification is necessary. This is beneficial, because the power density of the pump laser on the crystal reaches a saturation level for the generation of THz radiation at about 1 TW/cm^2. By keeping the beam area constant, it is thus possible to reduce the beam size in horizontal direction, while at the same time elongating it in vertical direction.

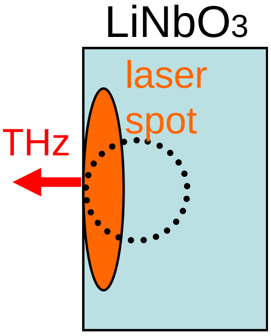

Figure 3.6: The elliptical shape of the NIR beam (orange) leads to a decreased absorption of the THz radiation, since the effective distance that the THz beam propagates within the crystal is reduced. The dotted line shows the laser beam profile with the same area, but without demagnification in horizontal direction.

For the optimization of the THz source it is important to introduce a sufficient number of degrees of freedom to the system. Therefore, the grating and the crystal are placed on translation stages in order to adjust the angle of the pulse front tilt and the distance of the image plane with respect to the crystal. In addition, the crystal is set on a rotation stage to optimize it for the entry and exit of the pump and THz beams, respectively. Also the distance between the lenses of the telescope can be varied. The optimization is then done in an iterative process by making use of the different degrees of freedom. For the optimum result this may lead to a long alignment process.

Measurement of THz parameters

The pulse energy of the THz radiation is measured by a pyroelectric detector after blocking scattered pump light by a 3 mm thick teflon plate. According to App. C, the transmission of this plate at 1 THz is between 85 and 90 %. The absorption of radiation leads to a temperature difference between the two electrodes of the detector which results in a voltage difference. A 2 mm×2 mm pyroelectric detector (LIE 301, Infratec) is utilized whose signal is amplified by a charge sensitive preamplifier module (CR 110, FAST ComTec). A calibration of this detector was performed only for wavelengths of up to 110 μm [92]. In addition, a 2 mm×3 mm pyroelectric detector calibrated in the THz range by the manufacturer (Microtech Instruments) could be borrowed for measuring the absolute energy and for calibrating the detector from Infratec for larger wavelengths. It turned out that an oscilloscope amplitude of 0.5 V from the amplified Infratec detector corresponds to a pulse energy of 1.3 μJ.

A pyroelectric array camera (Pyrocam III, Ophir) could be borrowed for measuring the THz beam profile. It consists of an array of 124×124 elements which are spaced by 100 μm.

3.3.2 Electro-optic sampling

For measuring the time-dependent THz electric field, the method of electro-optic sampling is utilized. Fig. 3.7 shows the typical setup. After leaving the crystal, the divergent THz beam is recollimated by a teflon lens with a focal length of 200 mm. While the 2.3 mm thick lens leads to an additional absorption of about 10 % (cf. App. C), it turned out to be advantageous for the alignment of the whole system. In contrast to a recollimation making use of a mirror in a non-collinear geometry, it is easily possible to change the distance between lens and crystal for an optimization process. The recollimated THz beam is then focused by a parabolic mirror ($f = 100$ mm) onto a ZnTe crystal with a thickness of $L = 0.3$ mm, which serves as the electro-optic crystal. A part of the pump beam (≈ 8 %) is coupled out by a pellicle beam splitter and used as a probe beam. It passes a delay stage in order to vary the overlap between probe and THz beams. The probe beam is focussed onto the crystal, and both beams are overlapped again by a second pellicle beam splitter. A cube polarizer splits the probe beam into two parts which are solely s and p-polarized, respectively. The intensities of both beams are recorded with two photodiodes. Without THz field, a $\lambda/4$ plate is adjusted such that the intensities on both diodes are the same. The difference signal is then recorded while varying the delay. This scheme is referred to as *balanced detection* and has the advantage that it is insensitive to laser noise. In addition, the signal

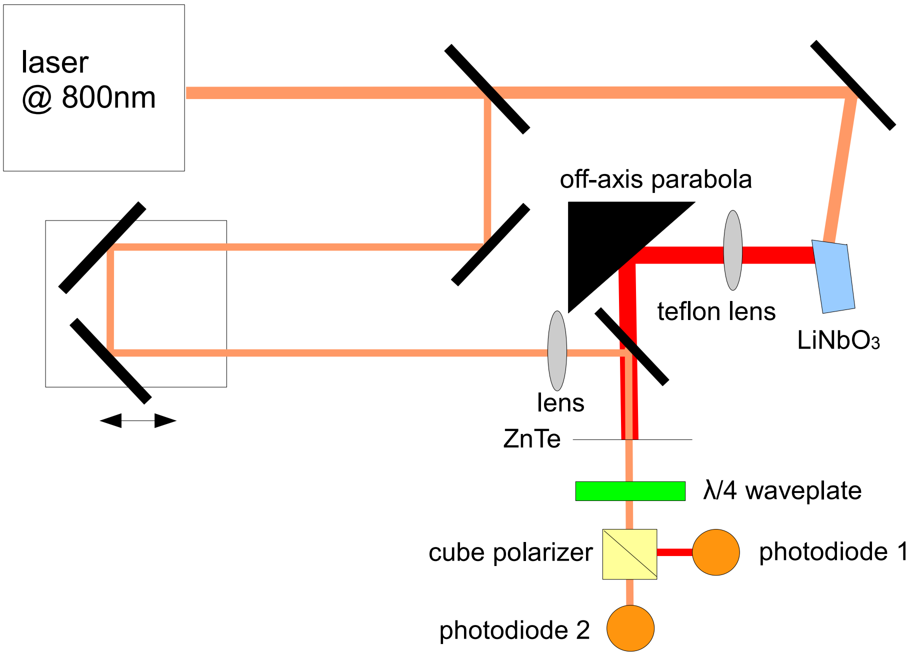

Figure 3.7: Setup for electro-optic sampling. The THz and probe beams are focused onto the electro-optic crystal ZnTe. The polarization of the probe beam is analyzed with a cube polarizer and two photodiodes.

is increased by an additional factor of 2.

It has to be noted that the focusing geometry for the THz beam is not easy to align. Due to the non-collinear geometry of the THz generation process, a pre-alignment of the THz beam path using the NIR beam is not possible. Instead, the parabolic mirror was pre-aligned backwards starting from the THz focal point to the crystal by making use of a helium-neon laser. Therefore, the teflon lens had to be removed. The exact alignment including the teflon lens was then done by placing the pyroelectric detector in the focal point of the parabolic mirror.

3.4 Laser-based THz-field-driven streak camera

The generated XUV and THz pulses are used for the laser-based terahertz-field-driven streak camera. As can be seen from Fig. 3.8, both pulses propagate collinearly towards the gas target. The polarization of the THz pulse is first rotated to p-polarization by a periscope. The beam is then guided by several copper mirrors and enters the vacuum chamber of the experiment through a 3 mm thick polymer window (Topas). The transmission of the window was measured to be about 90 %. Focusing onto the gas target is done by a 90 ° off-axis parabolic mirror (f = 100 mm). The XUV pulse propagates below the gas nozzle and and is reflected by a spherical multilayer mirror with a focal length of $f = 500$ mm. For optimal matching of the multilayer bandpass, the coating is identical to that of the planar multilayer mirror described in Sec. 3.2. The beam is focused upwards under an angle of 8 ° with respect to the incoming beam and passes through a 2 mm hole in the parabolic mirror to be superimposed with the THz pulse. The focus size of the harmonic beam can be determined by a CCD camera which is coated with a thin phosphor layer. As target media, the rare gases neon, xenon and krypton are used which are provided by a gas nozzle. For alignment purposes, a pyroelectric detector can be moved to the position of the target, while moving out the gas nozzle at the same time. It is used to adjust the focal position of the THz beam. For a pre-alignment, the pyroelectric detector can also be used to measure the NIR beam which is transmitted by the zirconium filter and co-propagates with the XUV beam. This is advantageous, since measurements with the phosphor-coated camera revealed that the foci of the NIR beam and the XUV beam are displaced by only about 100 μm. Therefore, when the NIR beam and the THz beam are coincidentally measured on the pyroelectric detector, a good spatial overlap of the THz and XUV beam is given. In order to pre-align the temporal overlap, an electro-optic crystal is placed at the target position. The NIR beam co-propagating with the XUV beam was used to probe the THz field. The pump pulse for the THz generation was delayed to obtain the temporal overlap. With the help of these pre-alignment methods, the streaking signal was found without any further scanning. In the following, a more comprehensive treatment of the gas feeding and the electron detection is given.

3.4.1 Gas feeding

The gas for the streaking experiment is provided by a capillary tube into the interaction zone. It is made of stainless steel, has a length of 50 mm and an inner diameter of 0.12 mm. A fine metering valve is used to regulate the gas

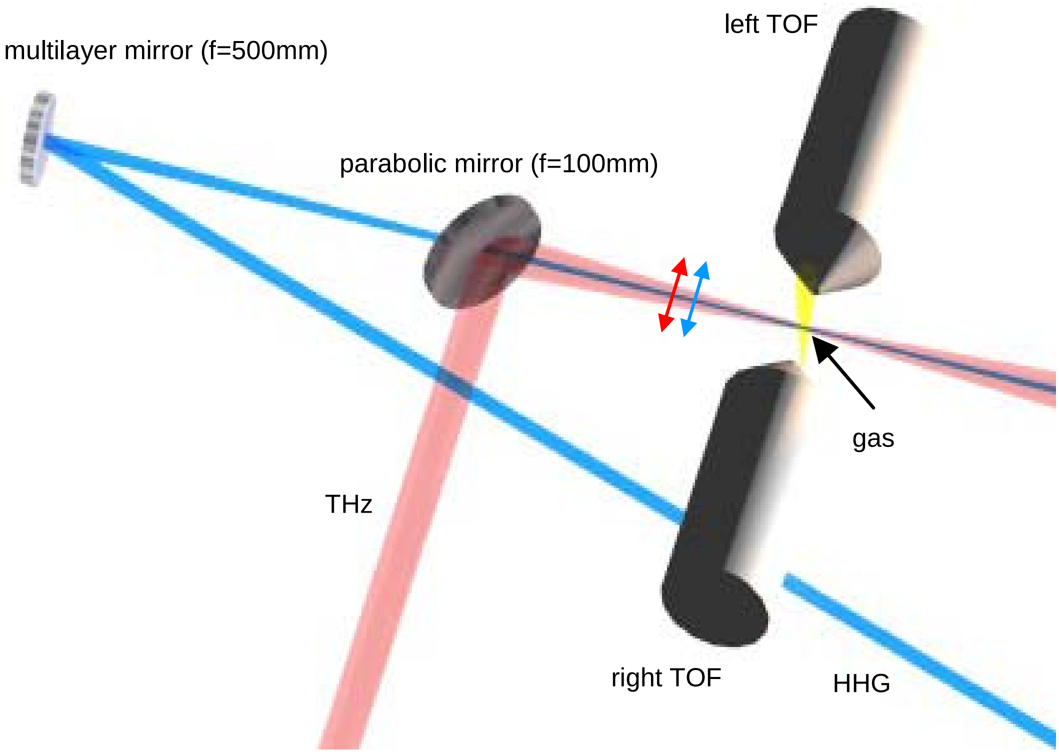

Figure 3.8: Schematic of the laser-based THz-field-driven streak camera. The THz and the XUV beams propagate collinearly and are both focused into the gaseous medium which is provided through a gas nozzle. The kinetic energies of the photoelectrons are measured with two time-of-flight spectrometers.

flow. The background pressure inside the vacuum chamber is $2 \cdot 10^{-6}$ mbar without gas feeding, and the valve is used to adjust a maximum background pressure of $5 \cdot 10^{-4}$ mbar. While it is favorable to increase the number of atoms interacting with the XUV pulse, a limit is set by a pressure of about $1 \cdot 10^{-5}$ mbar that should not be exceeded for the micro-channel plates used in the time-of-flight (TOF) spectrometers. Therefore, the spectrometers are differentially pumped by separate turbomolecular pumps, and the outer surfaces of the TOFs are connected to the walls of the vacuum chamber by plastic foils in order to reduce the gas flow from the chamber to the TOFs.

The gas density distribution after exiting the nozzle is important, because it determines the length of the interaction zone of the atoms and XUV pulses. During propagation through the interaction zone, the phase of the THz pulse is changed owing to the Gouy phase shift (cf. App. A) which leads to a blurring of the XUV pulse duration measurement. Therefore, the length of the interaction zone has to be made as short as possible. The distance between the top of the gas nozzle and the center of the THz beam is about 0.5 mm and cannot be further decreased, because otherwise the capillary disturbs the THz beam due to an antenna effect. The length of the interaction zone is measured by scanning the gas nozzle in transverse direction with respect to the XUV beam and recording the number of electrons that induce a TOF signal at each position. When making the additional assumption that the XUV focus size is small compared to the transverse size of the gas flow, the interaction zone length in the longitudinal direction can be inferred due to symmetry reasons.

3.4.2 Time-of-flight spectrometer

Two time-of-flight spectrometers are used to measure the kinetic energies of the electrons generated by the XUV pulse and accelerated or decelerated by the THz field. In the front part of each TOF, six electrostatic lenses collimate the electron beam in order to increase the transmission and time resolution of the TOF. In this way, electrons with angles of up to ±16 ° with respect to the TOF axis are detected. After propagation through a tube, the electrons hit on an array of two MCPs, where for each electron 10^6 to 10^7 secondary electrons are generated. These secondary electrons then induce a current signal on an anode, which is coupled out by a capacitor and recorded by an oscilloscope. The kinetic energy of the electrons can be calculated from the time of flight t according to the following equation:

$$W_{kin} = \frac{m_e l_{eff}^2}{2(t-t_0)^2} - U. \tag{3.1}$$

l_{eff} is the effective distance which the electrons propagate in the tube. It may deviate from the geometrical distance of 445 mm due to the electrostatic lenses which account for an additional acceleration for a short time. U refers to the retardation voltage which can be applied to the tube in order to increase the time resolution in a certain energy range. The parameters l_{eff} and U as well as the start time t_0 are inferred from simulations of the electron trajectories which have been carried out in [16] for identical TOFs using the simulation program SIMION [93]. As a result, the transmission function depends on the initial kinetic energy and reaches a maximum value, when the initial energy is about 78 eV and a retardation voltage of -50 V is applied. In this case, almost all electrons, which started at angles of up to ±16 ° with respect to the TOF axis, reached the detector. If the initial energy is varied by a few eV, which is true for a single line in the spectrum, the transmission changes only slightly. However, when the deviation is more than 10 eV, the drop of the transmission has to be taken into account for the analysis of the data. This is particularly important when comparing streaked and unstreaked spectra. The energetic resolution was also simulated. Therefore, a number of 500 electrons with the same initial kinetic energy was assumed which were spread over the interaction zone length of 1 mm and entered the detector at angles of up to ±16 °. After propagation through the tube, the calculated kinetic energies were spread. The width of the energy distribution was 0.3 eV which can be regarded as the theoretical energy resolution of the spectrometer.

Chapter 4

Characterization of the THz radiation

In this Chapter, a characterization of various THz pulse parameters is presented. Starting with general properties including the pulse energy and focus size in Sec. 4.1, electro-optic sampling results of the field transient and the calculated spectrum are given in Sec. 4.2. Finally, Sec. 4.3 deals with the characterization of the THz vector potential via the streaking technique.

4.1 General properties

4.1.1 Pulse energy

Estimations for the laser-based terahertz-field-driven streak camera made at the beginning of this work showed that the achieved THz conversion efficiencies given in the literature are not sufficient for obtaining time resolutions which are comparable to the results obtained at FLASH. Therefore, an improvement of the generation efficiency was realized in this work by different means.

For a measurement of the THz pulse energy behind the $LiNbO_3$ crystal, the pyroelectric detector from Infratec was shifted horizontally and vertically in steps of 2 mm and the measured energies were summed up. This was necessary, since the THz beam size is larger than the detector size of 2 mm×2 mm. The corresponding total energy over an area of 10 mm×10 mm is 4.2 μJ. In comparison, the pump pulse energy is 2.0 mJ after losses at the vacuum window, several lenses and mirrors as well as the diffraction grating. This corresponds to a THz generation efficiency of $\eta = 2.1\,‰$. The value is two times higher than the best conversion efficiency reported for THz generation in $LiNbO_3$ so far

[50]. The enhancement of the efficiency for the system setup in this work can at least partly be explained by the elliptical pump beam shape which reduces absorption of the THz radiation inside the crystal.

However, the measured energy is only the transmitted fraction of the THz radiation. Due to the large refractive index of $n_L = 4.96$ for $\mathrm{LiNbO_3}$ in the THz region, a significant part of the radiation is reflected: $R = (n_L - n_{air})^2/(n_L + n_{air})^2 = 44\,\%$. The calculated THz energy before exiting the crystal is $7.5\,\mu$J which corresponds to a generation efficiency of $\eta = 3.75\,‰$. Therewith, the photon efficiency is $\eta_{ph} = \eta \cdot \lambda_{THz}/\lambda_{pump} = 117\,\%$, where $\lambda_{THz} = 250\,\mu$m (cf. Sec. 4.3). On a first view, a conversion efficiency larger than 100 % seems to be surprising. It becomes understandable, when the THz generation is considered as a process where a photon with a frequency lying within the bandwidth of the fs laser decays into a THz photon plus a red-shifted NIR photon. Now, if the interaction length between pump and THz pulse is long enough, the red-shifted photon can on its part generate another THz photon plus a photon which is further shifted to the red part of the spectrum. This process is also referred to as a cascaded $\chi^{(2)}$ process [94]. According to this picture, the conversion efficiency can be calculated from the red-shift of the laser spectrum, assuming that the shift solely originates from the THz generation process. For the THz source setup in this work, the red-shift was obtained by measuring laser spectra after propagation through the $\mathrm{LiNbO_3}$ crystal for two different cases. In the first case, the polarization of the pump beam was rotated by 90 ° to obtain optimum THz generation. In the second case, the $\lambda/2$ plate was adjusted such that the polarization was perpendicular to the optical axis of the crystal in order to suppress THz generation. The difference of the spectral moments in these cases yields a red-shift of 4.6 nm. On the other hand, the generation of one photon with a frequency of 1.2 THz corresponds to a red-shift of only 2.6 nm. This means that in average each NIR photon generates more than one THz photon. The calculated photon efficiency is 177 %. The larger red-shift measured in the current work when compared to the red-shift of 2.6 nm reported in [20] indicates that not only absorption is reduced, but also the initial THz generation efficiency is increased. One reason for this might be a reduced THz absorption which is achieved for elliptical pump pulses with a small diameter in transverse direction (cf. Sec 3.3). It is also possible that by more or different degrees of freedom which have been introduced to the source, the optimization process is more efficient. This eludes a comparison, however, since no information concerning the optimization process is given for other sources in the literature.

After recollimation and focusing of the THz beam, the measured pulse energy is $1.7\,\mu$J which corresponds to a beamline transmission of 40 %. This reduced energy can partly be explained by absorption in the teflon lens, the incoupling window to the vacuum and the water which is contained in air. Furthermore, some components of the radiation might not be recollimated to a parallel beam or not even hit the lens. Finally, even in the focal point a small

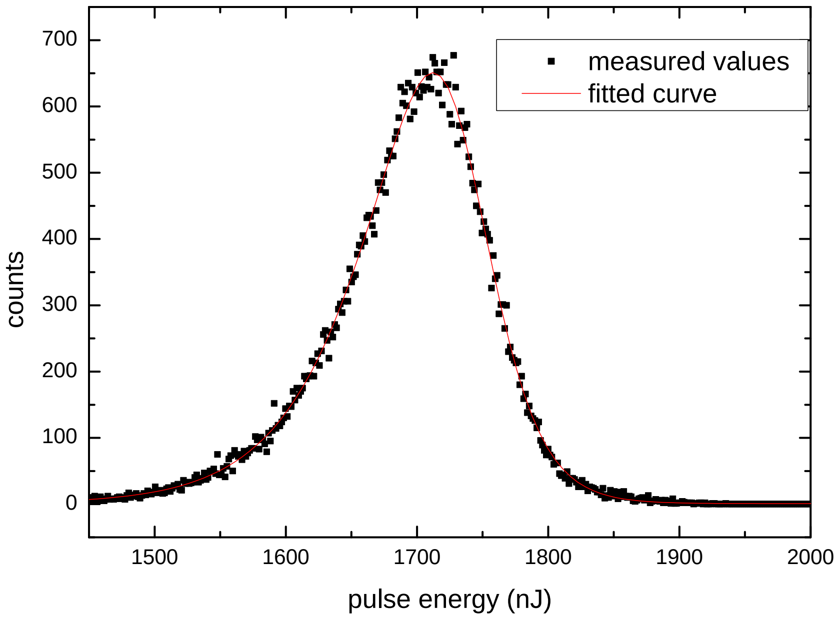

Figure 4.1: Histogram of the fluctuations of the THz pulse energy

part of the radiation does not hit the 2 mm×2 mm active area of the detector.

An important aspect of the THz radiation is the stability of its pulse energy. Therefore, pulse energies of 10^5 shots were recorded in a histogram (Fig. 4.1). The measured data are fitted by an asymmetric double sigmoidal function. The distribution has a full width at half maximum (FWHM) value of $0.12\,\mu$J which corresponds to a relative fluctuation of 7 %. In comparison, the fluctuations of the laser intensity are only $(3-4)\,\%$ [88]. Thus, the nonlinear THz generation process enhances the existant fluctuations or introduces additional fluctuations by other effects such as shifts in the spectrum of the laser. The histogram in Fig. 4.1 has an asymmetric shape which means that deviations from the peak value are larger on the lower energy side.

4.1.2 Divergence and focus size

The divergence of the THz beam after leaving the crystal was measured by placing a pyroelectric array camera at different distances from the crystal and determining the corresponding beam sizes. The values of the divergence in horizontal and vertical directions are 2.8 ° and 1.3 °, respectively which is in accordance with other values reported [95, 55]. Also the fact that the horizontal

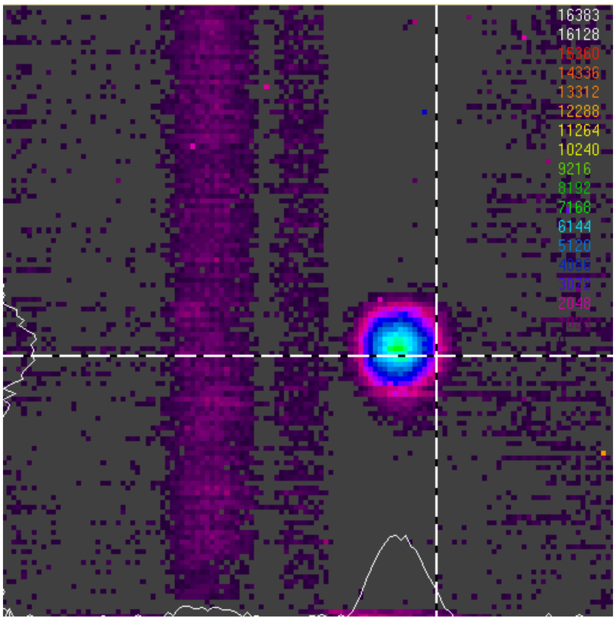

Figure 4.2: Pyrocam image of the focused THz beam

divergence exceeds the horizontal divergence has been observed before [50]. A possible explanation is that different spectral components of the THz pulse propagate at different angles with respect to the laser beam direction owing to spectral dispersion in the $LiNbO_3$ crystal. In addition, the pulse front curvature is expected to vary during propagation through the interaction zone. This effect is larger in horizontal direction compared to the vertical direction. Since the THz pulse propagates in perpendicular direction to this varying pulse front, a larger angular spread of the THz radiation is observed in transverse direction.

Fig. 4.2 shows an image of the THz beam after recollimation by the teflon lens and focusing with the parabolic mirror. The beam has a FWHM diameter of about 1 mm. A more precise derivation of beam parameters can be made from a focus scan along the longitudinal axis z which is depicted in Fig. 4.3. w corresponds to the beam radius, where the amplitude is decreased to $1/e$. A fit for the horizontal direction yields a beam waist radius of $w_0 = 0.7\,\mathrm{mm}$ and a Rayleigh length of $z_R = 9.8\,\mathrm{mm}$. It has to be noted that different frequency components of the single-cycle THz pulses are likely to have different values for their beam waists and Rayleigh lengths. Strictly speaking, these parameters have to be measured separately for the different frequency components. This is, however, hard to realize experimentally.

No fit could be performed for the vertical direction of the beam which is due to insufficient data which were taken during the short time the pyroelectric array camera could be borrowed. It is obvious from Fig. 4.3 that the minimum beam radius in vertical direction is smaller. It can again be argumented that different spectral components propagate at different angles which leads to a

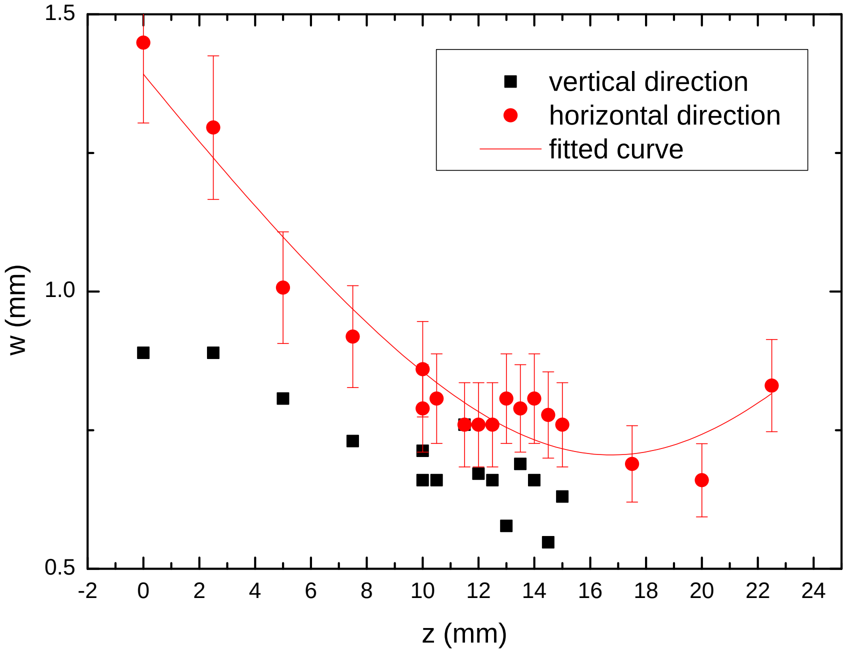

Figure 4.3: Focus scan of the THz beam, where z corresponds to the longitudinal coordinate and w is the beam radius.

deterioration of the focusability in horizontal direction.

4.1.3 Polarization

The polarization of the emitted THz radiation is important for the streaking experiment. After exiting the crystal it is expected to be parallel to the optical axis of the crystal which corresponds to an s-polarized beam. A periscope is used to rotate the polarization such that it is parallel to the polarization of the XUV beam. In order to verify that the polarization is rotated by the correct angle, a free-standing wire-grid polarizer was utilized. It consists of a regular array of thin metal wires. If the THz field is parallel to the wires, the electrons on the wire can move freely along the wire direction responding to the incident field. In this case, the polarizer behaves like a typical metal surface, thus reflecting most of the incident beam. The movement of the electrons in the direction perpendicular to the wire, however, is highly restricted so that for a perpendicular direction most of the THz intensity is transmitted. Fig. 4.4 shows the transmission dependence on the rotation angle θ of the polarizer, where $\theta = 0°$ corresponds to a vertical arrangement of the wires. In this case, the transmission T reaches its maximum, thus indicating a good agreement with the expected p-polarization of the THz pulse. The measurement is in

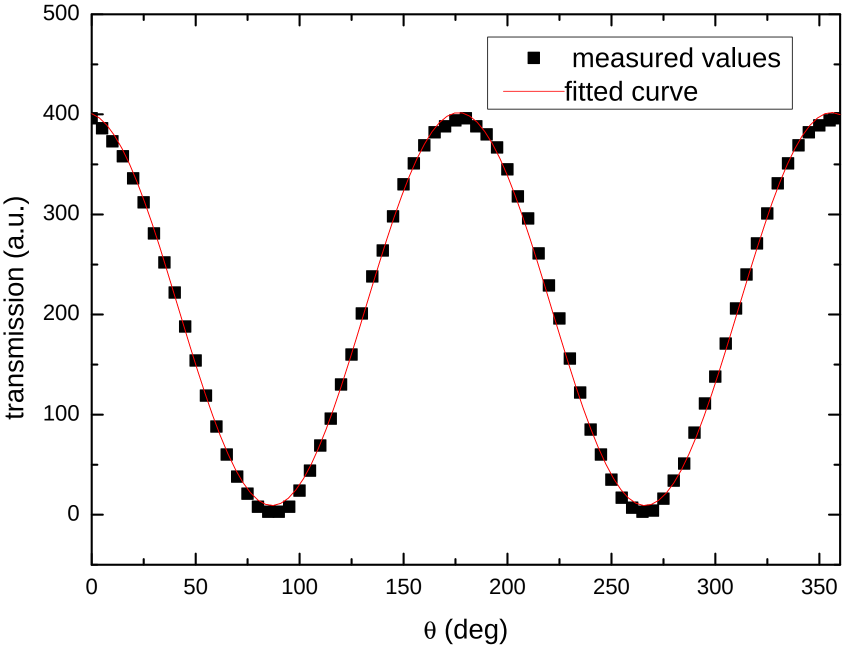

Figure 4.4: THz transmission dependence on polarizer rotation angle θ exhibiting a linear polarization of the radiation

good agreement with the relation $I(\theta) = \sin^2(\theta)$ which corresponds to the fitted curve in Fig. 4.4.

4.2 Electro-optic sampling

The temporal and spectral properties of the THz pulses were investigated by electro-optic sampling. Fig. 4.5 depicts a delay scan of the measured difference signal between the THz and the probe pulse showing the single-cycle behavior of the THz pulses. It has one main peak in the positive direction and two minor peaks in the negative electric field direction. A part of the THz radiation is reflected at the back side of the electro-optic crystal and again at the front side so that an echo of the signal is visible in the delay curve. For a 0.3 mm thick ZnTe crystal this corresponds to a delay of $\tau = 2 \cdot n_{ZnTe} \cdot 0.3\,\mathrm{mm}/c = 6.5\,\mathrm{ps}$ at which a smaller replica of the pulse appears in Fig. 4.5. The oscillations in the range between 2 and 10 ps are most likely due to a damped oscillation in the THz generation crystal. There is a further oscillation at about −6.5 ps which can be attributed to an echo of the probe pulse being reflected within the crystal.

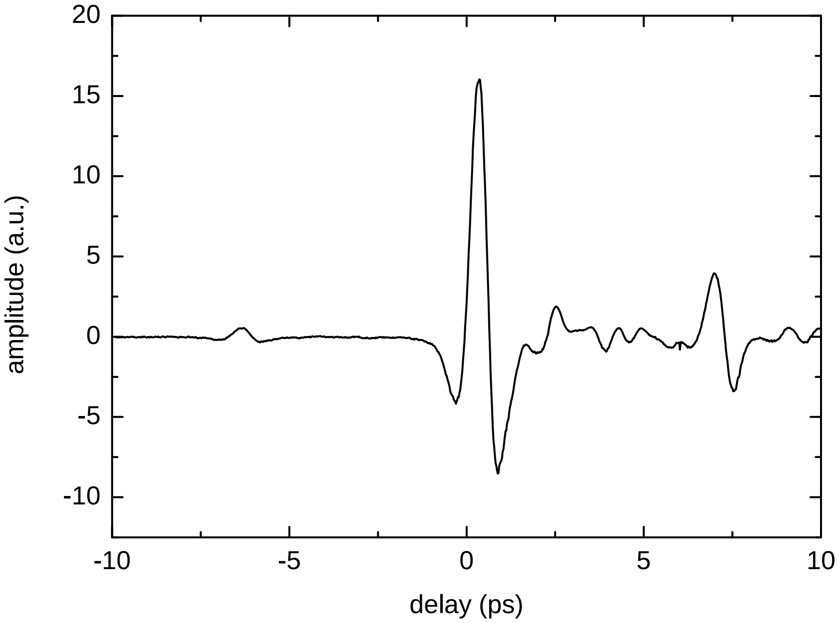

Figure 4.5: The electro-optic signal of the THz radiation reveals the near-single-cycle nature of the pulses.

From the measured peak height of the signal, one can calculate the electric field strength according to Eq. 2.58. The maximum balanced detection signal is $\Delta I_{max} = 1.8 \cdot I_p$ which corresponds to a field strength of 8.2 MV/m. Taking into account Fresnel reflection losses of the THz radiation at the entrance surface of the crystal of 28 %, the THz electric field becomes $E_{THz} = 11.4\,\mathrm{MV/m}$. This value is, however, known to underestimate the THz field strength for high fields, where an over-rotation of the electro-optic signal in ZnTe has been observed [56]. While for low fields the signal increases linearly with the field

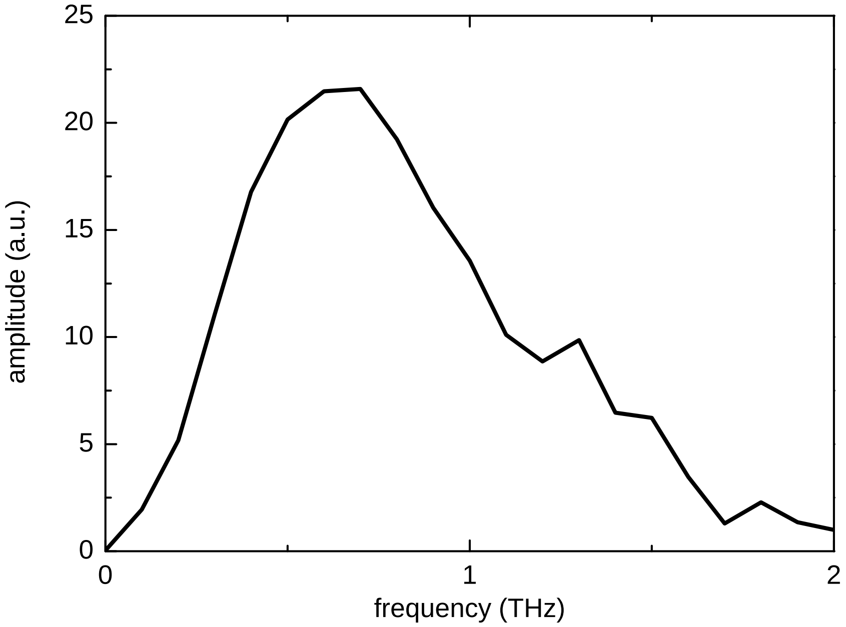

Figure 4.6: Spectrum of the THz radiation after a fast Fourier transform of the THz transient.

strength, it reaches a maximum for higher fields and decreases when the field strength is further increased.

The spectrum of the THz radiation shown in Fig. 4.6 is obtained from a fast Fourier transform (FFT) of the temporal amplitude (Fig. 4.5), where only the region from $-5\,\mathrm{ps}$ to $+5\,\mathrm{ps}$ was taken into account. It has to be noted that the response function for ZnTe is dependent on the frequency and the thickness of the crystal. However, for thin crystals and frequencies below 1.5 THz, it can be regarded as almost constant [68]. The spectrum exhibits a peak value at around 0.75 THz, while the average frequency is 0.9 THz. The additional small peaks appearing at higher frequencies of about 1.3 THz and 1.8 THz possibly correspond to harmonics of the THz fundamental frequency. Such peaks were also observed in [50] and with great distinction for shaped THz pulses [52]. In the latter case, partial reflections of the pump pulse were used to generate a sequence of pulses. Possibly, a similar effect occurs at one of the optical elements in the current system, thus accounting for the side peaks.

It has been mentioned in Sec. 4.1.2 that different frequency components of the THz beam have to be described separately when being focused. Explicitly, one expects a better focusability for higher frequency components. As a consequence, the spectral content should vary on the position along the transverse beam profile in the focus. In order to test this assumption, electro-optic sampling was performed for different lateral positions where the THz field has its maximum as well as where the field drops to 75 %, 50 % and 25 % of the maximum value. The corresponding spectra are shown in Fig. 4.7(a). In fact, when the spectral moments are evaluated (Fig. 4.7(b)), it is revealed that the

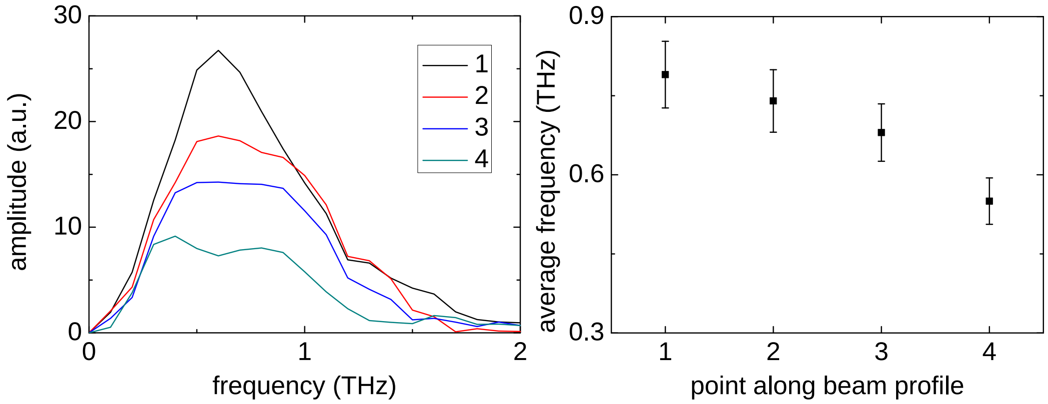

(a) (b)

Figure 4.7: (a) Recorded spectra for different positions along the transverse pump beam profile. 1 corresponds to the center of the beam with a maximum THz field strength. The probe beam has been shifted to the points 2, 3 and 4, where the electric field strength is 75 %, 50 % and 25 %, respectively. (b) The average frequency varies for different positions along the transverse beam profile.

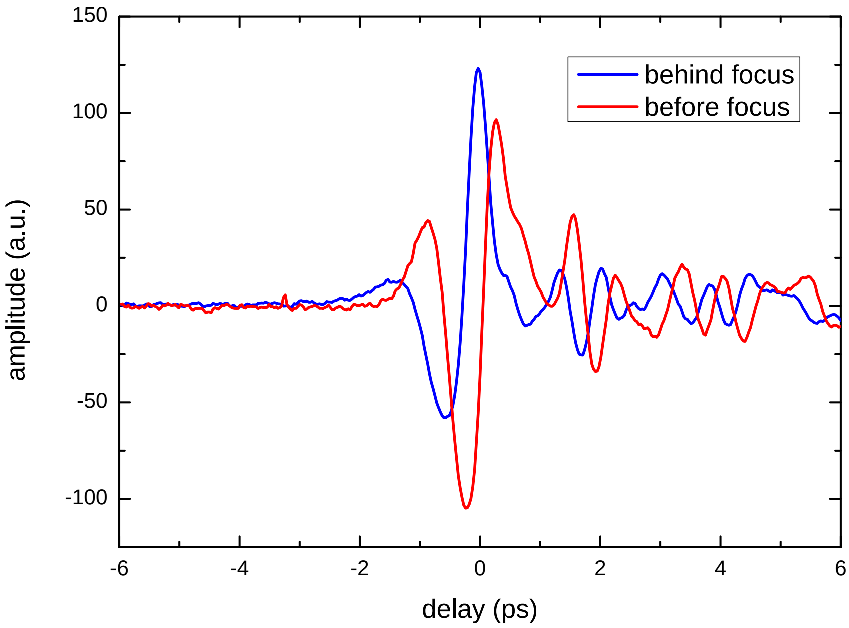

Figure 4.8: Two electric field transients measured before and after the focus which visualize the Gouy phase shift.

frequency decreases from the center to the edge of the beam.

Electro-optic sampling of a single-cycle THz pulse exhibits the ability to visualize the Gouy phase shift that a Gaussian beam experiences during its propagation through a focus. In [96], the Gouy shift was measured at a focal point in two different configurations, where the THz beam had either passed or not passed an additional focus before. In contrast, only one focus is considered here, and the electric field was measured at about 1 cm before and 1 cm behind the focus (Fig. 4.8). This distance corresponds approximately to the Rayleigh length. As a result of the Gouy phase shift, the sign of the strongest electric field direction is reversed after propagation through the focus. The phase shift between the two field transients is expected to be $\approx \pi/2$. Another consequence of the Gouy phase shift is an effectively increased local phase velocity in comparison to a plane wave. This effect can clearly be seen in Fig. 4.8, where the THz beam measured behind the focus appears at an earlier time with respect to the probe beam than it does before the focus.

4.3 Mapping of the THz field via the streaking technique

The streaking method may not only be exploited for the measurement of XUV pulse durations making use of a THz field. In turn, with the XUV pulses it is also possible to obtain temporal information about the THz pulses. This technique can thus be implemented as an alternative to electro-optic sampling. As an advantage, saturation effects which occur for electro-optical sampling, are not relevant for the streaking method. However, the electric field is not measured directly in this case, but obtained by a differentiation of the measured vector potential with respect to the time.

For the streaking experiment, the XUV beam has to be focused into a gas, and the generated electrons are accelerated or decelerated according to the strength and the sign of the actual THz field. Here, neon is used as the gas target due to several reasons. Its $2p$ line has a comparably large cross section for the interaction with photons at an energy of around 90 eV. In addition, the electrons are preferentially emitted in the direction of the XUV polarization [97] which is also the direction of observation. The $2p$ line exhibits a spin-orbit-interaction, but its splitting is only 0.1 eV [98] and can therefore be neglected. The ionization potential is 21.6 eV which means that for 90.7 eV photons, the kinetic energy of the electrons without THz field is 69.1 eV.

A delay scan of the THz pulse with respect to the XUV pulse is shown in Fig. 4.9. Photoelectron spectra were taken simultaneously with the two TOF spectrometers at different arrival times of the THz pulse. The pulses were delayed in steps of 30 fs and each spectrum was integrated over 10,000 shots. The measured curves exhibit similarities to the electric field measurements by electro-optic sampling in the sense that again the single-cycle nature of the pulse is revealed. It is clearly seen that when the left spectrometer detects electrons which are accelerated with respect to the initial energy, the right spectrometer detects decelerated electrons and vice versa. The maximum energy shift is almost the same in both detectors which means that neglecting the second term in Eq. 2.62 is still a good approximation.

The maximum vector potential was obtained after a re-optimization of the THz source and adjusting the NIR pulse duration for a maximum THz output. According to Fig. 4.10(a), a maximum shift of the photoelectron spectra of 20.6 eV was measured. The corresponding vector potential can be approximated as (cf. Eq. 2.63)

$$A_{max} = \frac{\Delta W}{e}\sqrt{\frac{m_e}{2W_0}} = 4.1 \cdot 10^{-6}\,\mathrm{Vs/m}. \tag{4.1}$$

The electric field of the THz pulse is inferred from a differentiation of the vector potential with respect to the time t and is depicted in Fig. 4.10(b). For the

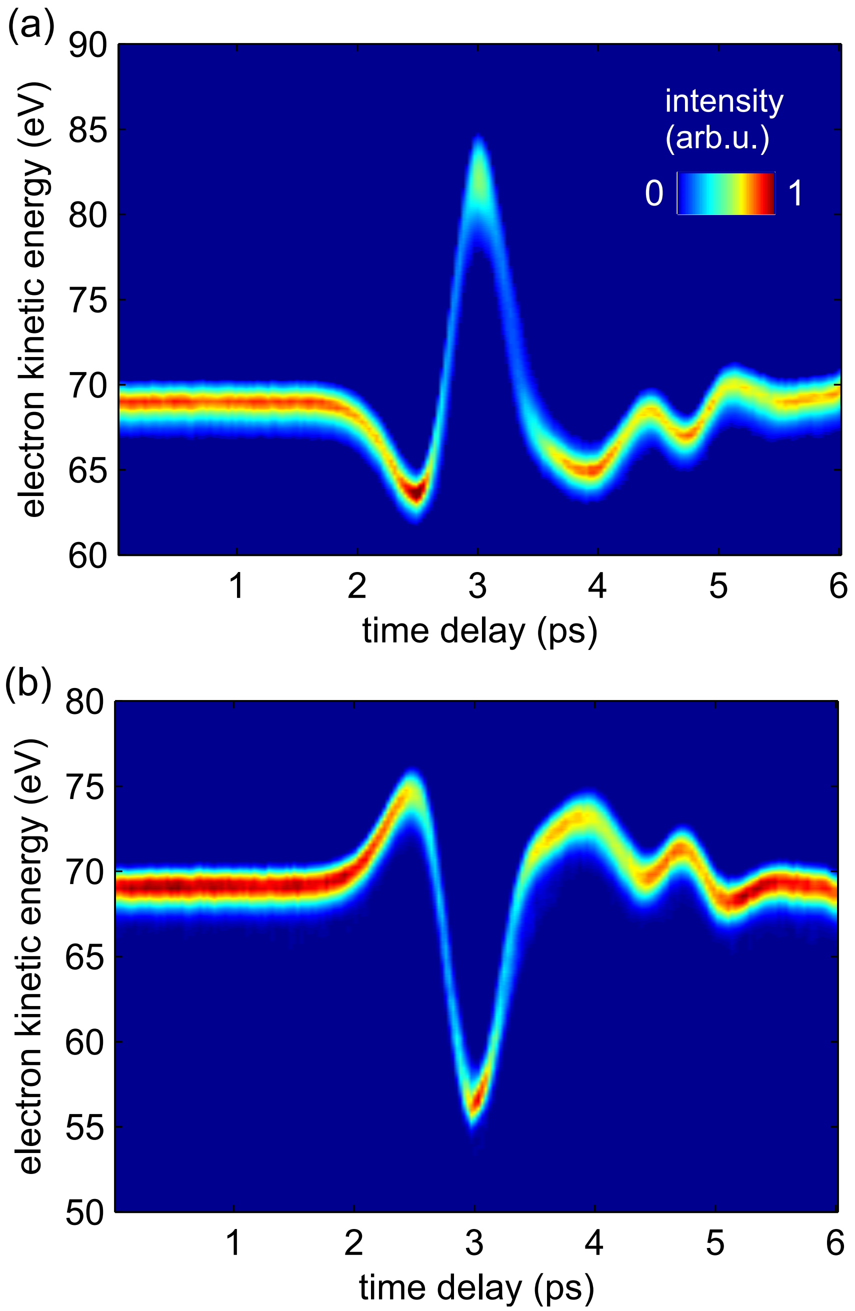

Figure 4.9: A series of neon $2p$ photoelectron spectra measured at different arrival times of the THz pulse with respect to the XUV pulse taken with the (a) left detector and (b) with the right detector.

calculation, the maxima of the spectra in Fig. 4.10(a) were used. Each point was averaged over five neighboring points to smooth the curve before differentiation. The resulting curve was then smoothed again over three neighboring points. As a result, the maximum value of the electric field is 22 MV/m. However, this value is possibly reduced by the smoothing process. It should also be noted that the electric field transient looks somewhat different from the field transient inferred from electro-optic sampling (Fig. 4.6). Here, the amplitudes in positive and negative directions are more similar than in the electro-optic sampling measurements. This can be explained by a different Gouy phase in both measurements. As was discussed in Sec. 4.2, the THz pulse form changes when propagating through the focus.

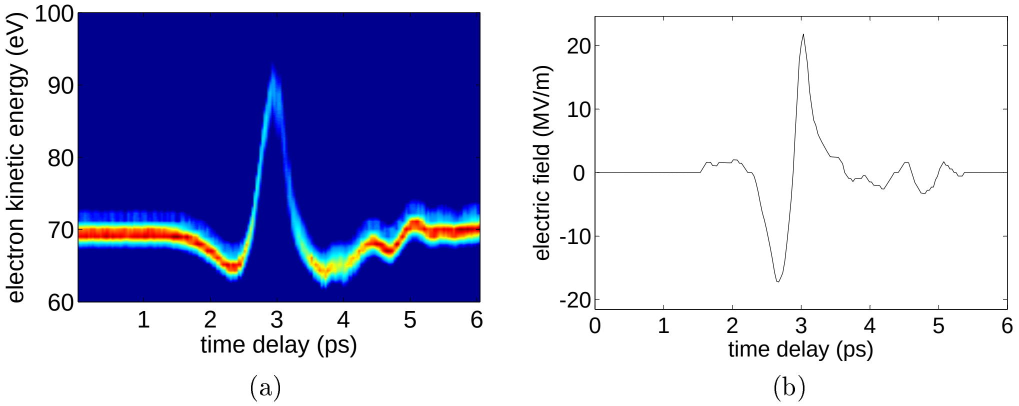

Figure 4.10: (a) Vector potential of the THz pulse after a re-optimization of the THz source. (b) Electric field after differentiation of the vector potential with respect to the time.

The spectrum of the THz pulse is inferred by a fast Fourier transform of the electric field transient and is shown in Fig. 4.11. It has a maximum amplitude of 0.83 THz and the spectral moment is 1.22 THz which is higher than what was measured by electro-optic sampling. The difference can be ascribed to a full re-optimization of the THz source and the THz imaging setup which was performed between the two measurements. Here, the interdependency of many different parameters plays a role. E.g. a varying THz frequency is explained by a variation of the tilt angle Θ of the pump pulse. Since the refractive index in $LiNbO_3$ depends on the frequency, the velocity matching condition (Eq. 2.32) changes for different values of Θ. This was also approved by experiments at 10 K where absorption effects within the crystal are negligible [51]. In the spectrum, side peaks are visible similar to the case of electro-optic sampling. Here, the peaks are even more pronounced which can be explained by the fact that the velocity-matching condition is better fulfilled in this spectral region due to the re-optimization process.

Knowing about the spectral properties of the THz radiation, the maximum electric field can be estimated from the value of the maximum vector potential

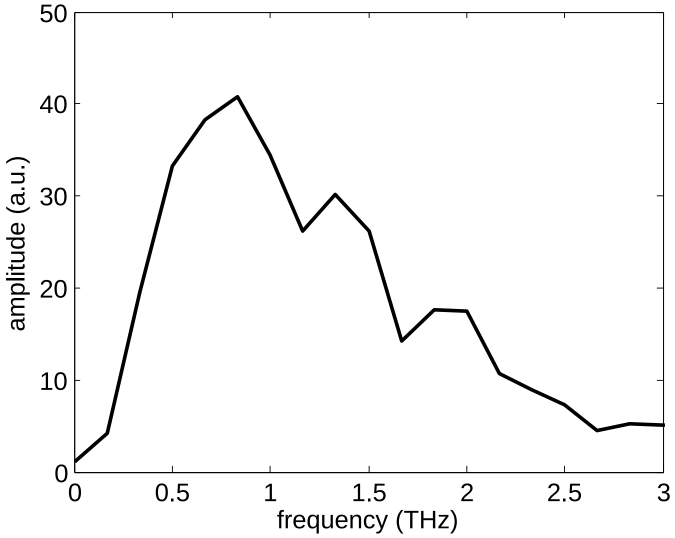

Figure 4.11: Spectrum of the THz pulse after a fast Fourier transform of the electric field.

by using the approximation $E_{max} \approx A_{max} \cdot \omega_{THz}$ which is valid for sinusoidal waveforms. Therefore, the resulting value of 32 MV/m only has a limited validity for the single-cycle THz waveform. The values for the electric field due to different measurement methods are compared in Table 4.1. It has already been noted that electro-optic sampling underestimates the field strength. In addition to the values obtained by the THz streaking experiment, the field is alternatively calculated according to

$$E_{max} = \sqrt{\frac{2I_{max}}{c\epsilon_0}}, \tag{4.2}$$

where ϵ_0 is the electric field constant. The maximum intensity is $I_{max} = W/tA$, with the pulse energy $W = 1.7\,\mu\mathrm{J}$, the time width of about $t = 1\,\mathrm{ps}$ and a focus area A of $1.5\,\mathrm{mm}^2$. This results in a value of $I_{max} = 113\,\mathrm{MW/cm}^2$ for the maximum intensity. According to Table 4.1, the calculated value of the electric field lies just between the values obtained by the streaking experiment. It can be concluded that the electric field has a value of well above 20 MV/m. This is distinctly higher than what was reported in [52] and comparable to [20], although a pump pulse energy lower by a factor of 2 or 8 was applied, respectively. The enhancement of the field can partly be explained by a higher THz generation efficiency and a lower absorption which was achieved in this work (cf. Sec. 4.1.1). In addition, by using a teflon lens instead of a parabolic mirror for the recollimation of the THz beam, the distance to the crystal can

Measurement technique	E_{max} (MV/m)
Electro-optic sampling	11
Streaking (from electric field)	22
Streaking (approximation)	32
Energy, pulse duration and focus size	29

Table 4.1: THz electric field values from different measurement methods

be adjusted in a more flexible way. Thus, a focus area of 1.5 mm^2 is achieved which is smaller than the value of 2 mm^2 reported in [52].

The measurement of the time-dependent vector potential also contains information concerning two other parameters which are important for the streaking measurements. The first one is the ponderomotive potential which results in a maximum value of $U_p = 0.44\,\text{eV}$. The other one is the streaking speed $s = \partial(\delta W)/\partial t$ which corresponds to the slope in Fig. 4.10(a). It has a maximum value of $s = 0.15\,\text{eV/fs}$ which is reached at about 100 fs after the maximum of the energy shift. For typical time duration measurements it is lower though and will be evaluated for each measurement.

Measurement with bandpass filter

In the streaking curves, an expected behavior was observed at certain time delays between THz and HHG pulses. In these regions, the broadening of the photoelectron spectrum was large, albeit the streaking speed was low. This broadening can e.g. be seen in Fig. 4.10(a) at a time delay of about 3.9 ps. The same behavior was observed with the THz-field-driven streak camera at FLASH when no bandpass filter was used [16]. The reason for this is not yet clear, but fluctuations of higher frequency components might play a role. To test the behavior for the laser-based THz source, a bandpass filter was inserted into the THz beam path which has a central transmission wavelength of 307 μm and a FWHM bandwidth of 20 μm. Mapping of the THz vector potential with bandpass filter is shown in Fig. 4.12 The THz pulse now consists of several cycles with decreasing amplitudes which is explained by the decreased bandwidth of the THz pulse. Since the THz intensity is reduced, the streaking amplitude is much lower than in the previous measurements. The measured curve looks smoother than without bandpass filter. However, it is not clear whether this is caused by the lower amplitude or by the lower bandwidth. Currently, the obtained streaking speeds with bandpass filter are too low for an accurate XUV pulse duration measurement. When the energy output of the THz source can be further increased in the future, the use of a bandpass filter might be advantageous to reduce unwanted fluctuations.

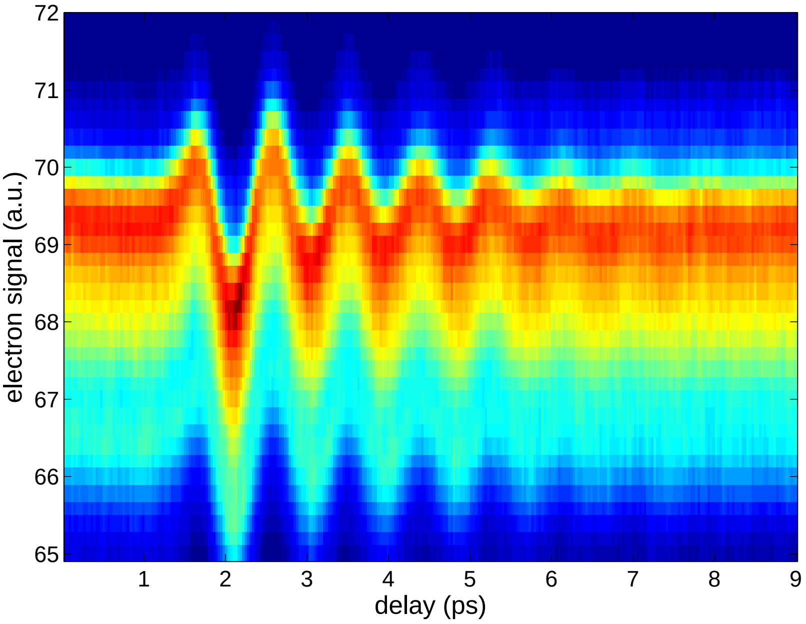

Figure 4.12: Streaking curve measured with bandpass filter

Chapter 5

Results on ultrafast temporal measurements with THz streaking

In this Chapter, the results of ultrafast temporal measurements utilizing the laser-based terahertz-field-driven streak camera are presented. In Sec. 5.1, the Gouy phase shift is considered which is an important effect when reconstructing HHG pulse parameters. It follows the evaluation of the harmonic pulse duration and its linear chirp rate in Sec. 5.2. In addition, the control of the harmonic chirp is demonstrated by changing the chirp of the fundamental laser. The streaking of Auger lines involving an unexpected behavior is investigated in Sec. 5.3. Finally, the application of the presented method for the pulse duration measurement at free electron lasers is discussed in Sec. 5.4.

5.1 Influence of the Gouy phase shift

During propagation through the interaction zone, the phase of the THz pulse changes with respect to the phase of the XUV pulse. This behavior is referred to as Gouy phase shift (cf. App. A). As a consequence, the streaked photoelectron spectra show a broadening in addition to what is expected from the XUV pulse duration. Even for an XUV pulse with an infinitesimal duration, the electrons created at different points within the interaction zone see different phases of the THz field. Therefore, it is important to estimate the value of the phase shift in the interaction zone. This can be carried out in different ways. In [16], the interaction length was estimated from the distance between gas capillary and XUV beam by assuming a certain density distribution of the gas. In combination with a simulation of the Rayleigh length of the focused THz beam, the phase shift within the interaction zone was evaluated. The contribution to the spectral broadening due to the Gouy phase shift could

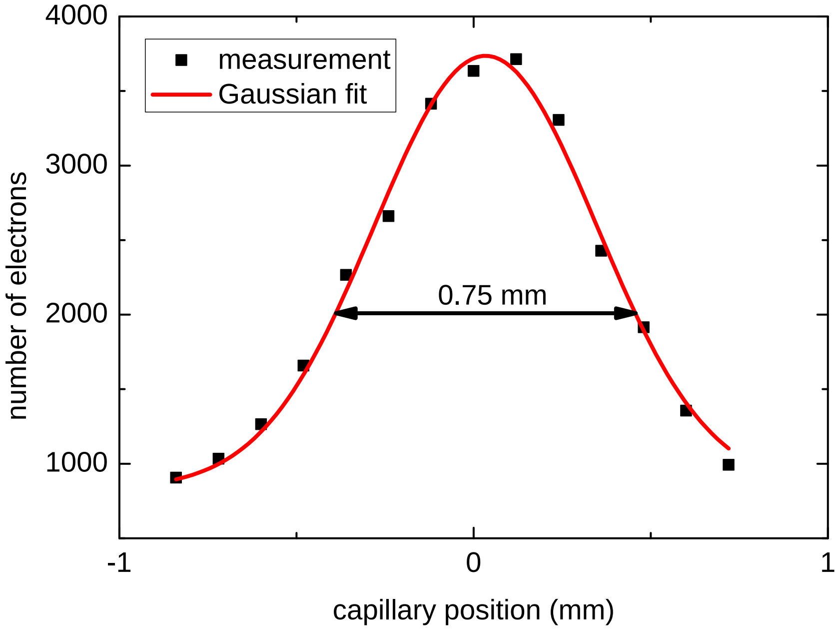

Figure 5.1: Scan of the gas beam in transverse direction recording the number of electrons at each spatial position.

thus be calculated. In this work, the interaction zone length was directly measured by determining the number of electrons while shifting the gas capillary in transverse direction. According to the Gaussian fit in Fig. 5.1, the FWHM of the gas density distribution is 0.75 mm.

In a second step, the phase shift within the 0.75 mm long interaction zone is estimated. The Rayleigh length was determined in Sec. 4.1.2 as $z_R = 9.8\,\mathrm{mm}$ which corresponds to a phase shift of $\phi(z) = \arctan(z/z_R) = 4.4°$. In the streaking experiment, the time shift Δt can then be calculated according to

$$\Delta t = \frac{\Delta\phi}{360°}T. \tag{5.1}$$

The result is $\Delta t = 12.2\,\mathrm{fs}$ taking into account an oscillation period of 1 ps. The definition of a period time, however, is not straightforward for the single-cycle pulse emitted by the THz source. A different approach involves the direct measurement of the temporal shift. In this case, the fact that the Gouy phase shift is accompanied by a temporal shift is exploited. In Fig. 4.8, the THz electric field was measured by electro-optic sampling at a distance of about z_R before and behind the focus. The temporal shift between both curves estimated at the first minimum of the electric field is 330 fs. It has to be taken into account that the phase does not vary linearly within the Rayleigh range. Instead, the maximum slope at $z = 0$ is a factor of 1.27 higher than the average slope in the boundaries between $-z_R$ and $+z_R$. Thus, the resulting value for the time shift is calculated as $\Delta t = 330\,\mathrm{fs} \cdot 0.75\,\mathrm{mm}/20\,\mathrm{mm} \cdot 1.27 = 15.7\,\mathrm{fs}$. This value is slightly higher than the first one. It will be used for further calculations, because less assumptions are needed for its determination. The spectral broadening of the photoelectron spectra in the streaking experiment thus represents a convolution of contributions due to the XUV pulse duration and the longitudinal Gouy phase shift. In contrast, the lateral Gouy phase shift can be neglected, since the XUV focus size is much smaller than the THz focus size. Therefore, the THz phase in lateral direction can be regarded as constant within the interaction zone.

For the future, it is desirable to reduce the influence of the Gouy phase. This can be achieved by a novel focusing geometry of the THz radiation. Therefore, a setup was tested during this thesis which consists of a cylindrical lens with $f = 180\,\mathrm{mm}$ and a cylindrical mirror with $f = 60\,\mathrm{mm}$ instead of the parabolic mirror with $f = 100\,\mathrm{mm}$. The cylindrical lens is used to focus the beam in horizontal direction and the cylindrical mirror for the focusing in vertical direction. This constellation aims for two effects. On the one hand, the Rayleigh length should be increased due to the looser focusing in the direction of the polarization. On the other hand, the tighter focusing in vertical direction should allow for a smaller distance between gas nozzle and the center of the THz beam which in this case has an elliptical shape in the focus. Thus, the interaction length between gas and XUV beam can be decreased. Since the Gouy phase is small for a small ratio between interaction length and Rayleigh length, both effects are expected to decrease the influence of the Gouy phase shift on the streaking measurements. However, the test of this setup resulted in a decreased THz electric field which was not sufficient for the determination of the shortest HHG pulse lengths. It is worthwhile though to optimize this setup in the future and thereby increase the measurement accuracy of small time durations.

5.2 Evaluation of HHG pulse parameters

For the characterization of the HHG pulse duration and its linear chirp rate, the time delay between XUV and THz pulses was adjusted to a value of 2.8 ps, where according to Fig. 4.9 the slope of the vector potential has a maximum. For the first measurements, the pulse duration of the NIR laser was increased to a value of 45 fs. This was achieved by reducing the bandwidth to about 40 nm in order to maintain a chirp-free fundamental laser pulse. In this configuration, field-free and streaked photoelectron spectra were taken by the two TOFs. According to Fig. 5.2(a),(b), the unstreaked photoelectron spectra measured with the two detectors have one peak at about 69 eV which corresponds to the 59^{th} harmonic shifted by the binding energy of the neon $2p$ line. The smaller peak at 66 eV is attributed to the 57^{th} harmonic from which a small fraction is reflected by the molybdenum-silicon multilayer mirrors. For each spectrum, the peaks were fitted by Gaussians assuming the same width for the different peaks. The resulting FWHM of the 59^{th} harmonic was 0.87 eV and 0.88 eV for the left and the right detector, respectively. When switching on the THz field, the corresponding photoelectron spectra are broadened (Fig. 5.2(c),(d)). In order to determine the widths of the streaked photoelectron spectra generated by the 59^{th} harmonic, the Gaussian fits from before were used keeping the relative amplitudes and spectral distances of the peaks constant. The absolute amplitude and spectral positions as well as a common spectral width of the peaks were set as free parameters. As a result, the FWHM at the left and the right detector are 2.35 eV and 2.45 eV, respectively. From these values the broadening induced by streaking is inferred by a deconvolution according to Eq. 2.72, yielding 2.18 eV and 2.29 eV for the left and right TOF, respectively. Assuming Gaussian pulses and taking into account the measured streaking speed of (54 ± 2) meV/fs, the temporal width is calculated to be $\tau_X = 41$ fs. According to the previous section, this value represents a convolution of the actual HHG pulse duration with a contribution due to the Gouy phase shift which was estimated to be $\tau_G = (16 \pm 2)$ fs. The corrected pulse duration for the 59^{th} harmonic is thus

$$\tau_{X,corr} = \sqrt{\tau_X^2 - \tau_G^2} = (38 \pm 4)\,\mathrm{fs}. \tag{5.2}$$

The HHG pulse duration is smaller than the pulse duration of the fundamental laser which is in agreement with most of the other pulse duration measurements that were performed for harmonic radiation. The ratio of pulse durations of 0.84, however, is larger than what was observed in [41, 11, 12, 13]. An explanation for the comparably long harmonic pulse durations is found when considering the experimentally obtained nonlinearities of the harmonic generation process which were reported in [40]. There, the harmonic output energy versus the fundamental intensity was recorded for different harmonic

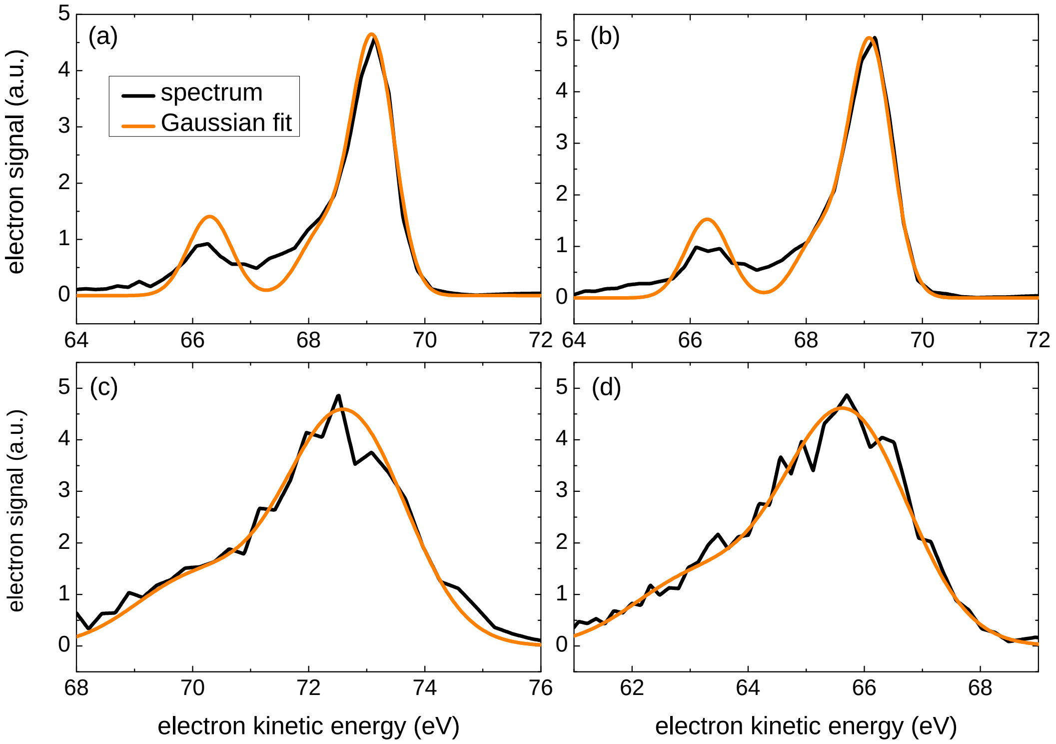

Figure 5.2: Field-free photoelectron spectra taken by the (a) left and the (b) right detector showing mainly the 59^{th} harmonic order. (c),(d) The corresponding streaked spectra show a clear broadening induced by the XUV pulse.

orders. For the 59^{th} harmonic it was observed that the order of nonlinearity is close to one in the plateau region. This means that in the low ionization regime, the initial fundamental pulse shape is transferred to the harmonics with only small changes. Therefore, similar pulse durations of the fundamental and harmonic beams are expected. In contrary, the order of nonlinearity is larger for the 9^{th} harmonic to the 27^{th} harmonic. This explains the shorter pulse durations measured in the experiments mentioned above when compared to the corresponding fundamental pulse durations.

The different widths of the THz-field-induced broadening measured for the left and the right detectors in Fig. 5.2 are a signature of a linear chirp. The chirp rate is calculated according to Eq. 2.74:

$$c = \frac{\sigma_l^2 - \sigma_r^2}{8 s \tau_X^2} = -(1^{+2}_{-1})\,\mathrm{meV/fs}. \tag{5.3}$$

In harmonic generation, a negative chirp is predicted due to the atomic dipole phase. It has its origin in the additional phase that the electron gains in the excursion time during the HHG process. Thus, the current result is in accordance with this expectation. A negative linear chirp of the harmonics was also observed in [42, 13].

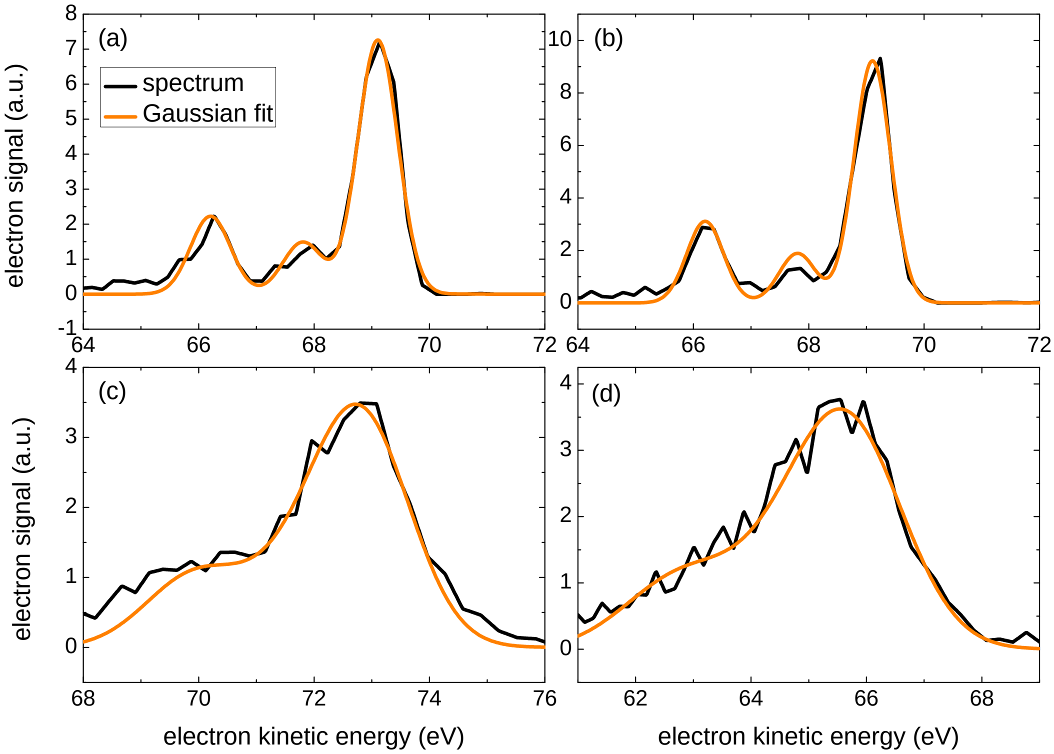

Figure 5.3: Same as Fig. 5.2, but a negative chirp is applied to the fundamental laser. This results in different values for the broadening at the two detectors corresponding to a negative chirp.

In a next step, a negative chirp was applied to the fundamental laser such that its pulse duration was elongated to 60 fs. The corresponding unstreaked photoelectron spectra in Fig. 5.3(a),(b) show an additional peak in between the 57^{th} and the 59^{th} harmonic order. This is attributed to the formation of a sideband which is generated due to the interaction of the neon gas with the harmonics and the fraction of the fundamental beam transmitted by the zirconium filter. Sidebands appear at an energy which is shifted by $\pm n\hbar\omega_0$ with respect to the harmonic energy, where n is an integer number. The reason, however, why no sideband is observed at the higher-energy side of the 59^{th} harmonic remains unclear. The assumption of the sideband formation was tested by removing the zirconium filter that blocks the fundamental beam. In this case, the intensity of the sidebands was clearly increased to comparable heights as the photoelectron peak. In addition, sidebands on both sides of the photoline occur. Also in Fig. 5.2 an additional peak between the 57^{th} and the 59^{th} harmonic is fitted to account for the appearance of a sideband which in this case was not resolved.

In the streaked spectra in Fig. 5.3(c),(d), a clear difference is observed for the two detectors. The widths in the field-free case are 0.82 eV and 0.75 eV. The difference of the widths is most likely explained by different alignments

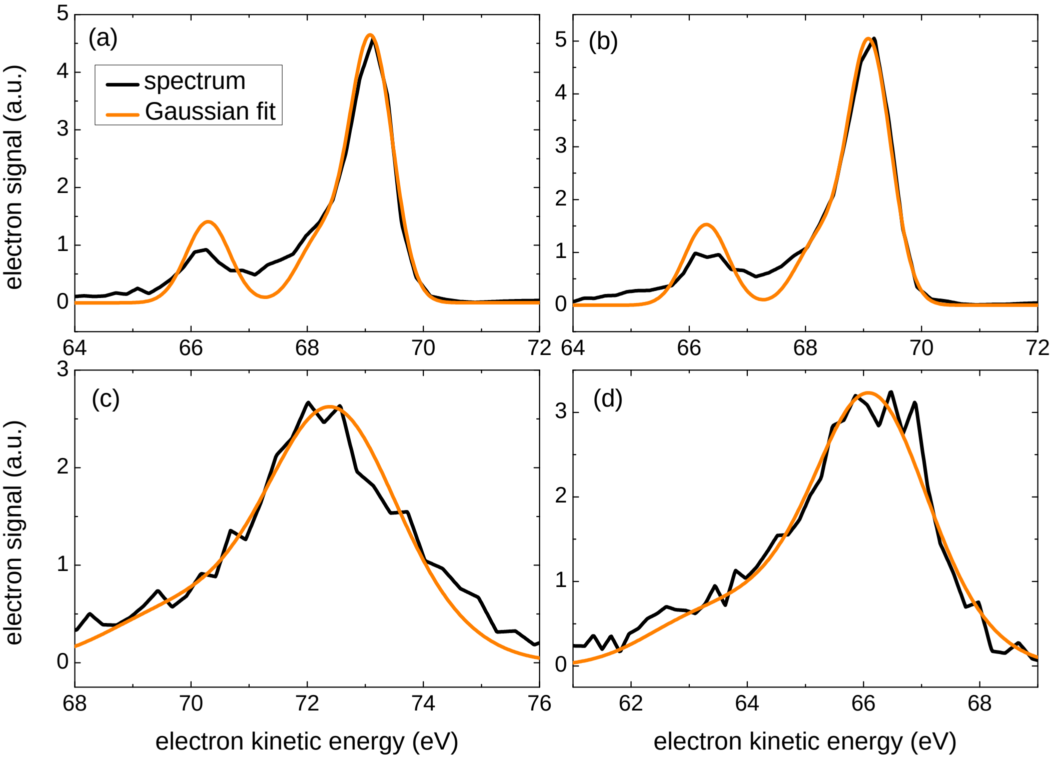

Figure 5.4: Same as Fig. 5.2, but a positive chirp is applied to the fundamental laser which is transferred to the 59^{th} harmonic.

of both TOFs which might slightly change the resolution. After switching on the THz field, the widths are 1.97 eV and 2.31 eV for the left and right TOF, respectively. The HHG pulse duration is calculated as $\tau_{X,corr} = (44 \pm 4)$ fs which already takes into account the deconvolution of the Gouy phase shift. The streaking speed in this case was measured to be $s = (43 \pm 2)$ meV/fs. Evaluating the linear chirp rate results in a value of $c = -(2^{+2}_{-1})$ meV/fs. This increased linear chirp can be explained as follows. Since the harmonic photon energy is a multiple of the fundamental photon energy, a time-varying energy of the fundamental will be transferred to a time-varying energy of the harmonic, i.e. a chirp. Detailed experimental proof of this effect is also given in [42].

The chirp of the 59^{th} harmonic changes its sign, when a positive chirp is applied to the fundamental laser. This can be seen from Fig. 5.4(c),(d), where the measured spectrum at the left detector is broader than at the right detector. The widths of the streaked spectra are 2.40 eV and 2.11 eV, while for the field-free case they are 0.85 eV and 0.78 eV for the left and right TOF, respectively. Deconvolution results in a broadening due to streaking which is 2.24 eV and 1.96 eV. With the measured streaking speed of (43 ± 2) meV/fs and after accounting for the broadening induced by the Gouy phase shift, the pulse duration of the harmonic is $\tau_{X,corr} = (46 \pm 4)$ fs. The corresponding linear chirp rate is positive and has a value of $c = +(2^{+2}_{-1})$ meV/fs. Contributions to the measuring errors of the HHG pulse duration and its linear chirp are given by uncertainties in the determination of the spectral widths, the streaking speeds and the Gouy phase shift.

After introducing a chirp to the fundamental laser, its pulse duration was about 60 fs. It has to be noted that the fundamental pulse measured with the SPIDER did not show a Gaussian temporal envelope after introducing a chirp. Instead, a structure of the pulse with more than one peak was observed. In addition, this structure was not stable in time which leads to an increased uncertainty for the measured fundamental pulse duration in the case of a chirped laser pulse. Therefore, a comparison of fundamental pulse duration and HHG pulse duration is difficult in this case.

In a next step, the laser pulse duration was reduced to 25 fs. As is obvious from Fig. 5.5, the streaking-induced broadening is less pronounced. This is mainly caused by a shorter harmonic pulse duration. The widths in the field-free case are 1.08 eV for both TOFs; switching on the THz field increases the widths to 1.63 eV and 1.75 eV measured with the left and right detector, respectively. Deconvolution and taking into account the Gouy phase yields an XUV pulse duration of $\tau_{X,corr} = 22^{+4}_{-6}$ fs. Here, the relative uncertainty is increased and has an asymmetric behavior. This is because the Gouy phase has an increasing influence on the measured results for shorter pulse durations. It is therefore desirable in the future to decrease the spectral broadening which comes from the Gouy phase shift. The ratio in pulse durations of harmonic and fundamental pulses is 0.88 and thus similar to the previous case. The linear chirp rate for an unchirped fundamental pulse is $c = -(2 \pm 2)$ meV/fs. It is increased to $c = -(4 \pm 2)$ meV/fs when a negative chirp is applied to the fundamental laser pulse (Fig. 5.5(e),(f)). This larger value when compared to the longer pulses is understood in the following: the shorter pulses are accompanied by a larger spectral width in the Fourier-limited case. In addition, this larger spectral content is in the chirped case varied faster due to the shorter pulse duration.

THz field fluctuations

In order to determine the fluctuations of the THz field, a single-shot measurement is required. While the laser-based THz-field-driven streak camera has a single-shot capability for higher XUV pulse energies, the single-shot mode could not be achieved with the harmonics used in this work, where averaged measurements over many pulses were performed. Instead, the technique of electro-optic sampling was utilized for the evaluation of shot-to-shot fluctuations. The resulting FWHM of the distribution of single-shot electric field strengths was 3 % when the NIR pulse was overlapped with the maximum electric field strength. This corresponds to the maximum slope of the vec-

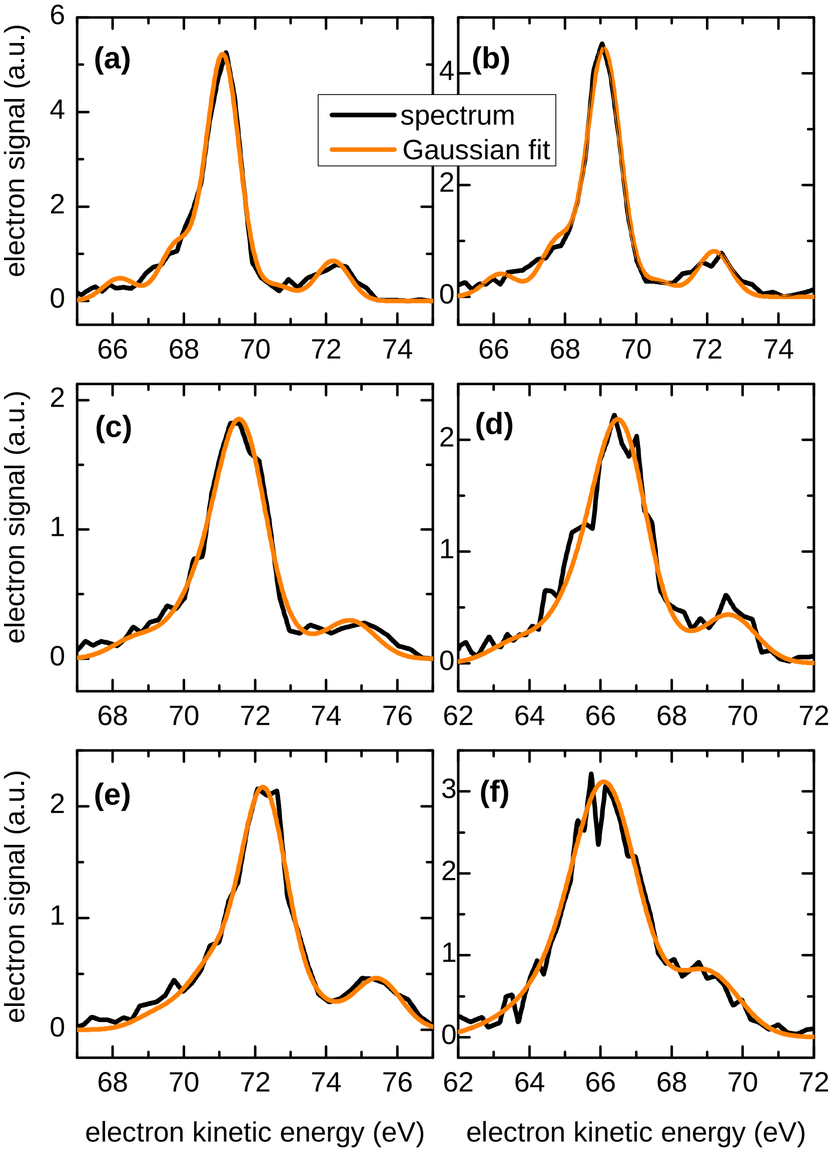

Figure 5.5: (a),(b) Field-free and (c),(d) streaked spectra for a fundamental pulse duration of 25 fs taken with the left and right detector, respectively. (e),(f) Streaked spectra for a negatively chirped fundamental pulse (from [99]).

tor potential, where the XUV pulse duration measurements were performed. A variation of the electric field strength is equivalent to a variation of the slope s of the vector potential and was therefore accounted for by an increased uncertainty of the slope parameter. Note that the measured fluctuations are different from the fluctuations of the THz pulse energies measured in Sec. 4.1.1. Here, one has to take into account that the electric field is proportional to the square root of the energy and that the fluctuations may be different at different phases.

For a comparison, the field fluctuations were also measured at the zero-crossing of the electric field which resulted in a value of 7 %. Because of these varying fluctuations, the determination of HHG pulse parameters was restricted to a single phase. In general, fluctuations play a more important role in THz streaking when compared to NIR streaking. In the first case, the maximum energy shift due to streaking is much larger than the spectral width, while in attosecond streaking both values are comparable. Thus, in the femtosecond range the same relative field fluctuations have a stronger influence on the measured width. After a possible reduction of the fluctuations in the future, one can take into account different phases and make use of an appropriate reconstruction algorithm known as FROG-CRAB [100, 101].

Temporal resolution

An important parameter of the laser-based terahertz-field-driven streak camera is its temporal resolution. It can be calculated according to Eq. 2.65:

$$\tau_{res} \approx \frac{\sigma_{unstreaked}}{s} = \frac{1\,\text{eV}}{0.1\,\text{eV/fs}} = 10\,\text{fs}. \tag{5.4}$$

Here it was assumed that the streaking-induced broadening should be at least 1 eV which corresponds approximately to the widths of the field-free spectra. For the streaking speed, a value of 0.1 eV/fs was supposed which was obtained when the fundamental laser parameters such as pulse duration and spectral momentum were optimized for a high THz energy output. Reducing the laser pulse duration to generate short harmonic pulses typically reduces the streaking speed. Therefore, the time resolution is deteriorated in the current setup, where the same laser pulse is used for HHG and THz generation. For the minimum pulse durations of 20 fs obtained with the laser system, however, the obtained THz field strengths are still sufficiently high.

The temporal resolution of the streak camera can still be improved by an enhancement of the streaking speed. Since the THz source is scalable, a higher THz output energy is achieved by using laser pulses with a higher energy. However, this does not automatically translate into higher THz intensities. As the pump spot size has to be increased in order to prevent saturation effects, the average THz propagation distance within the crystal is increased and thereby absorption mainly of the higher-frequency components. This effect resulted in the observation of lower THz frequencies when pump pulse energies of a few tens of mJ were used [20, 50]. However, the minimum focus size is larger for a beam containing longer wavelength components. In addition, the longer THz oscillation period of the single-cycle pulse decreases the achievable intensity. There are two ways to circumvent the increased absorption. The first one is the elliptical pump spot used in this work which decreases the THz propagation distance within the crystal. On the other hand, one can also reduce the absorption coefficient by cooling the crystal down to temperatures below 200 K. This scheme is already planned for a further development of the setup where the crystal will be cooled to the temperature of liquid nitrogen. While this has shown to efficiently decrease the absorption at low pump energies [51], the setup still has to be tested at high pump energies which also leads to an increased energy absorption within the crystal. Given the possibilities of increasing the pump energy and decreasing the absorption, a time resolution of a few fs is feasible.

5.3 Post-collision interaction of streaked Auger electrons

The streaking results found in the previous section were obtained from electrons formed by direct photoemission of neon atoms. However, it is also possible to streak Auger electrons which can be emitted in addition to an inner-shell photoelectron (cf. Sec.2.1). Here, the width of the spectrum is determined by the lifetime of the inner-shell vacancy and the resolution of the detector. In this way, it is possible to improve the temporal resolution of the THz-field-driven streak camera which is directly proportional to the measured field-free spectral width. As a short-cut, however, Auger streaking does not allow for a determination of the XUV chirp, since it is in general not sensitive to the XUV photon energy and the corresponding temporal changes in energy, i.e. the chirp.

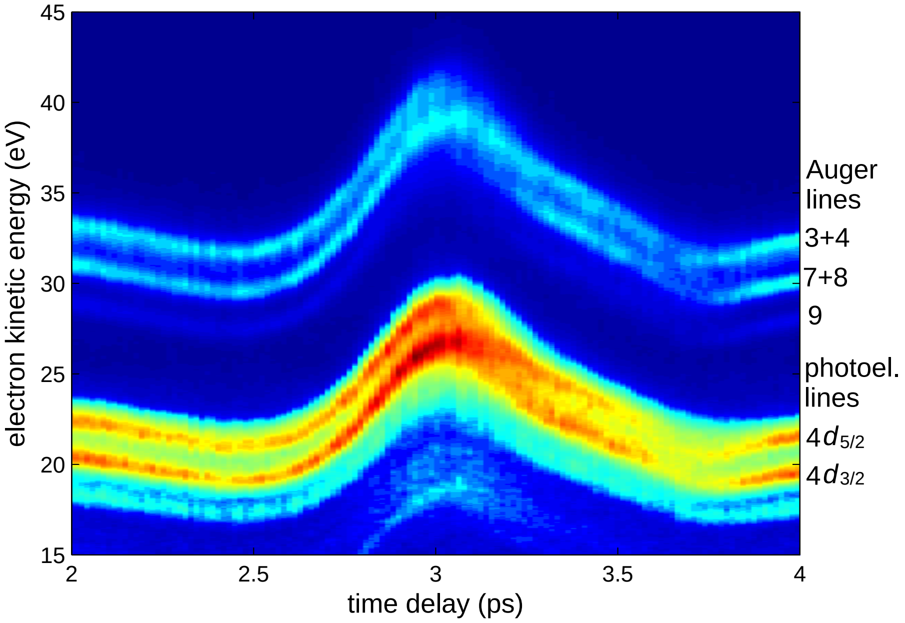

Figure 5.6: Streaking curve of xenon measured with the left TOF showing the $4d$ photoelectron lines and the corresponding Auger lines. For the identification of the Auger lines see Table 5.1.

For the investigation of Auger streaking, xenon was used as gas target in the interaction zone. Fig. 5.6 displays $4d$ and Auger electron spectra at different time delays between the THz and XUV pulses. 3 Auger lines are visible which have energies of about 30 eV, 32 eV and 34 eV in the unstreaked case. The streaking curve exhibits similar features when compared to the neon photoelectron streaking curves. However, the maximum energy shift is reduced which is due the lower initial kinetic energy (cf. Eq. 2.63). For the determination of the streak-induced broadening, field-free and streaked Auger spectra were taken with both TOF detectors (Fig. 5.7). The time delay was set to a value of 2.8 ps which corresponds to a zero-crossing of the THz vector potential. The first graph shows the xenon Auger spectrum without THz field. It consists of nine single lines whose spectral positions and relative amplitudes are given in Table 5.1. Due to the limited spectral resolution of the TOF spectrometers of about 0.55 eV, the lines 3 + 4, 5 + 6, and 7 + 8 each appear as single peaks in the spectrum.

When a THz field is applied, a clear difference in the spectra is visible between the data taken at the ascending slope and at the descending slope of the energy shift derivative with respect to time. Here, the first spectrum is measured with the left TOF and the second spectrum is measured with the right TOF. It turns out that the spectral width at the descending slope is larger than at the ascending slope. While for a photoelectron line this behavior could be attributed to a negative chirp of the XUV pulse, for Auger lines this is a highly unexpected behavior. As discussed before, an XUV chirp will not be visible in the streaked Auger spectra. In collaboration with the theoretical physicists Sebastian Bauch and Prof. Dr. Michael Bonitz from the University of Kiel, a different explanation for this linewidth asymmetry could be found which will be presented in the following. The current results are a confirmation of the same qualitative behavior observed with the THz-field-driven streak camera at FLASH [102]. The results presented here will be part of a publication which comprehends also the calculations and the FLASH data [103].

number	interpretation	spectral position	relative intensity
1	$N_4O_{2,3}O_{2,3}: {}^3P_0$	36.20 eV	15
2	$N_4O_{2,3}O_{2,3}: {}^3P_2$	34.99 eV	43
3	$N_5O_{2,3}O_{2,3}: {}^3P_0$	34.21 eV	86
4	$N_4O_{2,3}O_{2,3}: {}^1D_2$	34.07 eV	104
5	$N_5O_{2,3}O_{2,3}: {}^3P_2$	33.21 eV	48
6	$N_5O_{2,3}O_{2,3}: {}^3P_1$	32.99 eV	39
7	$N_5O_{2,3}O_{2,3}: {}^1D_2$	32.09 eV	97
8	$N_4O_{2,3}O_{2,3}: {}^1S_0$	31.71 eV	100
9	$N_5O_{2,3}O_{2,3}: {}^1S_0$	29.73 eV	73

Table 5.1: Spectral positions, relative intensities and the interpretation of xenon Auger lines. The data and nomenclature of the lines are taken from [104].

It was found that even though the influence of the Coulomb ionic potential on the emitted electrons can introduce a linewidth asymmetry [106], this effect is too small to explain the measured difference in widths. Instead, the effect

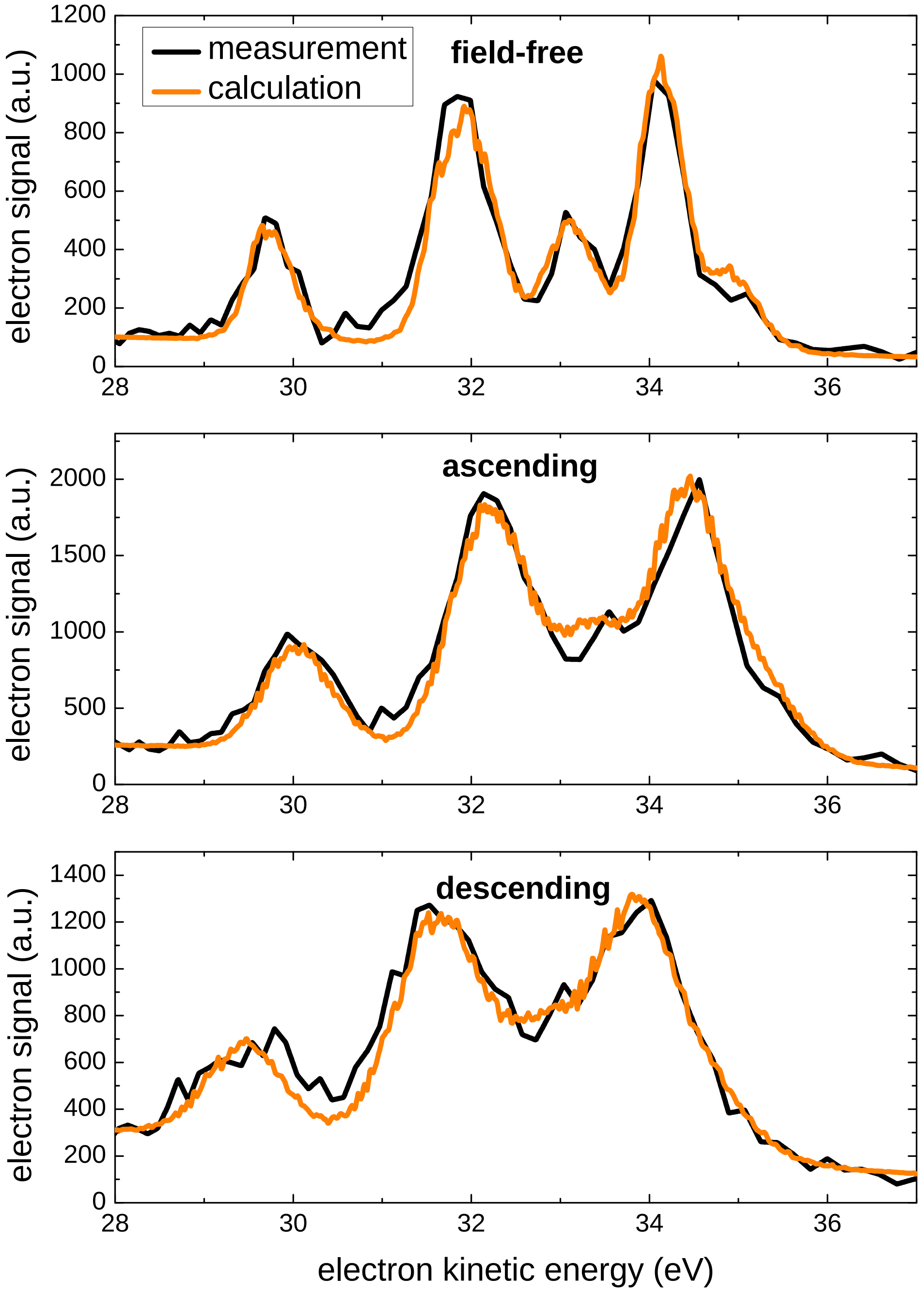

Figure 5.7: Xenon Auger spectra measured without THz field and at the zero-crossing of the energy shift. The spectra at the ascending and descending slopes are taken with the two detectors located in opposite directions. The calculations were carried out by Sebastian Bauch [105].

of post-collision interaction (PCI) [107, 108] was carefully investigated which is known to introduce linewidth distortions under certain circumstances. PCI describes the interaction of the photoelectron responsible for the inner-shell vacancy, the emitted Auger electron and the ion in the continuum. The Auger electron is typically emitted a few fs after the photoelectron according to the decay time of the inner-shell vacancy. When the kinetic energy of the Auger electron is higher than that of the photoelectron, it will overtake the latter at some time. This process is accompanied by a transfer of energy between both electrons which can be understood in the sense that the ionic charge affecting the electrons is changed. After the process of overtaking, the photoelectron shields a part of the ionic charge that attracts the Auger electron. As can be seen from Fig. 5.8, this is accompanied by a shift from the doubly charged ionic potential curve to the singly charged ionic potential curve which lies higher in energy. The magnitude of this energy shift now depends on the distance to the nucleus where the process of overtaking takes place. It was demonstrated that for slow photoelectrons with energies of around 1 eV, PCI leads to a broadening and asymmetric behavior of the Auger spectrum [109]. This is because the Auger electrons emitted only a short time after the corresponding photoelectron, experience a large energy shift, whereas the Auger electrons emitted at later times are basically undisturbed. However, when a photon energy of 89.5 eV was used for the ionization of xenon, the measured Auger spectrum was not cognizably changed compared to the case without PCI effect. This is close to the photon energy that was used for the measured xenon Auger spectra in this work and demonstrates that the measured linewidth asymmetry cannot be explained by PCI alone.

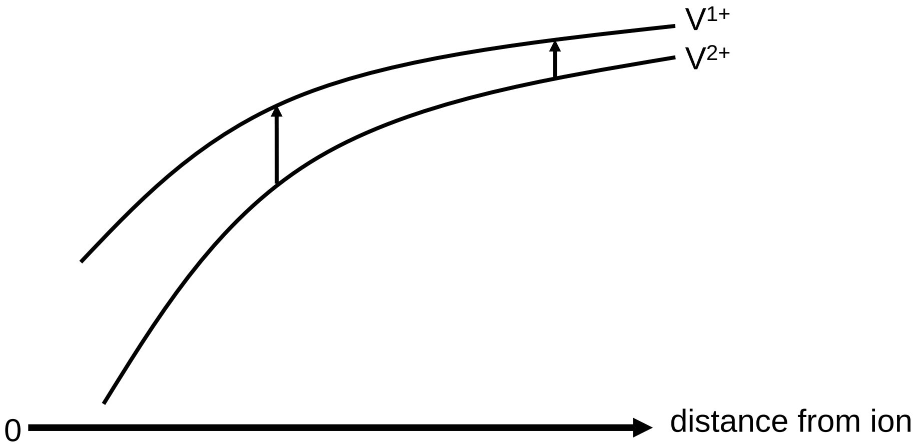

Figure 5.8: Illustration of post-collision interaction. V^{1+} is the potential curve of the singly charged ion and V^{2+} that of a doubly charged ion. At the time of overtaking, the Auger electron is shifted to the upper potential curve. The magnitude of the energy shift is larger for the process of overtaking occurring at smaller distances from the ion.

On the other hand, the combined influence of PCI and streaking is larger. This was confirmed by calculations from Sebastian Bauch and Prof. Dr. Michael Bonitz [105]. According to their model, the resulting spectra at the ascending slope with $\Delta\dot{W} > 0$ and at the descending slope with $\Delta\dot{W} < 0$ look different. In both cases the Auger electrons which are released only a short time after their related photoelectrons, experience a strong PCI effect and are thus shifted to higher energies. On the other hand, the later Auger electrons are only weakly influenced by the PCI effect. However, the phase of the THz field has changed for the later Auger electrons which is accompanied by a different streaking-induced energy shift. Thus, at the ascending slope, Auger electrons emitted at different times will always be shifted to higher energies. The amount of the energy shift is especially high for very early and very late Auger electrons. For intermediate release times there exists a minimum of the energy shift which is still positive. The situation is different at the descending slope, where the early Auger electrons are shifted to higher energies, while the later electrons are shifted to lower energies. In opposite to the previous case, there is no restriction on the sign of the energy shift. It was confirmed by Sebastian Bauch that this results in a larger Auger spectral width measured at the descending slope compared to the ascending slope [105]. Assuming an XUV pulse duration of 20 fs and a ponderomotive potential of 0.1 eV, he performed calculations on molecular dynamics of two electrons in the potential of the ion. At the beginning, the Auger electron movement is determined by the potential of the doubly charged ion, while after the process of overtaking the potential of a singly charged ion is applied. Here, the initial distributions of electron momenta and the emission times of the Auger electrons are defined according to their physical probabilities. The results are angularly resolved electron energy distributions at different phases of the THz field. In addition, the case without an applied THz field is considered. In order to also account for the detector response, TOF simulations using the program SIMION [93] were carried out within this work. The final electron energy spectra were obtained from the calculated angularly resolved spectra by applying the TOF parameters used in the experiments. For a comparison with the experimental data, in each case the calculated spectrum was plotted nine times with different amplitudes and spectral positions to account for the different Auger lines according to Table 5.1. Here, the overall amplitude was adjusted, and the whole spectrum was shifted in energy to match with the experimental data. This is necessary, because the spectra were not exactly taken at the zero-crossing of the energy shift, but at a slightly different time delay. Moreover, a background was added to the calculated data for a better comparison with the measurements. A wedge-shaped background was chosen such that experimental and calculated data are in accordance at the lowest and highest energy part of each spectrum. It is not completely clear what is the origin of this background in the measured data. The comparison between experimental and calculated data in Fig. 5.7 shows a fairly well agreement, and the linewidth asymmetry is confirmed by the calculations. Deviations can be caused by a number of reasons including the uncertainty of the pulse duration and a possible influence of the Gouy phase shift. In addition, one has to take into account that even in the field-free case the spectrum cannot fully be reproduced by the Auger lines. Another point is that the calculations were carried out only for Auger line 4, and a comparable behavior was assumed for the other lines. One has to have in mind, however, that the kinetic energies of the electrons vary for the different lines which may slightly influence the PCI effect on the streaked Auger electrons. Moreover, the natural linewidths of the different Auger lines vary between 104 meV and 111 meV [110]. This means that the Auger decay has a slightly different time constant which may lead to small differences in the streaked widths for the other Auger lines.

number	interpretation	spectral position	relative intensity
20	$M_4N_1N_{2,3}:{}^3P_2$	42.14 eV	58
21	$M_4N_1N_{2,3}:{}^3P_1$	41.69 eV	10
23	$M_5N_1N_{2,3}:{}^3P_2$	40.89 eV	46
24	$M_5N_1N_{2,3}:{}^3P_1$	40.46 eV	62
25	$M_5N_1N_{2,3}:{}^3P_0$	40.19 eV	21
27	$M_4N_1N_{2,3}:{}^1P_1$	38.71 eV	157
30	$M_5N_1N_{2,3}:{}^1P_1$	37.67 eV	211

Table 5.2: Spectral positions, relative intensities and interpretation of krypton Auger lines. The data and nomenclature of the lines are taken from [104].

For a further confirmation of the observed asymmetry, the Auger lines of krypton were studied. Here, one benefits from the flexibility that was accomplished due to the development of the laser-based terahertz-field-driven streak camera. It was thus possible on a short time scale to change the photon energy in order to exceed the ionization threshold of the $3d$ electrons in krypton. Therefore, different XUV mirrors with a central reflectivity at 97.5 eV were used to reflect the 63^{rd} harmonic order. Thus, the energy of the emitted $3d$ electrons is only around 3 eV, while the considered Auger electrons have an energy of about 40 eV. The process of overtaking will now take place at smaller distances from the ion which increases the influence of the PCI effect compared to the xenon case. Fig. 5.9 shows seven krypton Auger lines which are labeled in Table 5.2. The procedure of plotting the calculated and simulated data is analog to what was done for xenon. Only the ponderomotive potential was changed to 0.08 eV to resemble the experimental conditions in this case. Now, the broadening at the descending slope is increased and well reproduced by the calculations. While the calculated difference in linewidths between the ascending and descending slope is 120 meV for xenon, it is 320 meV for krypton. This meets the expectations of an increased PCI influence in the latter case and is a clear evidence for the correctness of the presented model.

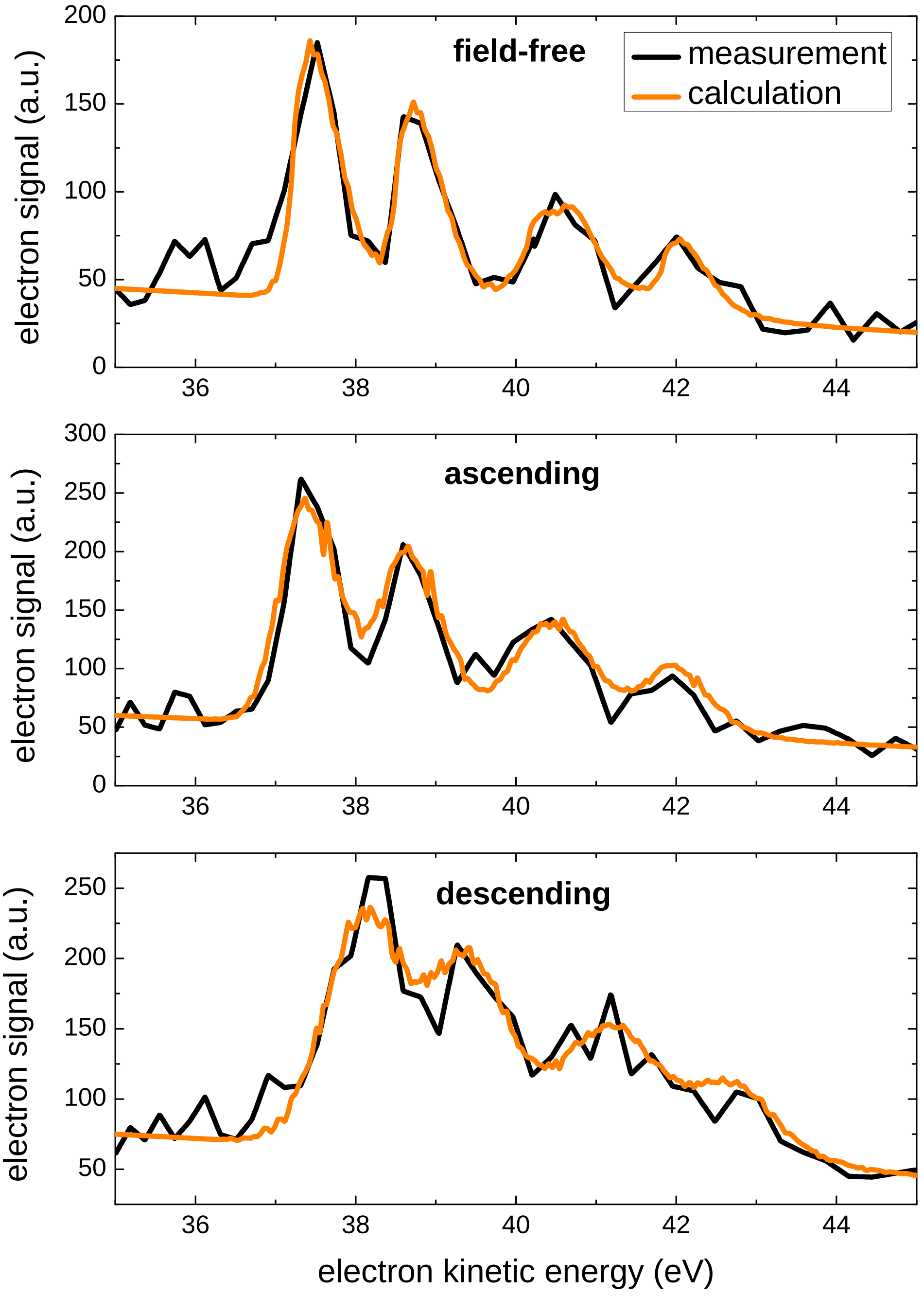

Figure 5.9: Same as Fig. 5.7, but for krypton Auger spectra. The difference in linewidths at the different slopes is increased. The calculations were carried out by Sebastian Bauch [105].

Since the broadening of the spectra depends on the Auger decay time, one can in principle measure the different broadenings and from that infer the characteristic decay time. So far, Auger decay times in the femtosecond range could directly be measured with laser-generated sidebands [23]. Thus, the results obtained here are a first example of electron wavepacket sampling making use of the THz-field-driven streak camera. Light-field streaking is widely used in attosecond metrology and becomes now available in the fs range as well. Note that the above results could not have been obtained by NIR streaking, because the Auger decay time of about 6 fs is longer than the NIR oscillation period. This means that the relevant information would be smeared out by using NIR pulses. Another interesting aspect is that the observed effect is distinct, albeit the XUV pulse duration is about three times larger than the Auger decay time. It is thus feasible to get access to dynamics on a time scale well below the XUV pulse duration.

When performing pulse duration measurements with Auger lines, one has to be sure that the linewidths are not influenced by the PCI effect. This can be guaranteed in a constellation where the photoelectron is faster than the Auger electron. In this case, no overtaking takes place and correspondingly no energy is transferred. An important condition here is that the Auger decay time must be short compared to the XUV pulse duration as well as the THz oscillation period to minimize effects from Auger electrons which are released at different times with respect to the time of photoionization.

5.4 Application at free electron lasers

When applying the laser-based terahertz-field-driven streak camera for the pulse characterization at a free electron laser, several issues are of importance and will be discussed in the following.

Since FELs experience an arrival time jitter, the synchronization to an external laser is a demanding task. It has been shown, however, that at the Linac Coherent Light Source (LCSL) the synchronization of the FEL pulses to an optical laser is feasible with a timing uncertainty on the scale of the X-ray pulse duration [10]. Thus, a small arrival time jitter compared to the THz oscillation period is expected. As a consequence, the FEL pulses arriving at different times will be coincident with slightly different slopes of the THz vector potential. The value of the slope can be extracted for each pulse after evaluating the measured kinetic energy shift. In this way, an accurate determination of the pulse duration can be performed for each shot. Also FELs seeded by a HHG source can be temporally characterized by the laser-based THz-field-driven streak camera. When generating HHG and THz radiation with the same laser pulse, one benefits from an inherent synchronization between these pulses.

In addition to the arrival time jitter, FELs are characterized by fluctuating intensities, pulse durations and pulse shapes. Therefore, it is important to measure the pulse duration and possibly the pulse shape for each single shot. The streak camera developed in this work has a single-shot capability for a sufficient photon flux. Using neon as photoemitter and having a pulse energy of the 59^{th} harmonic of about 0.2 pJ in the interaction zone, one electron was detected at about each third shot. This means that for a pulse energy of 1 nJ more than 1000 electrons could be detected. This number is regarded as sufficient for a single-shot spectrum. When, however, also the field-free spectrum of the FEL fluctuates, this has to be measured simultaneously for each shot. In this case, the spectrum can be recorded by a TOF which is located in a perpendicular direction to the THz polarization. As a consequence, the neon $2p$ line is not suitable anymore, because the electrons are mainly emitted into the direction of the XUV polarization. Alternatively, the krypton $4p$ line can be employed [16], where electrons are emitted in the directions parallel and perpendicular to the XUV polarization. This behavior and the fact that krypton has a lower cross section for radiation at 90 eV reduces the number of detected electrons. Therefore, a higher pulse energy of up to 1 μJ might be required for the single-shot mode. Typically, this is still a small fraction of the pulse energy delivered by FELs. It is thus possible to measure the pulse duration for each single shot and use the remaining part of the radiation for a time-resolved experiment.

Yet another important parameter is the temporal resolution of the streak camera which was already discussed for the harmonic radiation. However, at

X-ray FELs such as LCLS, much higher photon energies are generated and the spectral width of the pulses is typically increased to a few eV. On the one hand, this means that higher streaking amplitudes and streaking speeds are obtained, since these depend on the initial electron kinetic energy (cf. Eq. 2.63). On the other hand, also a larger streaking-induced broadening is required which should at least be equal to the spectral width of the field-free photoelectron spectrum. Thus, comparable time resolutions of a few fs can be achieved depending on the specific experimental parameters. When, on the other hand, Auger electrons are used for streaking, the demands on the streaking speeds are lower due to the much narrower spectrum in the field-free case. This can possibly improve the achievable time resolution, but is ultimately limited by the Auger decay time.

First measurements were performed at LCLS with the streaking technique at a wavelength of $2.4\,\mu$m [111]. It is therefore only possible to measure very short pulses with durations of up to a few fs. In contrary, with the laser-based THz-field-driven streak camera one can cover pulse durations from a few fs to a few hundreds of fs, thereby bridging the whole gap between attosecond and conventional streak cameras.

Chapter 6

Conclusion and outlook

In the present work, a novel laser-based terahertz-field-driven streak camera was developed which makes it possible for the first time to implement this technique in the laboratory for the characterization of fs XUV pulses. As a fundamental component of the streak camera, a single-cycle terahertz source relying on optical rectification in a lithium niobate crystal was designed. The characterization of this source revealed a quantum generation efficiency from NIR photons to THz photons of 117 %, thus exceeding the highest value of 100 % reported so far for this kind of source [21]. In addition, the electric field strength of more than 20 MV/m is higher than for systems with comparable pump pulse energies [52]. The latter is an important parameter for the light-field-driven streak camera, where XUV pulses create photoelectrons which are accelerated by the superimposed THz field. As an XUV radiation source, an NIR pulse is focused into a neon gas target to generate high-order harmonic radiation. Since the same NIR pulse is recycled to produce the THz radiation, both XUV and THz pulses are inherently synchronized. In a first step, the transient THz electric field was measured via the streaking method. It is thus an alternative technique to electro-optic sampling with the advantageous feature that it does not suffer from saturation effects in a crystal as well as crystal imperfections. Therefore, the streak camera is expected to give a more accurate determination of the THz electric field strength.

Electrons created at different times within the XUV pulse duration are accelerated by the THz field by different amounts which results in a broadening of the measured photoelectron spectra compared to the field-free case. By measuring photoelectron spectra with and without THz field, the duration of the HHG pulses could be reconstructed. For a fundamental pulse with a duration of 25 fs, the streaking measurement revealed a temporal width of (22^{+4}_{-6}) fs of the 59^{th} harmonic order. In addition, the chirp was determined with the help of two electron detectors located in opposite directions. This gave an estimated linear chirp rate of (-2 ± 2) meV/fs. It was shown that the harmonic chirp could be controlled by applying a chirp to the fundamental laser pulse. The temporal resolution of the laser-based terahertz-field-driven streak camera is 10 fs and thus comparable to the streak camera developed at the Free Electron Laser in Hamburg (FLASH) [16], while being much more compact, flexible and cost efficient. The presented technique thus bridges the gap in time resolution between attosecond and conventional streak cameras.

Finally, the capability of this approach for electron wavepacket sampling in the femtosecond range was demonstrated. After creating photoelectrons and Auger electrons, the correlation between these was studied. It turned out that the combined effects of THz streaking and post-collision interaction had a distinct impact on the measured Auger spectra. The THz-field-driven streak camera therefore opens up the way for measuring electron dynamics in the femtosecond range.

The ability of measuring XUV pulse durations can still be improved by enhancing the output energy of the THz source. This is planned for the future and will be realized by cooling the THz generation crystal down to the temperature of liquid nitrogen. In this way, absorption of higher THz frequencies within the crystal is diminished. As a consequence, not only the overall THz output energy is increased, but the higher frequencies also allow for a smaller THz focus size and thus a higher intensity. In addition, the oscillation period of the THz field becomes smaller. All these effects result in a higher streaking speed and thus a better temporal resolution.

Since the THz source is mobile, the technique can be implemented at XUV sources beyond the laboratory scale in the future. It is exceedingly suited for the pulse characterization of FELs seeded by a HHG source. In this case, the THz and HHG pulses can be generated by the same laser which ensures an inherent synchronization between them. Furthermore, the laser-based THz-field-driven streak camera can be utilized for the XUV pulse duration measurement at other FELs. As an example, results at LCLS have shown that the synchronization to an external laser source is feasible. This allows for an implementation of the laser-based THz-field-driven streak camera which also works at X-ray photon energies. Depending on the laser source used for THz generation as well as the streaked electron kinetic energies, a temporal resolution of several fs is possible.

By utilizing the streak camera for electron wavepacket sampling, it is possible to measure atomic and molecular decay times which are in the fs range. The idea is that a system is pumped by an XUV pulse to excite a certain state. When this state decays under the emission of electrons, the reconstructed temporal structure represents a convolution of the XUV pulse width and the exponential decay. The method can be implemented for excited states having decay times longer than the XUV pulse duration. This is true for the decay of certain Auger processes, including interatomic Auger decays in argon dimers [112]. Even though the cross sections are low, these processes can be studied by averaging over a large number of HHG pulses, since the shot-to-shot fluctuations are low.

Appendix A

Gaussian beams

The propagation of a laser beam is in many cases well described by a Gaussian beam. This means that the intensity of the beam in transverse direction has a Gaussian profile which is given by

$$I(r,z) = \frac{P}{\pi w^2(z)/2} \exp\left(-2\frac{r^2}{w^2(z)}\right). \tag{A.1}$$

Here, r and z are the coordinates in transverse and longitudinal directions, respectively, P is the power of the laser beam and $w(z)$ is the beam radius for which the intensity has dropped to $1/e^2$ of the maximum value. The propagation equation of a Gaussian beam is obtained by solving the paraxial form of the Helmholtz equation. For a monochromatic beam, the complex electric field amplitude is given by [113]

$$E(r,z) = E_0 \frac{w_0}{w(z)} \exp\left(-\frac{r^2}{w^2(z)}\right) \exp\left(-ikz - \frac{ikr^2}{2R(z)} + i \arctan\frac{z}{z_R}\right), \tag{A.2}$$

with the peak amplitude E_0, the beam diameter at the beam waist w_0, the wavenumber $k = 2\pi/\lambda$, the radius of the wavefronts $R(z)$ and the Rayleigh length z_R for which $w(\pm z_R) = \sqrt{2}w_0$ (cf. Fig. A.1). The latter is expressed as

$$z_R = \frac{\pi w_0^2}{\lambda}. \tag{A.3}$$

The distance $b = 2z_R$ is also called confocal parameter. The beam radius along the propagation axis can then be calculated as

$$w(z) = w_0\sqrt{1 + \left(\frac{z}{z_R}\right)^2}. \tag{A.4}$$

For large values of z, the parameter $w(z)$ approaches a line which allows the definition of a beam divergence:

$$\Theta = \frac{\lambda}{\pi w_0}. \tag{A.5}$$

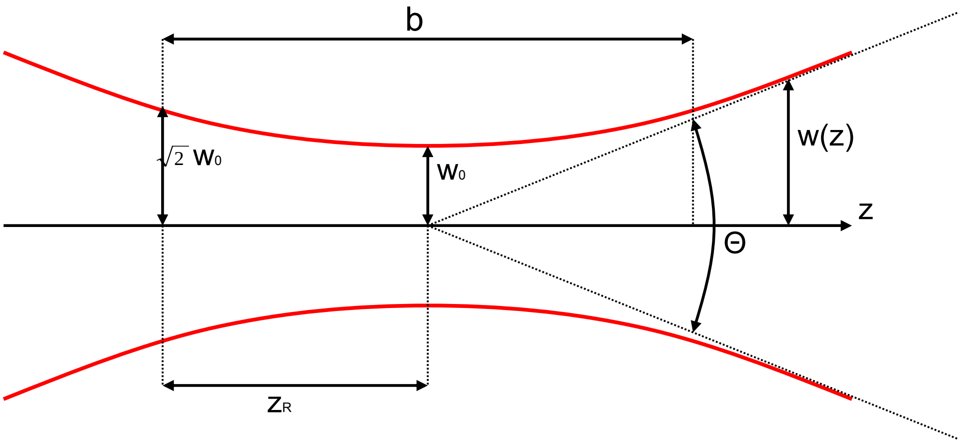

Figure A.1: Schematic of a Gaussian beam which propagates in z direction

The last term of the phase in Eq. A.2 is referred to as the Gouy phase shift:

$$\phi(z) = \arctan\left(\frac{z}{z_R}\right). \tag{A.6}$$

In the boundaries from $-\infty$ to $+\infty$, a Gaussian beam exhibits a phase shift of π, while in the limits of the confocal parameter the Gouy phase shift is $\pi/2$.

Appendix B

Derivation of the pulse front tilt after diffraction off a grating

The derivation of Eq. 2.33 follows the treatment in [56]. Here, a monochromatic beam with wavelength λ and diameter D is assumed. The beam illuminates a distance W on the diffraction grating which has a groove spacing of d (see also Fig. 2.5). Before the incoming beam is diffracted off the grating, both the intensity pulse front and the phase front, are perpendicular to the propagation direction of the beam. The diffraction equation for the first order reads

$$d(\sin\alpha + \sin\beta) = \lambda. \tag{B.1}$$

Here, α is the incident angle of the beam on the grating, and β refers to the angle at which the beam is diffracted. The angular dispersion ($d\beta/d\lambda$) can now be obtained by a differentiation of Eq. B.1 with respect to λ:

$$\frac{d\beta}{d\lambda} = \frac{1}{d\cos\beta}. \tag{B.2}$$

It can be seen from Fig. 2.5 that the upper edge of the beam travels a longer distance than the lower side which is because of two reasons. First, the orientation of the grating with respect to the incoming beam leads to an additional distance a. Secondly, diffraction off the grating makes the upper side propagate a further distance b with respect to the lower side. a and b can be rewritten as

$$a = W \cdot \sin\alpha = D\frac{\sin\alpha}{\cos\alpha}, \tag{B.3}$$

$$b = W \cdot \sin\beta = D\frac{\sin\beta}{\cos\alpha}. \tag{B.4}$$

As a consequence, the upper side of the beam is delayed by a distance $a + b$ with respect to the lower side which leads to the resulting tilt of the pulse front. It can be deduced by further geometrical considerations. The beam width P after diffraction is

$$P = W \cdot \cos\beta = D\frac{\cos\beta}{\cos\alpha}. \tag{B.5}$$

For the tilt angle γ follows

$$\begin{aligned}
\tan\gamma &= \frac{a+b}{P} \\
&= \frac{\sin\alpha + \sin\beta}{\cos\beta} \\
&= \frac{\lambda}{d\cos\beta} \\
&= \lambda\frac{d\beta}{d\lambda}.
\end{aligned} \tag{B.6}$$

The last equation relates the tilt angle of the beam to the angular dispersion. It is valid for one wavelength, but for an ultrashort pulse containing many wavelengths one can sum up over the various monochromatic components.

Appendix C

Transmission of teflon in the THz range

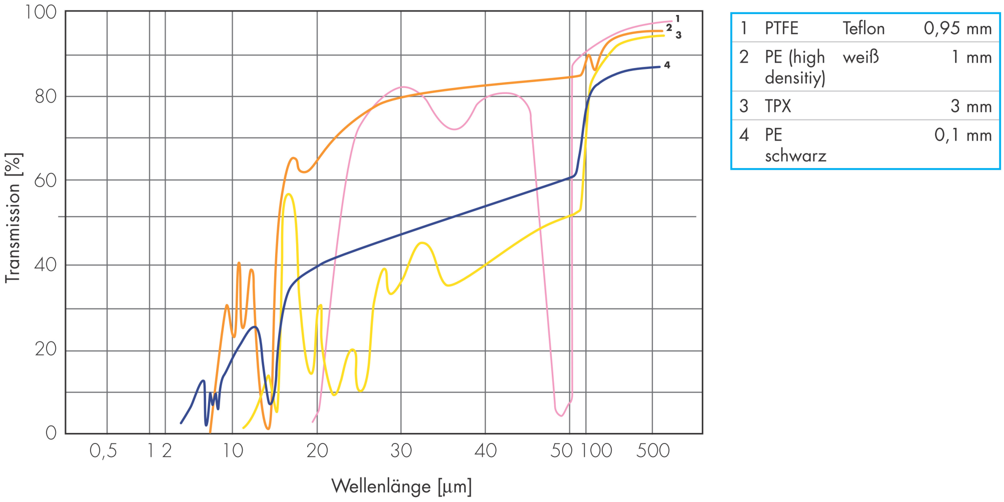

Figure C.1: Transmission curve of teflon in the THz range (taken from [114]).

Abbreviations

Abbreviation	Explanation
CCD	Charge-Coupled Device
CPA	Chirped-Pulse Amplification
EOS	Electro-Optic Sampling
FEL	Free Electron Laser
FFT	Fast Fourier Transform
FLASH	Free Electron Laser in Hamburg
fs	femtosecond
FWHM	Full Width at Half Maximum
HHG	High-order Harmonic Generation
LCLS	Linac Coherent Light Source
MCP	Microchannel Plate
NIR	Near-Infrared
PCI	Post-Collision Interaction
THz	Terahertz
TOF	Time-Of-Flight
XUV	Extreme Ultra-Violet

Acknowledgement

Here I want to thank all the people who supported me during the time I worked on this thesis.

First of all I would like to thank Markus Drescher for providing the exciting topic of my thesis and for supervising me as well as for the discussion of many problems.

Thanks also to Klaus Sengstock for reading and evaluating my work and to Günter Huber who was my co-supervisor and is going to evaluate my disputation.

Ulrike Frühling assisted me in many issues of the setup, the measurements and the analysis of the streaking experiment. She also helped me with correcting this script.

Marek Wieland was always eager to answer the many different questions I had, he helped me with many technical and experimental issues, and also corrected this thesis.

Armin Azima almost always knew about the right alignment technique of any component of the laser system and spent a lot of time to keep the system running.

Roland Kalms introduced me to the HHG setup and would always help me with issues of the laser system, the harmonic radiation or technical questions.

Michael Bonitz and Sebastian Bauch from the University of Kiel supported my by performing theoretical investigations on the streaking of Auger electrons.

Oliver Becker helped me in technical issues and in the fabrication of parts for my setup.

The mechanical workshop under the guidance of Stephan Fleig and the electrical workshop under the guidance of Armin Spikofsky fabricated a large number of parts which was necessary for my experimental setup.

Wolfgang Gärtner helped me with the design of the newly developed glued vacuum chambers.

Manfred Spiwek drilled accurate holes in any mirror.

In addition, I want to thank all the colleagues in my group for the good teamwork.

I acknowledge the Graduiertenkolleg 1355 for providing my scholarship and the many opportunities that it has given to gain insight in many different areas of photonic sciences.

Finally, I want to thank my friends, my family and Gaspar for all the support they have given to me in the last years.

Bibliography

[1] T. H. Maiman. Stimulated optical radiation in ruby. *Nature*, 187:493–494, 1960.

[2] A. H. Zewail. Laser femtochemistry. *Science*, 18:1645–1653, 1988.

[3] N. F. Scherer, R. J. Carlson, A. Matro, M. Du, A. J. Ruggiero, V. Romero-Rochin, J. A. Cina, G. F. Fleming, and S. A. Rice. Fluorescence-detected wave packet interferometry: Time resolved molecular spectroscopy with sequences of femtosecond phase-locked pulses. *J. Chem. Phys.*, 95:1487–1511, 1991.

[4] P. Eckle, A. N. Pfeiffer, C. Cirelli, A. Staudte, R. Dörner, H. G. Muller, M. Büttiker, and U. Keller. Attosecond ionization and tunneling delay time measurements in helium. *Science*, 322:1525–1529, 2008.

[5] M. M. Murnane, H. C. Kapteyn, M. D. Rosen, and R. W. Falcone. Ultrafast X-ray pulses from laser-produced plasmas. *Science*, 251:531–536, 1991.

[6] D. H. Auston. Picosecond optoelectronic switching and gating in silicon. *Appl. Phys. Lett.*, 26:101–103, 1975.

[7] A. McPherson, G. Gibson, H. Jara, U. Johann, T. S. Luk, I. A. McIntyre, K. Boyer, and C. K. Rhodes. Studies of multiphoton production of vacuum-ultraviolet radiation in the rare gases. *J. Opt. Soc. Am. B*, 4:595–601, 1987.

[8] M. Hentschel, R. Kienberger, C. H. Spielmann, G. A. Reider, N Milosevic, T. Brabec, P. Corkum, U. Heinzmann, M. Drescher, and F. Krausz. Attosecond metrology. *Nature*, 414:509–513, 2001.

[9] W. Ackermann *et al.* Operation of a free-electron laser from the extreme ultraviolet to the water window. *Nature Photon.*, 1:336–342, 2007.

[10] P. Emma *et al.* First lasing and operation of an angstrom-wavelength free-electron laser. *Nature Photon.*, 4:641–647, 2010.

[11] T. Sekikawa, T. Kanai, and S. Watanabe. Frequency-resolved optical gating of femtosecond pulses in the extreme ultraviolet. *Phys. Rev. Lett.*, 91:103902, 2003.

[12] Y. Nabekawa, H. Hasegawa, E. J. Takahashi, and K. Midorikawa. Production of doubly charged helium ions by two-photon absorption of an intense sub-10-fs soft X-ray pulse at 42 eV photon energy. *Phys. Rev. Lett.*, 94:043001, 2005.

[13] Y. Mairesse, O. Gobert, P. Breger, H. Merdji, P. Meynadier, P. Monchicourt, M. Perdrix, P. Salières, and B. Carre. High harmonic XUV spectral phase interferometry for direct electric-field reconstruction. *Phys. Rev. Lett.*, 94:173903, 2005.

[14] E. Goulielmakis, M. Uiberacker, R. Kienberger, A. Baltuska, V. Yakovlev, A. Scrinzi, Th. Westerwalbesloh, U. Kleineberg, U. Heinzmann, M. Drescher, and F. Krausz. Direct measurement of light waves. *Science*, 305:1267–1269, 2004.

[15] R. Kienberger, E. Goulielmakis, M. Uiberacker, A. Baltuska, V. Yakovlev, F. Bammer, A. Scrinzi, Th. Westerwalbesloh, U. Kleineberg, U. Heinzmann, M. Drescher, and F. Krausz. Atomic transient recorder. *Nature*, 427:817–821, 2004.

[16] Ulrike Frühling. *Lichtfeld getriebene Streak-Kamera zur Einzelschuss Zeitstrukturmessung der XUV-Pulse eines Freie-Elektronen Lasers.* PhD thesis, Universität Hamburg, Fachbereich Physik, 2009.

[17] M. Schultze, M. Fie, N. Karpowicz, J. Gagnon, M. Korbman, M. Hofstetter, S. Neppl, A. L. Cavalieri, Y. Komninos, T. H. Mercouris, C. A. Nicolaides, R. Pazourek, S. Nagele, J. Feist, J. Burgdörfer, A. M. Azzeer, R. Ernstorfer, R. Kienberger, U. Kleineberg, E. Goulielmakis, F. Krausz, and V. S. Yakovlev. Delay in photoemission. *Science*, 328:1658–1662, 2010.

[18] D. J. Cook and R. M. Hochstrasser. Intense terahertz pulses by four-wave rectification in air. *Opt. Lett.*, 25:1210–1212, 2000.

[19] J. Hebling, G. Almási, I. Z. Kozma, and J. Kuhl. Velocity matching by pulse front tilting for large-area THz-pulse generation. *Opt. Expr.*, 10:1161–1166, 2002.

[20] K.-L. Yeh, M. C. Hoffmann, J. Hebling, and K. A. Nelson. Generation of 10 μJ ultrashort terahertz pulses by optical rectification. *Appl. Phys. Lett.*, 90:171121, 2007.

[21] A. G. Stepanov, S. Henin, Y. Petit, L. Bonacina, J. Kasparian, and J.-P. Wolf. Mobile source of high-energy single-cycle terahertz pulses. *Appl. Phys. B*, 101:11–14, 2010.

[22] Y. Shen, T. Watanabe, D. A. Arena, C.-C. Kao, J. B. Murphy, T. Y. Tsang, X. J. Wang, and G. L. Carr. Nonlinear cross-phase modulation with intense single-cycle terahertz pulses. *Phys. Rev. Lett.*, 99:043901, 2007.

[23] M. Drescher, M. Hentschel, R. Kienberger, M. Uiberacker, V. Yakovlev, A. Scrinzi, Th. Westerwalbesloh, U. Kleineberg, U. Heinzmann, and F. Krausz. Time-resolved atomic inner-shell spectroscopy. *Nature*, 419:803–807, 2002.

[24] E. Seres, J. Seres, and C. Spielmann. X-ray absorption spectroscopy in the keV range with laser generated high harmonic generation. *Appl. Phys. Lett.*, 89:181919–3, 2006.

[25] I. J. Kim, C. M. Kim, H. C. Kim, G. H. Lee, Y. S. Lee, J. Y. Park, D. J. Cho, and C. H. Nam. Highly efficient high-harmonic generation in an orthogonally polarized two-color laser field. *Phys. Rev. Lett.*, 94:243901, 2005.

[26] I. J. Kim, G. H. Lee, S. B. Park, Y. S. Lee, T. K. Kim, C. H. Nam, T. Mocek, and K. Jakubczak. Generation of submicrojoule high harmonics using a long gas jet in a two-color laser field. *Appl. Phys. Lett.*, 92:021125, 2008.

[27] I. Christov, H. Kapteyn, and M. Murnane. Quasi-phase matching of high-harmonics and attosecond pulses in modulated waveguides. *Opt. Expr.*, 7:362–367, 2000.

[28] P. B. Corkum. Plasma perspective on strong-field multiphoton ionization. *Phys. Rev. Lett.*, 71:1994–1997, 1993.

[29] M. Lewenstein, P. Balcou, M. Y. Ivanov, A. L'Huillier, and P. B. Corkum. Theory of high-harmonic generation by low-frequency laser fields. *Phys. Rev. A*, 49:2117–2132, 1994.

[30] M. V. Ammosov, M. B. Delone, and V. P. Kraïnov. Tunnel ionization of complex atoms and of atomic ions in an alternating electromagnetic field. *Sov. Phys. JETP*, 64:1191–1194, 1986.

[31] C. Ruilliere. *Femtosecond Laser Pulses: principles and experiments.* Springer Science+Business Media, Inc., New York, 2nd edition, 2005.

[32] X. He, M. Miranda, J. Schwenke, O. Guilbaud, T. Ruchon, C. Heyl, E. Georgadiou, R. Rakowski, A. Persson, M. B. Gaarde, and

A. L'Huillier. Spatial and spectral properties of the high-order harmonic emission in argon for seeding applications. *Phys. Rev. A*, 79:063829, 2009.

[33] W. Becker, S. Long, and J. K. McIver. Modeling harmonic generation by a zero-range potential. *Phys. Rev. A*, 55:1540–1560, 1997.

[34] T. Brabec (Editor). *Strong field laser physics.* Springer Science + Business Media, LLC, New York, 2008.

[35] P. Balcou, P. Salières, A. L'Huillier, and M. Lewenstein. Generalized phase-matching conditions for high harmonics: The role of field-gradient forces. *J. Opt. Soc. Am. B*, 55:3204–3210, 1997.

[36] P. M. Paul, E. S. Toma, P. Breger, G. Mullot, F. Augé, Ph. Balcou, H. G. Muller, and P. Agostini. Observation of a train of attosecond pulses from high harmonic generation. *Science*, 292:1689–1692, 2001.

[37] A. L'Huillier and P. Balcou. Calculations of high-order harmonic-generation processes in xenon at 1064 nm. *Phys. Rev. A*, 46:2778–2792, 1992.

[38] P. Salières, A. L'Huillier, and M. Lewenstein. Coherence control of high-order harmonics. *Phys. Rev. Lett.*, 74:3776–3779, 1995.

[39] M. E. Faldon, M. H. R. Hutchinson, J. P. Marangos, J. E. Muffett, R. A. Smith, J. W. G. Tisch, and C. G. Wahlstrom. Studies of time-resolved harmonic generation in intense laser fields in xenon. *J. Opt. Soc. Am. B*, 9:2094–2099, 1992.

[40] C.-G. Wahlström, J. Larsson, A. Persson, T. Starczewski, S. Svanberg, P. Salières, Ph. Balcou, and A. L'Huillier. High-order harmonic generation in rare gases with an intense short-pulse laser. *Phys. Rev. A*, 48:4709–4720, 1993.

[41] J. M. Schins, P. Breger, and P. Agostini. Cross-correlation measurements of femtosecond extreme-ultraviolet high-order harmonics. *J. Opt. Soc. Am. B*, 13:197–200, 1996.

[42] J. Mauritsson, P. Johnsson, , R. López-Martens, K. Varjú, W. Kornelis, J. Biegert, U. Keller, M. B. Gaarde, K. J. Schafer, and A. L'Huillier. Measurement and control of the frequency chirp rate of high-order harmonic pulses. *Phys. Rev. A*, 70:021801(R), 2004.

[43] J. Mauritsson, R. López-Martens, A. L'Huillier, and K. J. Schafer. Ponderomotive shearing for spectral interferometry of extreme-ultraviolet pulses. *Opt. Lett.*, 28:2393–2395, 2003.

[44] G. Mourou, C. V. Stancampiano, and D. Blumenthal. Picosecond microwave pulse generation. *Appl. Phys. Lett.*, 38:470–472, 1981.

[45] D. You, R. R. Jones, P. H. Bucksbaum, and D. R. Dykaar. Generation of high-power sub-single-cycle 500-fs electromagnetic pulses. *Opt. Lett.*, 18:290–292, 1993.

[46] A. Dreyhaupt, S. Winnerl, T. Dekorsy, and M. Helm. High-intensity terahertz radiation from a microstructured large-area photoconductor. *Appl. Phys. Lett.*, 86:121114, 2005.

[47] T. Bartel, P. Gaal, K. Reimann, M. Woerner, and T. Elsaesser. Generation of single-cycle THz transients with high electric-field amplitudes. *Opt. Lett.*, 30:2805–2807, 2005.

[48] M. D. Thomson, M. Kress, T. Löffler, and H. G. Roskos. Broadband THz emission from gas plasmas induced by femtosecond optical pulses: From fundamentals to applications. *Laser&Photon. Rev.*, 1:349–368, 2007.

[49] F. Blanchard, L. Razzari, H.-C. Bandulet, G. Sharma, R. Morandotti, J.-C. Kieffer, T. Ozaki, M. Reid, H. F. Tiedje, H. K. Haugen, and F. A. Hegmann. Generation of 1.5 μJ single-cycle terahertz pulses by optical rectification from a large aperture ZnTe crystal. *Opt. Expr.*, 15:13212–13220, 2007.

[50] A. G. Stepanov, L. Bonacina, S. V. Chekalin, and J.-P. Wolf. Generation of 30 μJ single-cycle terahertz pulses at 100 Hz repetition rate by optical rectification. *Opt. Lett.*, 33:2497–2499, 2008.

[51] J. Hebling, A. G. Stepanov, G. Almási, B. Bartal, and J. Kuhl. Tunable THz pulse generation by optical rectification of ultrashort laser pulses with tilted pulse fronts. *Appl. Phys. B*, 78:593–599, 2004.

[52] K.-L. Yeh, J. Hebling, M. C. Hoffmann, and K. A. Nelson. Generation of high average power 1 kHz shaped THz pulses via optical rectification. *Opt. Commun.*, 281:3567–3570, 2008.

[53] M. Bass, P. A. Franken, J. F. Ward, and G. Weinreich. Optical rectification. *Phys. Rev. Lett.*, 9:446–448, 1962.

[54] R. W. Boyd. *Nonlinear Optics.* Acadamic Press, Inc., San Diego, 1992.

[55] J. Hebling, K.-L. Yeh, M. C. Hoffmann, B. Bartal, and K. A. Nelson. Generation of high-power terahertz pulses by tilted-pulse-front excitation and their application possibilities. *J. Opt. Soc. Am. B*, 25:B6–B19, 2008.

[56] Ka-Lo Yeh. *The generation of high field terahertz radiation and its application in terahertz nonlinear spectroscopy.* PhD thesis, Massachusetts Institute of Technology, Department of Chemistry, 2009.

[57] T. P. Dougherty, G. P. Wiederrecht, and K. A. Nelson. Impulsive stimulated Raman scattering experiments in the polariton regime. *J. Opt. Soc. Am. B*, 9:2179–2189, 1992.

[58] D. H. Auston and M. C. Nuss. Electrooptic generation and detection of femtosecond electrical transients. *IEEE J. Quantum Electron.*, 24:184–196, 1988.

[59] B. Bartal, I. Z. Kozma, A. G. Stepanov, G. Almási, J. Kuhl, E. Riedle, and J. Hebling. Toward generation of μJ range sub-ps THz pulses by optical rectification. *Appl. Phys. B*, 86:419–423, 2007.

[60] A. G. Stepanov, J. Kuhl, I. Z. Kozma, E. Riedle, G. Almási, and J. Hebling. Scaling up the energy of THz pulses created by optical rectification. *Opt. Expr.*, 13:5762–5768, 2005.

[61] D. Redfield and W. J. Burke. Optical absorption edge of $LiNbO_3$. *J. Appl. Phys.*, 45:4566–4571, 1974.

[62] M. C. Hoffmann, K.-L. Yeh, J. Hebling, and K. A. Nelson. Efficient terahertz generation by optical rectification at 1035 nm. *Opt. Expr.*, 15:11706–11713, 2007.

[63] L. Pálfalvi, J. Hebling, G. Almási, Á. Péter, K. Polgár, K. Lengyel, and R. Szipöcs. Nonlinear refraction and absorption of Mg doped stoichiometric and congruent $LiNbO_3$. *J. Appl. Phys.*, 95:902–908, 2004.

[64] L. Pálfalvi, J. Hebling, J. Kuhl, Á. Péter, and K. Polgár. Temperature dependence of the absorption and refraction of Mg-doped congruent and stoichiometric $LiNbO_3$ in the THz range. *J. Appl. Phys.*, 97:123505, 2005.

[65] D. H. Auston, K. P. Cheung, J. A. Valdmanis, and D. A. Kleinman. Cherenkov radiation from femtosecond optical pulses in electro-optic media. *Phys. Rev. Lett.*, 53:1555–1558, 1984.

[66] D. A. Kleinman and D. H. Auston. Theory of electrooptic shock radiaton in nonlinear optical media. *IEEE J. Quantum Electron.*, 20:964–970, 1984.

[67] D. Mittleman (Editor). *Sensing with Terahertz radiation.* Springer, Berlin, Heildelberg, New York, 2003.

[68] Y.-S. Lee. *Principles of Terahertz Science and Technology.* Springer, New York, 2009.

[69] Bernd Richard Steffen. *Electro-optic methods for longitudinal bunch diagnostics at FLASH.* PhD thesis, Universität Hamburg, Fachbereich Physik, 2007.

[70] J. D. Jackson. *Classical Electrodynamics.* John Wiley and Sons, Inc., 3rd edition, 1999.

[71] S. Casalbuoni, H. Schlarb, B. Schmidt, B. Steffen, P. Schmüser, and A. Winter. Numerical studies on the electro-optic sampling of relativistic electron bunches. *TESLA-Bericht*, 2005-01, 2005.

[72] A. Yariv and P. Yeh. *Optical waves in crystals: propagation and control of laser radiation.* John Wiley and Sons, Inc., 3rd edition, 1983.

[73] P. C. M. Planken, H.-K. Nienhuys, H. J. Bakker, and T. Wenckebach. Measurement and calculation of the orientation dependence of terahertz pulse detection in ZnTe. *J. Opt. Soc. Am. B*, 18:313–317, 2001.

[74] Q. Wu and X.-C. Zhang. Ultrafast electro-optic field sensors. *Appl. Phys. Lett.*, 68:1604–1606, 1996.

[75] D. J. Bradley, B. Liddy, and W. E. Sleat. Direct linear measurement of ultrashort light pulses with a picosecond streak camera. *Opt. Commun.*, 2:391–395, 1971.

[76] M. Y. Schelev, M. C. Richardson, and A. J. Alcock. Image-converter streak camera with picosecond resolution. *Appl. Phys. Lett.*, 18:354–357, 1971.

[77] M. Uiberacker, E. Goulielmakis, R. Kienberger, A. Baltuska, T. Westerwalbesloh, U. Keineberg, U. Heinzmann, M. Drescher, and F. Krausz. Attosecond metrology with controlled light waveforms. *Laser Phys.*, 15:195–204, 2005.

[78] M. M. Shakya and Z. H. Chang. Achieving 280 fs resolution with a streak camera by reducing the deflection dispersion. *Appl. Phys. Lett.*, 87:041103, 2005.

[79] J. Feng, H. J. Shin, J. R. Nasiatka, W. Wan, A. T. Young, G. Huang, A. Comin, J. Byrd, and H. A. Padmore. An X-ray streak camera with high spatio-temporal resolution. *Appl. Phys. Lett.*, 91:134102, 2007.

[80] U. Frühling, M. Wieland, M. Gensch, T. Gebert, B. Schütte, M. Krikunova, R. Kalms, F. Budzyn, O. Grimm, J. Rossbach, E. Plönjes, and M. Drescher. Single-shot terahertz-field-driven X-ray streak camera. *Nature Photon.*, 3:523–528, 2009.

[81] J. Itatani, F. Quéré, G. L. Yudin, M. Y. Ivanov, F. Krausz, and P. B. Corkum. Attosecond streak camera. *Phys. Rev. Lett.*, 88:173903, 2002.

[82] F. Quéré, Y. Mairesse, and J. Itatani. Temporal characterization of attosecond XUV fields. *J. Mod. Opt.*, 52:339–360, 2005.

[83] Eleftherios Goulielmakis. *Complete Characterization of Light Waves using Attosecond Pulses.* PhD thesis, Ludwigs-Maximilian-Universität München, Fachbereich Physik, 2005.

[84] D. E. Spence, P. N. Kean, and W. Sibbett. 60-fsec pulse generation from a self-mode-locked ti:sapphire laser. *Opt. Lett.*, 16:42–44, 1991.

[85] G. Strickland, D. und Mourou. Compression of amplified chirped optical pulses. *Opt. Commun.*, 56:219–221, 1985.

[86] Patrick Rüdiger. *Setup, characterization and optimization of a high harmonic conversion cell for the generation of coherent EUV radiation.* Diploma thesis, Universität Bielefeld, 2008.

[87] Lasse Schroedter. *Design, Simulation and Operation of two Spectrometers for the Analysis of High Harmonic and Fluorescence Radiation in the Extreme Ultraviolet Spectral Range.* Diploma thesis, Universität Hamburg, 2009.

[88] Roland Kalms. *Eine lasergestützte Apparatur für Experimente zum magnetischen Lineardichroismus in der Photoemission.* PhD thesis, Universität Hamburg, Fachbereich Physik, 2010.

[89] T. A. Johnson, R. Soufli, E. M. Gulikson, and M. Clift. Zirconium and niobium transmission data at wavelengths from 11-16 nm and 200-1200 nm. *Proc. SPIE*, 5538:119–124, 2004.

[90] Center for X-ray optics, X-ray interactions with matter calculator by E. Gullikson, URL: *http://henke.lbl.gov/optical_constants/*.

[91] L. Pálfalvi, J. A. Fülöp, G. Almási, and J. Hebling. Novel setups for extremely high power single-cycle terahertz pulse generation by optical rectification. *Appl. Phys. Lett.*, 92:171107, 2008.

[92] Christopher Behrens. *Detection and spectral measurements of coherent synchrotron radiation at FLASH.* Diploma thesis, Deutsches Elektronen-Synchrotron (DESY), Hamburg, 2008.

[93] SIMION 3D, version 7.00. 1999.

[94] M. Nagai, M. Jewariya, Y. Ichikawa, H. Ohtake, T. Sugiura, Y. Uehara, and K. Tanaka. Broadband and high power terahertz pulse generation beyond excitation bandwidth limitation via $\chi^{(2)}$ cascaded processes in $LiNbO_3$. *Opt. Expr.*, 17:11543–11549, 2009.

[95] A. G. Stepanov, J. Hebling, and J. Kuhl. Efficient generation of subpicosecond terahertz radiation by phase-matched optical rectification using ultrashort laser pulses with tilted pulse fronts. *Appl. Phys. Lett.*, 83:3000–3002, 2003.

[96] A. B. Ruffin, J. V. Rudd, J. F. Whitaker, S. Feng, and H. G. Winful. Direct observation of the Gouy phase shift with single-cycle terahertz pulses. *Phys. Rev. Lett.*, 83:3410–3413, 1999.

[97] U. Becker and D. A. Shirley (Editors). *VUV and Soft X-Ray Photoionization.* Plenum press, New York and London, 1996.

[98] J. A. Bearden and A. F. Burr (Editors). *Photoemission in Solids I: General Principles.* Springer-Verlag, Berlin, 1978.

[99] B. Schütte, U. Frühling, M. Wieland, A. Azima, and M. Drescher. Electron wave packet sampling with laser-generated extreme ultraviolet and terahertz fields. *Opt. Express*, (submitted), 2011.

[100] Y. Mairesse and F. Quéré. Frequency-resolved optical gating for complete reconstruction of attosecond bursts. *Phys. Rev. A*, 71:011401, 2005.

[101] G. Sansone, E. Benedetti, F. Calegari, C. Vozzi, L. Avaldi, R. Flammini, L. Poletto, P. Villoresi, C. Altucci, R. Velotta, S. Stagira, S. De Silvestri, and M. Nisoli. Isolated single-cycle attosecond pulses. *Science*, 314:443–446, 2006.

[102] U. Frühling *et al.*,. *Unpublished results*, 2008.

[103] B. Schütte, S. Bauch, U. Frühling, M. Bonitz, and M. Drescher *et al.* *Publication in preparation*, 2011.

[104] L. O. Werme, T. Bergmark, and K. Siegbahn. The high resolution $L_{2,3}$MM and $M_{4,5}$NN auger spectra from krypton and $M_{4,5}$NN and $N_{4,5}$OO auger spectra from xenon. *Physica Scripta*, 6:141–150, 1972.

[105] Sebstian Bauch and Michael Bonitz. *Private communication*, 2011.

[106] O. Smirnova, M. Spanner, and M. Y. Ivanov. Coulomb and polarization effects in laser-assisted xuv ionization. *J. Phys. B*, 39:323–339, 2006.

[107] R. B. Barker and H. W. Berry. Electron energy distributions from ionizing collisions of helium and neon ions with helium*. *Phys. Rev.*, 151:14–19, 1966.

[108] A. Niehaus. Analysis of post-collision interactions in auger processes following near-threshold inner-shell photoionization. *J. Phys. B: At. Mol. Phys.*, 10:1845–1857, 1977.

[109] V. Schmidt, N. Sandner, W. Mehlhorn, M. Y. Adam, and F. Wuilleumier. Post-collision interaction in the xenon $N_{4,5}$-OO auger spectrum excited by photon impact. *Phys. Rev. Lett.*, 38:63–66, 1977.

[110] M. Jurvansuu, A. Kivimäki, and S. Aksela. Inherent lifetime widths of Ar $2p^{-1}$, Kr $3d^{-1}$, Xe $3d^{-1}$, and Xe $4d^{-1}$ states. *Phys. Rev. A*, 64:012502, 2001.

[111] R. Kienberger. Attosecond spectroscopy on solid surfaces. *DPG-Tagung*, SYAP 1.4, 2011.

[112] Y. Morishita, X.-J. Liu, N. Saito, T. Lischke, M. Kato, G. Prümper, M. Oura, H. Yamaoka, Y. Tamenori, I. H. Suzuki, and K. Ueda. Experimental evidence of interatomic coulombic decay from the Auger final states in argon dimers. *Phys. Rev. Lett.*, 96:243402, 2006.

[113] B. E. A. Saleh and M. C. Teich. *Fundamentals of Photonics.* John Wiley and Sons, Inc., 1st edition, 1991.

[114] Eigenschaften optischer Materialien, LOT Ultra, URL: *http://www.lot-oriel.com/at/de/home/eigenschaften-optischer-materialien/.*

List of Figures

List of Tables

Selbständigkeitserklärung

Diese Arbeit ist von mir selbstständig verfasst worden, und ich habe keine anderen als die angegebenen Quellen und Hilfsmittel verwendet.

Bernd Schütte, Juli 2011